X-Ray Thomson Scattering as Dynamic Temperature and Microstructure Diagnostic

Oliver Karnbach

Christ Church

University of Oxford

A thesis submitted for the degree of

Doctor of Philosophy

Trinity, 2022

So much of life ahead.

—Carpenters

Abstract

Whilst the field of High Energy Density physics spans a history of more than a century, it lacks a reliable dynamic temperature diagnostic. This work presents computational and experimental work on developing such technique based on the principle of detailed balance.

In molecular dynamics simulations, monocrystalline copper is shocked along [001] to pressures ranging between ambient and 70 GPa, and its synthetic elastic and inelastic diffraction signal is computed via the spatial and temporal Fourier transforms of the atomic coordinates. In the plastic regime beyond the Hugoniot elastic limit, the crystals slip faults and stacking faults arise, which cause certain Bragg spots to link up in reciprocal space. The compression facilitates the detection of the inelastic phonon modes through pressure hardening by increasing their spacing in energy space, yet the quasi-elastic signal linked to the stacking faults can dominate the spectra outside of the first Brillouin zone. Whilst these temperature measurements highly benefit from increased resolution, it is proposed that the shock compression setups can also determine a Doppler-induced energy shift on the order of meV, which could be used as a direct particle velocity diagnostic.

As part of a collaboration in the European XFEL experiment p2191, the ambient and resistively elevated temperatures of monocrystalline diamond are determined. In order to expand this technique into the field of dynamic compression, more results of experiment p2191 and work of p2656 presented here recorded spectra for polycrystalline copper, cobalt, and nickel samples. Whilst no temperature could be determined, the photon levels for a seeded XFEL sufficed to generate high-resolution spectra of inelastic scattering that exhibit varying asymmetry, indicating the presence of microstructure-related quasi-elastic scattering. Whilst predictions about the inelastic signal strength through a photometrics code could be verified, diffraction data remained inconclusive due to poor grain statistics in the polycrystalline targets.

Acknowledgments

I would very much like to thank my supervisors Justin Wark and Gianluca Gregori for the fantastic opportunity to work with them in the Clarendon laboratory and their guidance throughout my time in Oxford. Similarly, I have enjoyed excellent support by my post-docs David McGonegle, Charlotte Palmer, Shenyuan Ren, and am particularly grateful for having witnessed Patrick Heighway's excellence in anything MD related and Oliver Humphries' deep knowledge of EuXFEL detectors.

Further, I would like to thank my collaborators at various research facilities, such as Lennart Wollenweber of EuXFEL, Adrien Descamps of SLAC, Andy Comley of AWE, and Rob Rudd of LLNL. My gratitude also goes to Sam Vinko and Muhammad Kasim for helpful discussions, and Paul Pattinson for trusting me with using his laboratories. Furthermore, I gratefully acknowledge support from AWE via the Oxford Centre for High Energy Density Science (OxCHEDS), the Engineering and Physical Sciences Research Council (EPSRC), and the LLNL Institutional Computing Grand Challenge program.

Special thanks is due also to the friends that stuck around throughout the chapters of my life, including everyone from the department and college that made my years in (and out of) the Simon Room very enjoyable, particularly Robin, Mark, Jimmy, Joseph, Linnea, Tom, Hannah, Charlie, Pontus, Alessandro, Marko, Bernd, Del, and Dan.

Lastly, thank you to Josse for continuing to be interested in my life and excited about my day, even whilst I was writing this thesis, and my family for their love and support throughout my life, particularly for bearing with my excitement when reporting about the crazy things I have learnt first in school, then at university.

Table of Contents

List of Figures

List of Tables

Chapter 1

Introduction

1.1 Motivation and Historic Context

Research in the field of matter in extreme conditions has kept mankind occupied for many generations of scientists and has a rich, well-documented history[1–11]. In addition to purely academic reasons – the mere fascination of understanding these exotic states – or to design nuclear fusion reactors[12, 13], describing the interior of our own planet and characterising the objects within our solar system (and beyond) is of growing importance[14–19]. On much smaller spatial scales, ultra-high pressure research involves the prediction and generation of novel metastable materials, with the prominent example of diamond being a recovered variation of carbon that would not form under ambient conditions[20–24].

Due to their highly energetic nature, such extreme states of matter usually either exist only for a brief time or need elaborate containment, which is why handling them comes with unique challenges. To characterise their nature on microscopic scales, x-ray diffraction is one of the earliest structure diagnostics employed to characterise high-pressure or high-temperature phase diagrams[25–29]. These techniques could be advanced in line with improved x-ray and neutron beams, such as from synchrotrons and spallation sources, which allowed to disperse scattered beams in energy to obtain high-resolution inelastic spectra[30–36]. Particularly, intricacies like the collective motion of the constituent atoms under high pressure could be analysed through the creation or annihilation of phonons[37–48]. Since these modes–on the order of meV–are of very low energy, the relative bandwidth of interacting x-rays–on the order of keV–is required to be extremely narrow.

As of today, there a several well-established methods of obtaining matter at such extreme pressures. A prominent static route is through diamond anvil cells (DACs), where a small sample is wedged between two brilliant-cut diamonds and pressures beyond 600 GPa can be

obtained[49, 50, 43, 44, 51–55]. Apart from static compression, dynamic methods involving inertial confinement often allow for even higher pressure states to be reached, for example via rapid compression through explosives or gas guns[56–59]. More recently, the compression through high-intensity lasers of nanosecond pulse duration has been combined with intense x-ray beams of similar or shorter duration[60–90]. Such rapid loading usually results in the compression wave gradually steepening into a shock when traversing the sample, where the behaviour of the latter is described by the Rankine-Hugoniot equations[91, 92]. Shocking significantly increases the entropy of the compressed material and, despite the higher confinement due to increased pressure, causes most elements to melt around 100-300 GPa[93–95]. This can be circumvented through 'quasi-isentropic' (QI) compression, where the initial strong shock (e.g., one top-hat laser pulse) either is replaced by several weaker laser shocks or reverberates within specifically designed targets[96]. In the continuous limit, this can be achieved through a gradually increasing ramp profile[97–100, 80, 101–105], where the materials at several TPa were found to remain solid[106–111].

The field of high energy density (HED) physics highly benefits from the immense progress in transient x-ray sources of increasing brightness, where early developments involved laser generated plasmas[60, 61, 112, 64, 68, 69, 71, 76, 80, 113] that were complemented by synchrotrons[114–116, 83, 86, 117]. The current state-of-the-art, 4th generation light sources, are X-ray Free Electron Lasers (XFELs)[118–121], pushing the peak spectral brightnesses by more than nine orders of magnitude beyond those of synchrotrons. This gave rise to a multitude of publications[70, 72–75, 77, 78, 84, 122, 82, 87, 88], where these intense x-ray sources are used to probe dynamically compressed matter through diffraction in order to extract information of their microstructure with unprecedented temporal resolution on the order of fs. Such work is supported by a wide range of simulations[123–131], which evolved alongside increasing computing power, and help the analysis and design of experimental campaigns.

Given the highly transient nature of shock and QI compression, probes determining the

thermodynamic properties of the compressed matter need to be equally confined in time, where the sample density commonly is determined through Bragg or Laue diffraction from the previously described sources. Furthermore, the pressure often is indirectly inferred from the breakout velocity through Velocity Interferometer System for Any Reflector (VISAR) measurements[132–134], where an equation of state is linked to the Rankine-Hugoniot relations. Whilst these methods for density and pressure have a proven track record, as of today, a precise dynamic temperature diagnostic is lacking. Due to complex microstructural behaviour, where plastic compression and relaxation changes the heat within the solid, it also cannot be reliably inferred like pressure is. A common route attempts to compare the intensity of Bragg spots or the modulation of an x-ray absorption edge in Extended X-ray Absorption Fine Structure (EXAFS), which both are linked to the Debye-Waller effect[135–141]. However, this method directly relies on the Debye temperature of the sample, which depends on the pressure and sample microstructure, and also itself is a function of temperature again.

A proposed route to fully characterise the thermodynamic state of the compressed solid is through its phonons. Hereby, an x-ray inelastically scatters off these thermalised lattice vibrations by creating or annihilating phonons, corresponding to Stokes or anti-Stokes interaction. The relative intensity of these processes depends on the absolute temperature through the principle of detailed balance[142, 30, 31, 143], and could be used as a direct diagnostic in dynamic compression experiments[144, 145]. Given the low energy of these modes compared to the x-rays employed to resolve the atomic lattice spacing, a highly monochromatised beam of extremely narrow bandwidth is required, which comes at the price of photon flux. Furthermore, the phonon cross section is about three orders of magnitude lower than the elastic signal at a Bragg spot[32, 31], and usually the extreme pressure state is only existent for a few ps. These are the main reasons for why only now, with the advent of extremely brilliant XFELs, dynamic experiments based on this principle are being developed, such as

at the Linac Coherent Light Source (LCLS)[144]. Particularly, related to the LCLS work but on unshocked monocrystalline diamond, the ambient and resistively heated temperature were obtained at the European XFEL (EuXFEL)[145, 146] with an uncertainty of about 9%. Whilst this static experiment overcame the low photon numbers through integrating over many XFEL pulses, recent developments such as seeding[147, 148] substantially increased the potential photon flux. Further research on improving these sources for shock and QI compression experiments is in progress, in order to combine the dynamic temperature diagnostic with intense, ultrashort, high-repetition-rate drivers, such as the DiPOLE laser[149] at the EuXFEL.

This work reports on progress being made towards using inelastic x-ray scattering as temperature and microstructure diagnostic in shock and QI compression. Molecular dynamics (MD) simulations of shocked, monocrystalline copper provide insight into the interplay of elastic and inelastic signal contributions and their effect on potential temperature measurements. Further, two experimental campaigns covering proof-of-principle experiments at ambient conditions inform the design of future dynamic endeavours, outlining anticipated signal strengths and resolution requirements.

1.2 Structure of Thesis and Author Contributions

Due to the collaborative nature of experimental work in HED science (and most research in general), parts of the results in this thesis were found through team efforts. This section aims at outlining the content of the following chapters whilst highlighting the author contributions.

Chapter 2 provides an overview of relevant theoretical concepts employed throughout this thesis that is based on well-known material covered in various textbooks. First, the structure and dynamics of crystals is introduced, followed by the description of their behaviour under shock compression. Second, the physics of x-ray generation through XFELs, and their interaction with solid matter through Compton and Thomson scattering is presented. Lastly, the

computational concepts used to simulate shocked crystals and to extract inelastic Thomson scattering from noisy x-ray detectors are outlined.

Work presented in Chapter 3 is about MD simulations of shocked copper crystals, with pressures ranging up to 70 GPa, where synthetic inelastic scattering is compared to elastic scattering. The simulations set up by the author, David McGonegle, and Patrick Heighway were run with `LAMMPS`, which was developed by the Sandia National Laboratories. For the parallelised spatial Fourier transforms, part of a code suite called 'Son of Howard' was used, which was developed by past Wark group members. Part of the real-space analysis was done with the commercially available program `Ovito` and the phase diagram demarcation data in Figure 3.3 was extracted from Sadigh[150].

Chapter 4 features signal strength predictions of p2191 and p2656 based on an inelastic photometrics code, qualitative simulations, and experimental diffraction data. p2191 was the commissioning experiment of the EuXFEL HED instrument, where a large number of collaborators were involved, consisting of researchers from the EuXFEL, Deutsches Elektronen-Synchrotron (DESY), Stanford Linear Accelerator Center (SLAC), Lawrence Livermore National Laboratory (LLNL), Atomic Weapons Establishment (AWE), and the Universities of Jena, Rostock, Trento, Warwick, and Oxford. Given the timeline of the beam time competition, the proposal had been submitted prior to the author joining the University of Oxford. The p2656 campaign was designed by the EuXFEL, the Indian Institute of Science, and University of Oxford, and executed by the EuXFEL, the Helmholtz Zentrum Dresden Rossendorf, and the University of Oxford. Particularly, the development of the four-bounce (533) monochromator was led by Lennart Wollenweber. The experimental work in the HED chamber involved a large number of EuXFEL scientists, where the author provided design specifications, provided and mounted the Oxford targets, and informed the target selection process with photon numbers. The p2656 Laue diffraction setup was designed and implemented by Thomas Preston and the author. The initial EuXFEL data analysis (reading

data, correcting x-ray camera signals) were done by Oliver Humphries, Lennart Wollenweber, Adrien Descamps, and the author. The Single Photon Counting routine was proposed by Oliver Humphries and Adrien Descamps, and implemented by Oliver Humphries and the author. The course of action during the experiments and the subsequent interpretation of the p2191 experimental results were aided by discussions with the respective collaborators, particularly Adrien Descamps, Emma McBride, Benjamin Ofori-Okai, Siegfried Glenzer, Lennart Wollenweber, Thomas Preston, Ulf Zastrau, David McGonegle, Oliver Humphries, Julian Lütgert, and Justin Wark. The shape function scattering code in Section 4.4.1 was developed by Oliver Humphries, Ed Rowe, and the author. The mimicked polycrystal was generated with the simulations described in Chapter 3, yet the parallelised Fourier spatial averaging routine was developed by Pontus Svensson, Thomas Gawne, and the author.

Chapter 5 is about the experimental equivalent under ambient conditions at the HED instrument of the EuXFEL of the simulations presented in Chapter 3, where high-resolution inelastic spectra were obtained. These were analysed by the author with the program `maleo`, which was designed by Muhammad Kasim.

The main findings of this work are summarised and put into context in Chapter 6, where also future trends in the field of inelastic scattering in shocked solids are evaluated. Figure 6.1 was reproduced from Descamps[145].

The bulk of the work in Chapter 3 is included in the manuscript Karnbach 2021[151], which was published in the Journal of Applied Physics. Part of the collaborative work in Chapters 4 and 5 resulted in the publications by Preston[152], Descamps[145], and Wollenweber[146], with the author of this thesis a co-author.

Chapter 2

Selected Concepts of Shocked Solids, X-Ray Scattering, and Scientific Computation

2.1 Introduction

This chapter provides an overview of selected background information and nomenclature used in this thesis. Hereby, concepts of solid matter at extreme conditions and the physics of x-rays, together with relevant computational methods will be featured. Given each of these topics has been explored by physicists for many decades now, for a greater depth of detail the reader is referred to the numerous publications on these matters[153–158].

2.2 Realistic Crystals and Shock Physics

2.2.1 Crystal Structures

Central to this work are crystals, that constitute a large fraction of condensed matter in the universe. In the most general sense, crystalline matter consists of atoms arranged in a periodic manner that, through this periodicity, exhibits unique collective features.

Matter consisting of N_α atoms and N_β electrons is described by a highly complex wave function accounting for the $N_\alpha + N_\beta$ positions and $N_\alpha + N_\beta$ velocities in 3D space, not even taking into account intrinsic properties like spin. Yet, due to its extreme symmetry, a perfect crystal can be described with much fewer parameters; that is as a sum of identical units–the crystal basis–that are arranged on a periodic lattice. The latter is given by all positions $\mathbf{R}$ through

$$\mathbf{R} = m_1\mathbf{a_1} + m_2\mathbf{a_2} + m_3\mathbf{a_3} \tag{2.1}$$

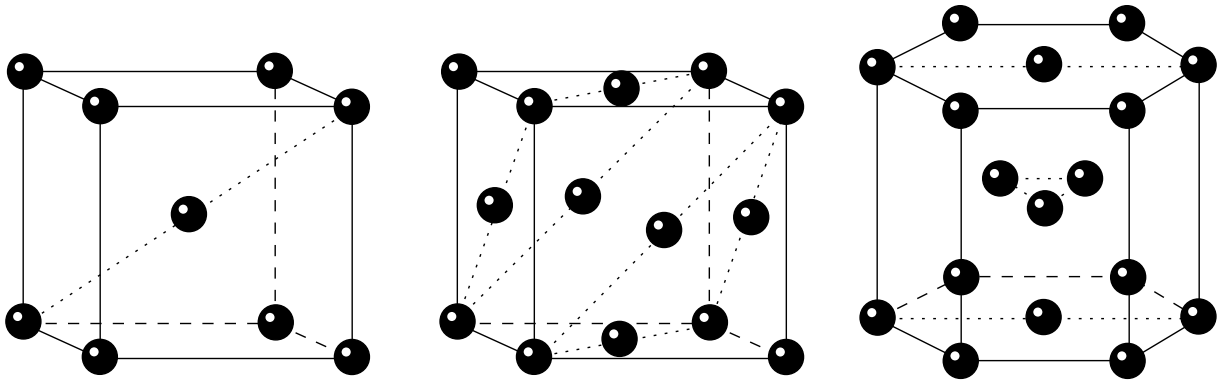

Figure 2.1: Schematic of conventional unit cells of bcc, fcc, and hcp. The sc structure is the same as bcc, yet without the central atom.

with m_1, m_2, and $m_3 \in \mathbb{Z}$. The vectors $\mathbf{a}_1$, $\mathbf{a}_2$, $\mathbf{a}_3$ are linearly independent (yet their choice is not unique) and are called primitive lattice vectors if the parallelepiped they are spanning–the primitive unit cell–contains only one lattice point. Its volume is V is given as

$$V = \mathbf{a_1} \cdot (\mathbf{a_2} \times \mathbf{a_3})$$

and, placed at each lattice point $\mathbf{R}$, fills the entire crystal space. For practical reasons, there are several different choices of unit cells (conventional unit cells) that contain more than one lattice point. Particularly relevant for this work are cubic crystals, where $\mathbf{a}_1$, $\mathbf{a}_2$, and $\mathbf{a}_3$ are orthogonal and of the same length, hence spanning a perfect cube.

The crystal basis, which is repeated at each $\mathbf{R}$, can consist of single atoms, multiple identical atoms, or many different atoms, ranging from pure Cu crystals to ion lattices of water ice, up to complex enzymes made of hundreds of atoms. Each atom itself exhibits a structure depending on its nucleus and the configuration-specific electron cloud (charge density) the respective element equilibrated at.

Lattices of the cubic family come in three main varieties as shown in Figure 2.1: simple cubic (sc), face-centred cubic (fcc), and body-centred cubic (bcc). In addition, the hexagonal close-packed (hcp) structure can be seen, which is part of the hexagonal crystal family.

Examples of such structures at ambient conditions are Be and Co in hcp, Cr and Fe in bcc, or Cu and Ni in fcc.

The position of each basis atom i within the crystal is found by

$$\mathbf{R}_i = m_1\mathbf{a}_1 + m_2\mathbf{a}_2 + m_3\mathbf{a}_3 + \mathbf{r}_i$$

with its position $\mathbf{r}_i$ within the conventional unit cell. Hence, in a cubic system with a lattice constant a (and a monoatomic *primitive* cell), the atoms are found at the following positions:

$$\begin{aligned}
\text{sc}: &\quad \mathbf{r}_1 = a\,(0,0,0) \\
\text{bcc}: &\quad \mathbf{r}_1 = a\,(0,0,0)\,, \quad \mathbf{r}_2 = \frac{a}{2}\,(1,1,1) \\
\text{fcc}: &\quad \mathbf{r}_1 = a\,(0,0,0)\,, \quad \mathbf{r}_2 = \frac{a}{2}\,(0,1,1)\,, \quad \mathbf{r}_3 = \frac{a}{2}\,(1,0,1)\,, \quad \mathbf{r}_4 = \frac{a}{2}\,(1,1,0)\,.
\end{aligned}$$

Diamond, relevant in Chapter 4, forms a fcc lattice with a two-atomic basis, and is referred to as face-centred diamond cubic (fcdc). The relative displacement of its two basis atoms is $\frac{1}{4}\,(\mathbf{a}_1 + \mathbf{a}_2 + \mathbf{a}_3)$ and the atoms of the diamond structure are located at the following positions:

$$\begin{aligned}
\text{fcdc}: &\quad \mathbf{r}_1 = a\,(0,0,0)\,, \quad \mathbf{r}_2 = \frac{a}{2}\,(0,1,1)\,, \quad \mathbf{r}_3 = \frac{a}{2}\,(1,0,1)\,, \quad \mathbf{r}_4 = \frac{a}{2}\,(1,1,0)\,, \\
&\quad \mathbf{r}_5 = \frac{a}{4}\,(1,1,1)\,, \quad \mathbf{r}_6 = \frac{a}{4}\,(1,3,3)\,, \quad \mathbf{r}_7 = \frac{a}{4}\,(3,1,3)\,, \quad \mathbf{r}_8 = \frac{a}{4}\,(3,3,1)\,.
\end{aligned}$$

It is clear that these crystalline structures exhibit numerous symmetries in various directions and planes cutting through them. For that reason, it is convenient to use the Miller indices h, k, and l that describe equally-spaced crystal planes of equivalent direction. Hereby, the plane second-closest to the origin of the conventional unit cell intercepts the cell axes spanned by $\mathbf{a}_1$, $\mathbf{a}_2$, $\mathbf{a}_3$ at $\mathbf{a}_1/h$, $\mathbf{a}_2/k$, $\mathbf{a}_3/l$ respectively. For a cubic lattice, the spacing

between the (hkl) planes is

$$d_{hkl} = \frac{a}{\sqrt{h^2 + k^2 + l^2}}.$$

Conventionally, negative Miller indices are denoted with a horizontal bar, e.g., the planes with $h = 1$, $k = -2$, $l = 3$ are written as $(1\bar{2}3)$. Furthermore, due the cubic symmetry, the planes (100), (010), and (001) have equivalent spacing, they can be grouped through $\{100\}$ (referred to as a family of planes), which will be particularly relevant for polycrystalline samples presented later within this work.

2.2.2 Reciprocal Lattice

Directions of high symmetry within the crystal can be defined with help of these planes. For any given (hkl), the vector perpendicular to them is called reciprocal lattice vector $\mathbf{G}_{hkl}$. The reciprocal lattice is the real space lattice expressed in the basis of lattice planes, which is used in x-ray scattering off such crystals as shown later in this chapter. It is constructed from the Miller indices through the reciprocal lattice vectors $\mathbf{b}_1$, $\mathbf{b}_2$, and $\mathbf{b}_3$ by

$$\mathbf{G}_{hkl} = h\mathbf{b}_1 + k\mathbf{b}_2 + l\mathbf{b}_3$$

and its magnitude is inversely proportional to d_{hkl}. The reciprocal lattice vectors, that span the reciprocal space in analogy to Equation 2.1, can be calculated from

$$\begin{aligned}
\mathbf{b}_1 &= 2\pi \frac{\mathbf{a}_2 \times \mathbf{a}_3}{V} \\
\mathbf{b}_2 &= 2\pi \frac{\mathbf{a}_3 \times \mathbf{a}_1}{V} \\
\mathbf{b}_3 &= 2\pi \frac{\mathbf{a}_1 \times \mathbf{a}_2}{V},
\end{aligned}$$

with the volume V of the conventional unit cell and the constant 2π chosen such that the symmetry found in diffraction studies becomes apparent. Hence, they satisfy the property $\mathbf{a}_i \cdot \mathbf{b}_i = 2\pi\delta_{ij}$. From the reciprocal lattice vector, the lattice spacing can be found through

$$d_{hkl} = \frac{2\pi}{|\mathbf{G}_{hkl}|}.$$

In analogy to the crystal planes, directions within the crystal are denoted as $[hkl]$ and families of directions as $\langle hkl \rangle$.

2.2.3 Phonons

The above expressions describe a perfect crystal where the atoms are spatially localised around each lattice site, equivalent to a theoretical system at 0 K. At finite temperatures, the atoms oscillate around these equilibrium points. Due to the coupling between the atoms in a crystal, these thermal oscillations in the form of elastic waves can be described through quantised quasi-particles called phonons, that behave like bosonic particles.

Phonons are attributed a magnitude, energy or frequency, direction, and momentum. The latter two are commonly summarised as vector $\mathbf{q}$, referred to as the phonon wavevector. As bosons, the population of the mode with $\mathbf{q}$ is described by

$$\langle n_{\mathbf{q}j} \rangle = \left[\exp\left(\frac{\hbar\omega_{\mathbf{q}_j}}{k_B T} \right) - 1 \right]^{-1},$$

the Bose-Einstein distribution, where $\hbar\omega_{\mathbf{q}j}$ is the phonon energy with its angular frequency $\omega_{\mathbf{q}j}$, $\hbar$ the reduced Planck constant, T the temperature of the crystal and k_B the Boltzmann constant. In this work, only monatomic crystals are considered and the index j describes the acoustic transverse or acoustic longitudinal branch. For this simple case, the dispersion relation of a one-dimensional crystal (an infinite chain of atoms separated by a) is found by considering the n^{th} atom and the classical interaction with its direct neighbours according

to Newton and Hooke:

$$m\frac{\partial^2 x_n}{\partial t^2} = K\left[(x_{n+1} - x_n) + (x_{n-1} - x_n)\right], \tag{2.2}$$

with the effective spring constant K of their interatomic potential, x_n the position, and m the mass of the n^{th} atom. With the educated guess

$$x_n = A\exp\left[i\left(qx - \omega t\right)\right]$$

and $A \neq 0$, Equation 2.2 can be solved for the phonon dispersion relation

$$\omega\left(q\right) = 2\sqrt{\frac{K}{m}}\left|\sin\frac{qa}{2}\right|$$

which is plotted in Figure 2.2. It describes the relation between the phonon energy $\hbar\omega$ and its momentum q. Its maximum is at $q_{max} = \frac{\pi}{a}$ with a frequency (the Debye frequency) of $\omega_D = 2\sqrt{\frac{K}{m}}$, where its group velocity is zero whilst each atom is of directly opposite phase as its neighbours, and it vanishes at $q_{min} = m\frac{2\pi}{a}$ for $m \in \mathbb{Z}$. The latter implies that phonons only exist between the reciprocal lattice vectors $\mathbf{G}$, where their energy is the highest exactly in between two reciprocal lattice points. Note that for this monatomic 1D system, only one solution per momentum is found (the acoustical modes), whilst for crystal systems with polyatomic bases, additional polarisations and optical phonon branches arise.

The dispersion relation found for the monatomic case can be expanded into 3D for more complicated crystals. Customarily, the functional dependence is displayed in a basis of crystal directions of high symmetry. All other directions can be inferred via superposition of several phonons. Note that there is no single correct choice of basis, but this choice of symmetry reduces algebraic complexity.

In addition to describing which phonon modes exist, in the context of x-ray scattering it

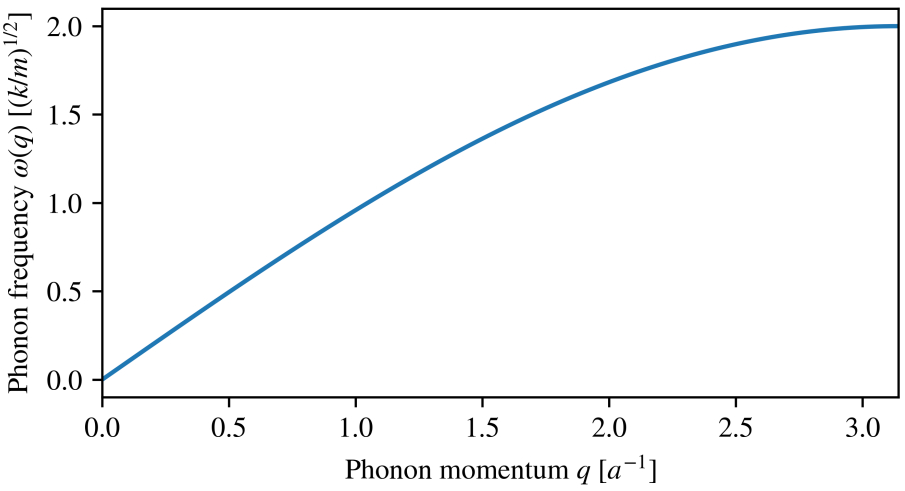

Figure 2.2: Longitudinal phonon dispersion relation for a monatomic 1D chain of equally spaced identical atoms. For low momenta, the relation can be linearly approximated with the slope given as the speed of sound.

also is helpful to understand their density of states $g(\omega)\,\mathrm{d}\omega = \hat{g}(q)\,\mathrm{d}q$, i.e., how many phonon modes can exist at a certain energy $\omega + \mathrm{d}\omega$ or momentum interval $\mathbf{q} + \mathrm{d}\mathbf{q}$, which will affect the scattering cross section. Hereby, the Debye model provides a instructive approximation. For a cubic crystal of extent L and N atoms, the 3D mode density in q-space is $\left(\frac{L}{2\pi}\right)^3$ per polarisation. For one longitudinal and two transverse polarisations, the total number of modes is $3N$. The Debye model defines a highest wave vector q_D or frequency ω_D as a cut-off, that defines a sphere such that the correct number of modes is contained:

$$3N = \int_0^{q_D} \hat{g}(q) 4\pi q^2 \mathrm{d}q = \int_0^{q_D} 3\left(\frac{L}{2\pi}\right)^3 4\pi q^2 \mathrm{d}q \tag{2.3}$$

$$= \frac{V}{2\pi^2} q_D^3 \tag{2.4}$$

with the real-space volume $V = L^3$. Further, the Debye model assumes a linear dispersion relation of $\omega \approx v_s q$ with the speed of sound v_s. Thus the Debye frequency $\omega_D = v_s q_D$ is

found with Equation 2.4 as

$$\omega_D = v_s \left(\frac{6\pi^2 N}{V} \right)^{\frac{1}{3}}.$$

To find the density of states in energy space, Equation 2.3 is compared with the energy density and converted with the derivative of the approximated dispersion relation $\frac{\mathrm{d}q}{\mathrm{d}\omega} = \frac{1}{v_s}$ as

$$g(\omega)\mathrm{d}\omega = \hat{g}(q)\mathrm{d}q = 3\frac{V}{(2\pi)^3} 4\pi \left(\frac{\omega}{v_s} \right)^2 \frac{\mathrm{d}\omega}{v_s}$$
$$g(\omega) = \frac{9N}{\omega_D^2}\omega^2.$$

The key takeaway of this expression for a 3D crystal is the quadratic growth of the density of states with the phonon frequency. Whilst the Debye model only is an approximate description of the physics of phonons, experimental findings in monatomic crystals show that indeed the density of states rising with ω is a good rule-of-thumb. Note that the presented considerations are good approximations for phonons in crystals whose potential is quasi-harmonic (usually a good approximation for low temperatures), but projecting the thermal crystal modes to harmonics (cf. temporal Fourier transforms) has its limits at higher temperature, where anharmonic effects such as phonon-phonon scattering will start to play a role.

2.2.4 Stress and Strain

In addition to phonon modes in ambient crystals, this work will investigate their behaviour under compression through a force applied to one of their surfaces. This is referred to as stress, and for the simple case of a normal force of magnitude F applied to a crystal face A is defined as $\sigma = F/A$. This can be expanded into a 3D tensor $\underline{\underline{\sigma}}$ to account for shear stress

that arises perpendicular to the force applied in any of the three cardinal directions:

$$\underline{\underline{\sigma}} = \begin{pmatrix} \sigma_{xx} & \sigma_{yx} & \sigma_{zx} \\ \sigma_{xy} & \sigma_{yy} & \sigma_{zy} \\ \sigma_{xz} & \sigma_{yz} & \sigma_{zz} \end{pmatrix}$$

with the stress σ_{ij} being the i-component of the stress applied on a unit area normal in the j-coordinate. The mean pressure of the system is given by a third of the trace of this tensor.

Applying stress will change the crystal and cause a reaction (a resistance to being compressed), where it can change its volume, shape, and orientation. Hereby, true strain is defined as $\mathrm{d}\epsilon = \frac{\mathrm{d}l}{l}$ and describes the infinitesimal length change $\mathrm{d}l$ along the normal of a material of initial length l. The strain rate is the time derivative of ϵ, and affects which deformation mechanisms are active.

For a normal compression in simple 1D uniaxial stress geometry, the strain is proportional to the stress through Young's modulus E as $\epsilon = \sigma/E$ and the crystal behaves elastically (reversible length changes upon varied stress). For most crystals, this linear approximation only holds true for small enough stresses as beyond a certain threshold (the yield stress), the response of the crystal will encompass plastic changes (irreversible). Analogously to stress, strain in realistic systems also is a tensor quantity and related to stress through a stiffness tensor. In the plastic regime, there is coupling between the σ_{ii} components and upon full material yield (no internal strength), the system becomes hydrodynamic in character, where $\sigma_{xx} = \sigma_{yy} = \sigma_{zz}$ like it is the case in fluids.

2.2.5 Crystallographic Defects

So far, the crystal systems introduced in this chapter have been for perfect lattices with small, thermal oscillations around their equilibrium position. Usually, materials are defective, where their structure exhibits deviations from that order. It is useful to treat imperfect crystals as

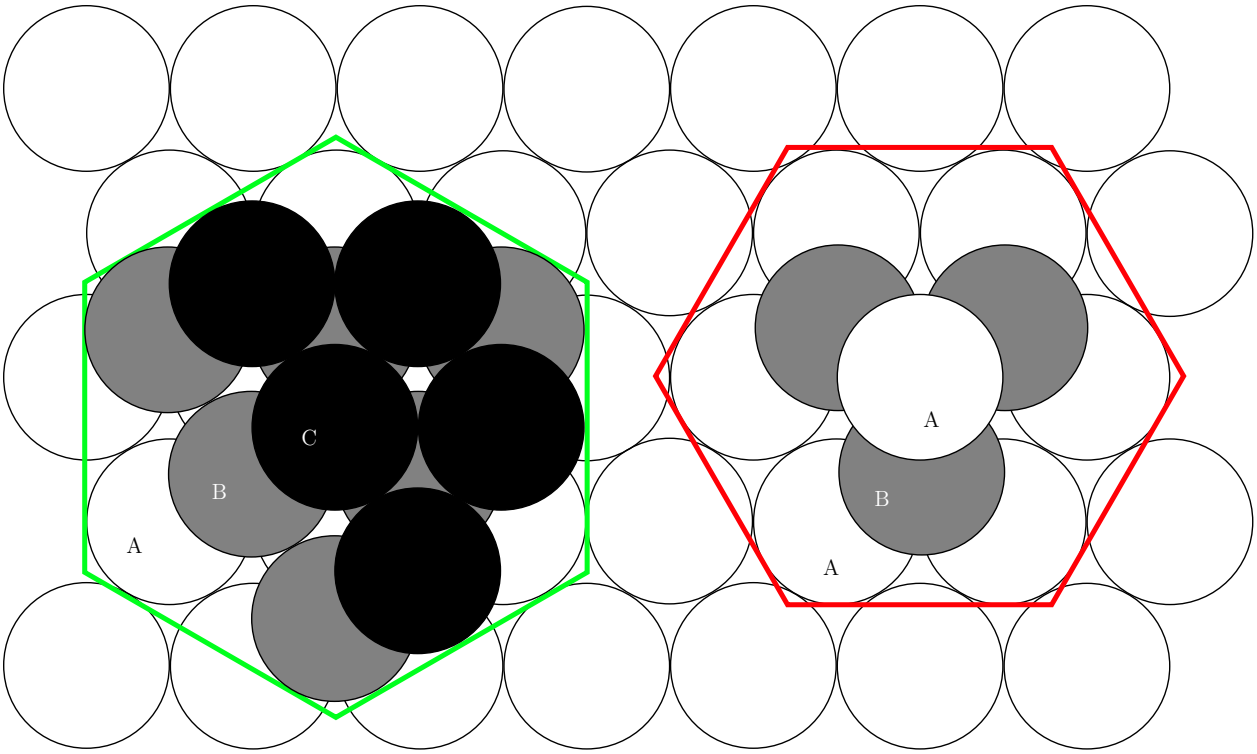

Figure 2.3: Schematic of the stacking sequence of close-packed structures. On the left, fcc can be seen, which consists of three different layers A, B, and C when viewed at in (111) (paper plane), described by an ABCABC... sequence. On the right, hcp can be seen, which consists of only two alternating layers A and B.

a superposition of a perfect crystal and certain defects, that in turn have certain effects on the physical properties of the material, e.g., their yield strength. Given the large number of atoms present in even microscopic samples, there is a wide variety of defects which come in different dimensionality.

The lowest ones are point defects, such as vacancies (an atom is simply missing within the lattice), interstitial atoms (an arbitrary type of atom placed between the lattice sites), or substitute atoms. One-dimensional deviations are line defects such as dislocations (primarily full or partial edge and screw dislocations). One dimension higher, there are planar defects such as stacking faults or grain boundaries, whilst lastly, holes/pores, cracks, or small regions of different material are classified as volume defects.

This work focuses on grain boundaries and stacking faults. Grain boundaries are the

imperfect link between two adjacent crystallites (e.g., created through the merger of two growing crystals of mismatched orientations) and are numerous in polycrystals. Stacking faults, which through homogeneous nucleation are the main defect arising behind the shock front in the Cu simulations, are changes in stacking order. In Figure 2.3, the (111) plane of a fcc crystal is shown (layer A). Superimposed is the next layer (B), followed by a final layer (C) before A would be repeated again (ABCABC...). Similarly shown in Figure 2.3, the sequence ABAB... is shown as the order for a hcp crystal. For a perfect fcc crystal, slipping on plane relative to the rest can create a stacking fault. For example, the faulted order ABCABABC... will locally be a hcp contribution to the lattice. At the edge of such faults, partial dislocations can be found to reconcile the defects with the otherwise perfect lattice. The example for a stacking fault spanning the entire sample can be seen in the Appendix A, Figure A.1.

2.2.6 Shock Wave Physics

The experimental and simulation work in the field of HED physics frequently involves the usage of shock compression to obtain extreme states of matter. Macroscopically, shock waves are described as a discontinuity of pressure, density, and energy propagating faster than the speed of sound in the unshocked medium. Such a scenario is shown in Figure 2.4, where a medium of mass density ρ_0, pressure P_0, volume-specific internal energy E_0, and velocity U_0, that is initially at rest ($U_0 = 0$), is driven by a piston with velocity U_p (the particle velocity) generating a shock front at velocity U_s and altering the state variables between the piston and that discontinuity.

The behaviour of strong shocks, where the stress exceeds the yield strength of the material and the system is dominated by fluid-like behaviour, is well described by the set of Rankine-Hugoniot equations[91, 92]. These can be found by considering the conservation of mass, momentum, and energy at the discontinuity defined by the shock front.

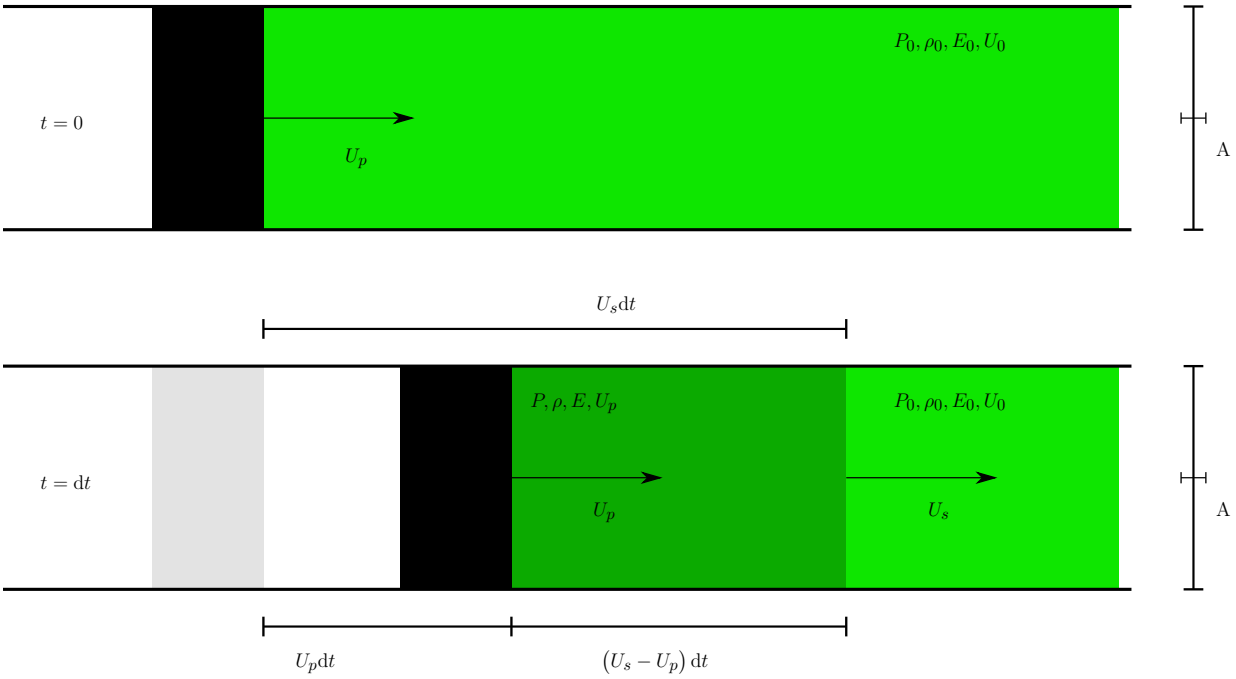

Figure 2.4: Schematic of the shock compression model process used to derive the Rankine-Hugoniot equations. A piston (black) drives into a medium of density ρ_0 (light green) from the left, compressing it to ρ (dark green).

Starting from the conservation of mass, at time $t = \mathrm{d}t > 0$ the total mass in the compressed region is found through its density and volume as $m = \rho V = \rho A \left(U_s - U_p\right) \mathrm{d}t$. Similarly, at $t = 0$, the corresponding uncompressed region corresponds to $m = \rho_0 A U_s \mathrm{d}t$. Eliminating A and $\mathrm{d}t$ results in the 1st Rankine-Hugoniot equation:

$$\rho_0 U_s = \rho \left(U_s - U_p\right).$$

Further, according to Newton's 2nd law, the change of momentum p of that mass m equals the force F applied over $\mathrm{d}t$, where

$$\mathrm{d}p = \left(\rho_0 U_s A \mathrm{d}t\right) U_p$$

$$F \mathrm{d}t = \left(P - P_0\right) A \mathrm{d}t$$

which yields the 2nd Rankine-Hugoniot equation:

$$(P - P_0) = \rho_0 U_s U_p.$$

Similarly, based on the conservation of energy, the change of internal energy $EV - E_0V_0$ will be given by the amount of compression work done by the piston $P\mathrm{d}V$ (neglecting phase transitions), and the kinetic energy $\frac{1}{2}mU_p^2$ imparted. Equating these and dividing by $A\mathrm{d}t$ results in

$$E\rho\left(U_s - U_p\right) - E_0\rho_0 U_s = PU_p - \frac{1}{2}\rho\left(U_s - U_p\right)U_p^2$$

and, solving for the change of specific energy using the specific volume $v = \frac{1}{\rho}$, yields the 3rd Rankine-Hugoniot equation:

$$E - E_0 = \frac{1}{2}\left(P + P_0\right)\left(v_0 - v\right).$$

The three Rankine-Hugoniot equations are independent yet contain five unknowns. To unambiguously find parameters as a function of only one other in order to predict the behaviour of shock compressed systems, another constraint is required, which commonly is referred to as Equation of State; unintuitively, this only determines the Hugoniot, rather than any other part of the phase diagram. One route is to relate the shock to the particle velocity through the polynomial expansion

$$U_s = v_s + S_1U_p + S_2U_p^2 + ...$$

where the ambient speed of sound v_s and the S_i are are tabulated parameters. This is the empirical formula used to find the piston velocities required to obtain the high pressure states in the molecular dynamics simulations presented in Chapter 3.

One such prediction commonly sought after is the final pressure state reached as a function of specific sample volume, which is referred to as the Hugoniot. For an initial tuple of pressure and volume, it describes the thermodynamically allowed states that can be accessed through a single shock.

2.3 X-Ray Physics

Investigating the behaviour of crystals, where characteristic length scales are on the order of Å, requires probes with extreme spatial resolution. Most commonly, this is done with photons, electrons, or neutrons. Whilst the de Broglie wavelength of electrons and neutrons even for moderate kinetic energies is on the order of most lattice spacings, x-ray photons do not suffer from the limited surface sensitivity of electron diffraction as seen in Transmission Electron Microscopy, nor require as large of a sample volume as neutron scattering experiments do.

2.3.1 X-Ray Free Electron Lasers

There are numerous natural and man-made sources of x-rays, such as astronomical objects like neutron stars or supernovae, cathode rays as used in medical imaging, or radiation at synchrotrons. In the field of ultrashort lasers, development on high harmonic generation in gases expanded the field of table top lasers into the extreme ultraviolet regime, bordering soft x-rays. Whilst any of these come with various up- and downsides such as potentially low flux, little beam control, or elaborate and costly setups, the sources adequate for the work in this thesis are X-ray Free Electron Lasers[121] (XFELs). These provide short, pulsed radiation of extreme brilliance, also called spectral brightness. For an x-ray source propagating in z-direction it is defined as the incident photons per second per solid angle per sources area

per frequency interval through

$$B = \frac{\dot{N}}{\mu_x \mu_y \sigma_x \sigma_y \, 0.1\% \cdot \Delta\omega}$$

with the $\dot{N}$ photons per second, the beam divergence μ_i in mrad, the source size σ_i in mm, and its bandwidth $\Delta\omega$[158].

On a high level, an XFEL can be divided into two parts: an electron injector into a linear accelerator followed by a undulator. The latter acts like a laser gain medium with single pass operation. Due to the linear acceleration and single pass cavity, the physical extent of these sources is on the order of kilometres, which partially is due to the lack of efficient reflective optics in the x-ray regime.

The linear accelerator produces a relativistic electron beam in the GeV range at a radio frequency repetition rate, which is designed to be of minimal spatial extent to provide a confined gain medium. Then, the electron beam enters the undulator part of the XFEL, where strong alternating magnets of undulator period λ_u divert the electrons through the Lorentz force back and forth on a superimposed trajectory perpendicular to their initial direction of propagation. Finally, the electron beam gets diverted and dumped. Beforehand, they oscillate at a frequency of $\omega_u = \frac{2\pi c}{\lambda_u^e}$, where $\lambda_u^e = \frac{\lambda_u}{\gamma}$ is the Lorentz contracted undulator length seen by the relativistic electrons. These periodic lateral diversions (accelerations) give rise to synchrotron radiation through spontaneous emission centred at λ_u^e in the electron frame. After boosting back into the laboratory frame, the wavelength of the generated radiation is $\frac{\lambda_u}{2\gamma^2}\left(1 + \frac{K^2}{2}\right)$[118, 119], with K a function of the undulator parameters. Typically, for electrons with kinetic energies on the order of tens of GeV and undulator spacings of a couple of centimetres, this corresponds to radiation on the order of keV, where the wavelength can be tuned over a wide range of energies[120].

The emission of synchrotron light of electrons in the accelerator bunches is inherently a stochastic process and the generated x-rays through spontaneous emission are incoherent.

However, due to a effect called 'bunching' the electrons in the electromagnetic field of undulator and radiation, that are initially smoothly distributed within a continuous accelerator bunch, influence each other through their emitted photons, experience a slight drift, and spatially group up, forming so-called microbunches along the XFEL axis with a period of λ_u^e. This amplifies the x-ray signal and is referred to as self-amplified spontaneous emission (SASE). The overall repetition rate of the XFEL will be given by the radio frequency of the linear accelerator and the bunch substructure. The temporal extent of each microbunch will determine the lowest pulse duration (typically on the order of a few tens of fs).

An even better temporal coherence is achieved through self-seeding, where after a few undulators, the electron beam is diverted, and the initial x-ray photons monochromated by a diamond crystal. A higher order of the transmitted monochromatised component (temporally later than the lowest reflection order) provides extremely monochromatic residual photons, that are recombined with the electron beam and act as the seed in the following undulators to obtain a very narrow bandwidth[159, 160].

The EuXFEL, a XFEL located in Hamburg with an approximate length of about 3.4 km in total, provides x-rays in a range of 0.25 to 25 keV with a peak brilliance on the order of $5 \cdot 10^{33} \frac{\text{photons}}{\text{s}\,\text{mm}^2\text{mrad}^2 0.1\%\Delta\omega}$. It operates at a linear accelerator repetition rate of 10 Hz with a 220 ns intra-bunch pulse spacing and up to 2700 pulses per bunch at 10 to 200 fs pulse duration, whilst, at 7.5 keV, its SASE full-width-half-maximum (FWHM) is about 20 eV. This can be improved down to about 1.2 eV upon self-seeding operation.

2.3.2 Compton and Thomson Scattering

Apart from absorption, x-rays in the keV regime primarily interact with matter via Compton scattering, which in the low energy limit is referred to as Thomson scattering. For Compton

scattering, the change of the x-ray wavelength λ_0 is described by

$$\lambda - \lambda_0 = \frac{h}{m_e c} \left(1 - \cos\Theta\right),$$

with the wavelength λ after scattering, the electron rest mass m_e, the speed of light c, and the scattering angle Θ. For photon wavelengths long compared to the effective Compton wavelength, the scatter process can be described as elastic and the Thomson cross section for a free electron is

$$\frac{d\sigma_e}{d\Omega} = \left(k'/k\right)^2 \left(\frac{e^2}{4\pi\epsilon_0 m_e c^2}\right)^2 \left|\boldsymbol{\epsilon}_\alpha^* \cdot \boldsymbol{\epsilon}_\beta\right|^2$$
$$\sigma_e = \frac{8\pi}{3} r_e^2$$

with the incoming $\mathbf{k}$ and scattered photon momentum $\mathbf{k}'$, the elementary charge e, vacuum permittivity ϵ_0, the polarisation $\boldsymbol{\epsilon}$ of the incoming α and outgoing β photon mode, and the classical electron radius $r_e = \frac{e^2}{4\pi\epsilon_0 m_e c^2}$. For linearly polarised x-rays, the second line describes the average cross section of a free electron radiated into 4π.

The Thomson differential cross section in matter is given by

$$\frac{d^2\sigma}{d\Omega dE'} = \left(k'/k\right)^2 r_e^2 \left|\boldsymbol{\epsilon}_\alpha^* \cdot \boldsymbol{\epsilon}_\beta\right|^2 S(\mathbf{Q}, \omega) \tag{2.5}$$

where the specific structure factor $S(\mathbf{Q}, \omega)$ describes the correlation between the scatterers (i.e., atoms). In case of solids, it can be split into a contribution of elastic and inelastic scattering

$$S(\mathbf{Q}, \omega) = S_E(\mathbf{Q}, \omega) + S_I(\mathbf{Q}, \omega), \tag{2.6}$$

whilst the overall scattering process can involve contributions from either one of these.

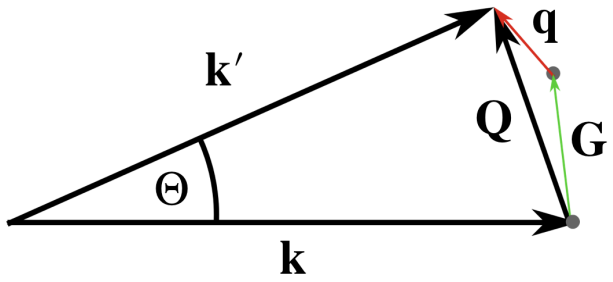

Figure 2.5: Scattering triangle of Thomson scattering. An incoming photon of $\mathbf{k}$ is scattered by an angle of Θ into direction $\mathbf{k}'$, changing its momentum by $\mathbf{Q} = \mathbf{G} + \mathbf{q}$, the combined effect of lattice and phonon scattering.

Hereby, as sketched in Figure 2.5, the photon of momentum $\mathbf{k}$ is scattered at an angle Θ into $\mathbf{k}'$ and changes its momentum by

$$Q \approx 2k \sin \frac{\Theta}{2}$$

with the scattering vector $\mathbf{Q} = \mathbf{k} - \mathbf{k}' = \mathbf{G} + \mathbf{q}$, where $\mathbf{G}$ describes the elastic lattice and $\mathbf{q}$ the inelastic phonon contribution. The magnitude of $\mathbf{k}$ and $\mathbf{k}'$ is almost equal given the negligible phonon energy is tiny compared to the photon energy.

2.3.3 Elastic Scattering in Ordered Structures

Elastic scattering commonly is referred to as Bragg (in reflection) or Laue (in transmission) diffraction and in monatomic crystals[31] is described by

$$S_E(\mathbf{Q}, \omega) = \frac{Z^2}{\hbar} f^2(\mathbf{Q}) e^{-2W} \left[\sum_m \exp i\mathbf{Q}\mathbf{r}_m \right] \delta(\omega) \tag{2.7}$$

where Z is the atomic number of the sample, $f(\mathbf{Q})$ the atomic form factor, W the Debye-Waller factor, m runs over each atom in the sample, and ω is the photon angular frequency. Evaluating Equation 2.7 for the immense number of atoms present in relevant samples is a significant computational challenge and thus usually only possible for short times and small

samples. However, it can be seen that due to interference, the elastic contribution to the diffracted intensity depends on the coherent sum of scattering signal of each individual scatterer, e.g., each atom at position $\mathbf{r}_m$, weighted by a relative phase factor. The bracketed expression in Equation 2.7 mathematically is just the Fourier transform of the atomic positions in $\mathbf{Q}$, and in the case of a perfect monatomic crystal an infinite three-dimensional grid of δ-functions in reciprocal space, i.e., the Bragg peaks as commonly found in single crystal diffraction, described through

$$S_E(\mathbf{Q},\omega) = \frac{Z^2}{\hbar} f^2(\mathbf{Q}) e^{-2W} \left[\frac{L^3}{(2\pi)^3} \sum_{\mathbf{G}} \delta(\mathbf{Q}-\mathbf{G}) \right] \delta(\omega)\,, \tag{2.8}$$

with the sample extent L and the reciprocal lattice vector $\mathbf{G}$. In experiments with polycrystalline samples, Debye-Scherrer rings will be found. This is consistent with Bragg's law, which states $2d_{hkl}\sin\frac{\Theta}{2} = n\lambda$ with integer n and the x-ray wavelength λ.

Hereby, since the $\mathbf{G}_{hkl}$ often are based on the conventional unit cell, the set of allowed diffraction planes is non-trivial for most crystal systems due to inference within the unit cell. Whilst Equation 2.8 contains the Fourier transform of the whole lattice made up of individual atoms, the system can also be described as an infinite lattice of conventional unit cells with a basis consisting of n atoms. According to the Fourier convolution theorem, the structure factor then is proportional to the convolution of all conventional Bragg δ-peaks with the Fourier transform of the unit cell. The latter is given by

$$S_E(\mathbf{G}) \propto \sum_j \exp\left(i\mathbf{G}\mathbf{r}_j\right)$$

and modulates the Bragg peak intensities; particularly, it can vanish. Substituting in the

relative atomic positions from Section 2.2.1 will yield

$$\begin{aligned} S_E(\mathbf{G}) &\propto \sum_j \exp\left(i\left[h\mathbf{b}_1 + k\mathbf{b}_2 + l\mathbf{b}_3\right] \cdot \left[x_j\mathbf{a}_1 + y_j\mathbf{a}_2 + z_j\mathbf{a}_3\right]\right) \\ &\propto \sum_j \exp\left(2\pi i\left[hx_j + ky_j + lz_j\right]\right) \end{aligned} \tag{2.9}$$

with the $r_j = \left(x_j, y_j, z_j\right)$ and where the property $\mathbf{a}_i \cdot \mathbf{b}_i = 2\pi\delta_{ij}$ was used. For the example of a fcc lattice, this reduces to the sum over the four atoms as

$$\begin{aligned} S_E(\mathbf{G}) &\propto \sum_j \exp\left(2\pi i\left[hx_j + ky_j + lz_j\right]\right) \\ &\propto \exp\left(2\pi i\left[h\cdot 0 + k\cdot 0 + l\cdot 0\right]\right) + \exp\left(\pi i\left[h\cdot 0 + k\cdot 1 + l\cdot 1\right]\right) \\ &+ \exp\left(\pi i\left[h\cdot 1 + k\cdot 0 + l\cdot 1\right]\right) + \exp\left(\pi i\left[h\cdot 1 + k\cdot 1 + l\cdot 0\right]\right) \\ &\propto 1 + (-1)^{k+l} + (-1)^{l+h} + (-1)^{h+k}\,. \end{aligned}$$

This describes the fcc selection rules of a finite $S_E(\mathbf{G})$ for h, k, l being all odd or all even, and $S_E(\mathbf{G}) = 0$ otherwise. In Table 2.1, the allowed diffraction peaks for the most common crystal structures are shown.

Structure	Finite $S_E(\mathbf{G})$	Vanishing $S_E(\mathbf{G})$
sc	All h, k, l	None
bcc	$h + k + l$ even	$h + k + l$ odd
fcc	All h, k, l odd or even	All others
fcdc	All h, k, l odd, or even and $h + k + l$ divisible by four	All others
hcp	l even and $h + 2k$ not divisible by three	All others

Table 2.1: The diffraction selection rules based on Equation 2.9 for the most common crystals.

Further than interference of atoms in the conventional unit cell and different crystallite orientations within the sample, the overall crystallite shape affects the diffraction signal. A finite crystal spanning the volume C, i.e. atoms in a periodic lattice of finite extent, can be

understood as the product of an infinite perfect crystal and a shape function defined as

$$g_S(\mathbf{r}) = \begin{cases} 1 & \text{if } \mathbf{r} \in C \\ 0 & \text{if } \mathbf{r} \notin C. \end{cases}$$

According to the Fourier convolution theorem, the Fourier transform of this product, i.e., inserted into equation 2.7, is equivalent to the convolution of the Bragg peaks with the Fourier transform of the shape function. Thus, the relative elastic intensity is found to behave as

$$S_E(\mathbf{Q}) \propto \sum_{\mathbf{G}} \widetilde{g}_S(\mathbf{Q} - \mathbf{G}) \tag{2.10}$$

with $\widetilde{g}_S$ the spatial Fourier transform of the shape function. This describes an infinite sum over $\mathbf{G}$, which is impossible to numerically evaluate. However, given most shape functions decay quickly in $\mathbf{Q}$, for most scattering configurations in the keV regime, it usually suffices to sum over a local reciprocal area. This deviation from sharp δ-peaks in reciprocal space gives rise to the quasi-elastic scattering (QES) relevant in this work.

2.3.4 Inelastic Scattering in Ordered Structures

Inelastic scattering (IXS) involves a phonon and in a perfect crystal is approximated[31] by

$$\begin{aligned} S_I(\mathbf{Q},\omega) = Z^2 f^2(\mathbf{Q}) e^{-2W} \frac{L^3}{(2\pi)^3} \sum_{\mathbf{q_0}j} \frac{|\mathbf{q}\cdot\mathbf{e}(\mathbf{q_0}j)|^2}{2m\omega_{\mathbf{q_0}j}} \\ \left\{ \left\langle n_{\mathbf{q_0}j} \right\rangle \delta(\omega + \omega_{\mathbf{q_0}j}) + \left(\left\langle n_{\mathbf{q_0}j} \right\rangle + 1 \right) \delta(\omega - \omega_{\mathbf{q_0}j}) \right\} \\ \sum_{\mathbf{G}} \delta(\mathbf{Q} \pm \mathbf{q_0} - \mathbf{G}) \end{aligned} \tag{2.11}$$

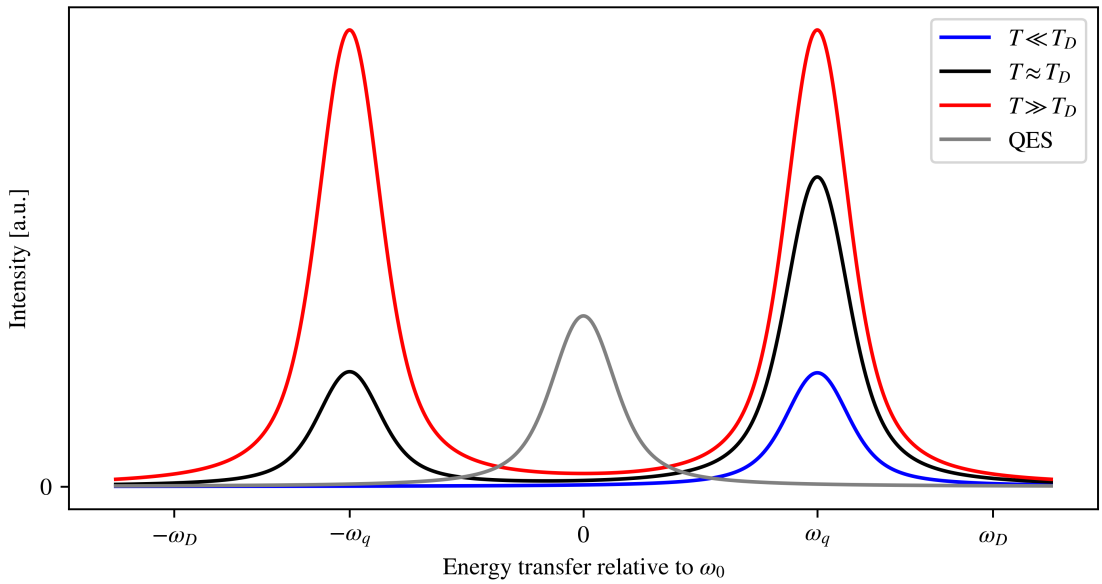

Figure 2.6: Detailed balance: Stokes (right) and anti-Stokes peaks (left) for a sample that is hot, cold, or close to its Debye temperature. Overlaid is a potential QES contribution. ω_D is the Debye frequency, the most energetic phonon frequency in the crystal, and ω_q the energy of the phonon involved in the scatter process.

with the phonon momentum $\mathbf{q}$, polarisation $\mathbf{e}$, and the atomic mass m. In crystals, IXS is much weaker than elastic scattering at the Bragg/Laue spots.

When dispersing the scattered beam of initial photon energy $\hbar\omega_0$ as shown in Figure 2.6, two distinct peaks arise due to the Stokes and anti-Stokes process. In the former, the x-ray photon creates a phonon of energy $\hbar\omega_q$ or in the latter, absorbs a pre-existent phonon and undergoes any energy upshift by $\hbar\omega_q$. This process is dependent on the Bose-Einstein factor and thus the absolute temperature of the sample. The relative intensity of the peaks provides a direct source of the absolute temperature via

$$\frac{I_1\left(\omega_0 - \omega_q\right)}{I_2\left(\omega_0 + \omega_q\right)} = \frac{\left\langle n_q \right\rangle + 1}{\left\langle n_q \right\rangle} = \exp \frac{\hbar\omega_q}{k_B T}. \tag{2.12}$$

Note that Figure 2.6 also shows a third peak, quasi-elastic scattering, which may be superimposed and can impair the temperature measurement principle featured in this work.

2.4 Scientific Computation

A large fraction of the work in Chapter 3 involves high-performance computing to simulate the behaviour of the metal crystals and analyse their signals. Hereby, as the computing power grows, so does the accessible range of physics, where, e.g., the spatial extent and duration of shock simulations can increase relative to past investigations. In addition, the analysis of noisy x-ray detector images applied in Chapter 4 and 5 is outlined below.

2.4.1 Molecular Dynamics Simulations

In the field of solid state and shock physics, there are numerous simulation methods to model and predict the physics observed in experiments. For static experiments, where the long-term time evolution is of no concern, stable crystal structure prediction includes Density Functional Theory (DFT), simulated annealing, and several Machine Learning implementations. Whilst for full quantum-mechanical treatment most systems quickly grow too large to be analytically or numerically handled, dynamic simulations covering compression and shocks add even more complexity and come at high computational cost (one structure per time step). This is why often, simplifications of the involved physics have to be made, and the systems are approximated by their dominant physics (at the price of reduced accuracy). Such methods include 'hydrocodes'[161, 162] (modelling the sample as a liquid with an average strength) and, most relevant to this work, MD simulations.

These classical simulations approximate the evolution of several millions of point-like atoms through numerically integrating Newton's equations. By knowing their positions and velocities, the forces acting on these particles are found through interatomic potentials. Hereby, only the equation of motion of the ions is solved, since, as the electrons are more than three orders of magnitude lighter than the nuclei and move much faster at the same temperature, for the electrons the nuclei are quasi-static and the electronic system quickly equilibrates even whilst the nuclei are moving, as described by the Born-Oppenheimer ap-

proximation. Hence, the electrons are modelled as an effectively time-independent potential governing the ion dynamics.

The Lennard-Jones potential was one of the first pair potentials used in MD simulations, given by

$$V(r) = 4\epsilon \left[\left(\frac{\sigma}{r}\right)^{12} - \left(\frac{\sigma}{r}\right)^{6} \right],$$

with the parameters ϵ, σ, and the interatomic distance r. The first term describes the steep repulsive force arising when atomic electron clouds begin to overlap, and the second term the long-range attractive van der Waals forces. Whilst it has limited applicability for metals, and all structures modelled with this potential assume a fcc configuration, its historical importance arises from its low computational cost and ability to reproduce some basic crystal properties.

Throughout this work, a potential based on the Embedded Atom Method (EAM) will be employed. For a monatomic system, it describes the potential energy V_i of ion i through

$$V_i = \frac{1}{2} \sum_{i \neq j} \phi\left(r_{ij}\right) + F\left(\sum_{i \neq j} \rho\left(r_{ij}\right) \right),$$

where r_{ij} is the distance between ion i and j, ϕ describes the pairwise interaction energy, F the embedding function describing the energy required to place ion i within the electron cloud of local density ρ. The latter usually is determined from the neighbouring atoms up to a certain cut off, whose individual electron densities are treated as isotropic (note that the Modified EAM incorporates an angular dependence yet at significant additional computational cost). Since the nuclei do not explore far away from their equilibrium positions, these element-specific potentials are fine-tuned and benchmarked with empirical data and can turn out to be good approximations of static properties up to pressures of several hundreds GPa (e.g., elastic constants, defect energies). Note that given their classical nature, the particle

velocities follow a Maxwell-Boltzmann distribution given by

$$f(v)\,\mathrm{d}^3v = \frac{1}{(2\pi)^{2/3}\,v_e^3}\exp\left(-\frac{v^2}{2v_e^2}\right)\mathrm{d}^3v$$

with $v_e = \sqrt{\frac{k_\mathrm{B}T_e}{m}}$, rather than the quantum-based Bose-Einstein distribution $\langle n\rangle$ that accurately describes the phonon population.

The MD suite used in this work is Large-scale Atomic/Molecular Massively Parallel Simulator (`LAMMPS`)[163], which is an open-source code that can be executed in parallel on computing clusters. It numerically integrates the Newtonian equations of motion of millions of atoms using a Verlet algorithm, ensuring that the number of particles, the volume of the simulation box, and the energy of the system are conserved.

2.4.2 Single Photon Counting

Here, a very basic routine[164, 165] to extract a scarce photon signal from pixel-based x-ray detectors is presented that was used in the collaborative p2191 experiment[145, 146] at the HED instrument of the EuXFEL as covered in Chapter 4 and 5.

In these experiments, 2D arrays containing the signal on the flat detectors made up of hundreds of thousands of micron-sized pixels are generated at a repetition rate of 10 Hz. Thus, efficient post-processing is required to inform the course of the experiments. Leveraging the low signal strengths (the 2D arrays are scarce in respect to the number of detected photons per image), a simple algorithm based on comparing the signal within the vicinity of a pixel can extract the single photon hits.

An x-ray photon of energy $\hbar\omega_0$ registered by a single pixel gives rise to an average signal of magnitude A. However, the photon can also excite multiple pixels, or spread across multiple pixels upon readout. Summing such smeared signal similarly produces average counts of A. Hereby, the noise floor of the camera systems employed in this work is on the order of

$20\% \cdot A$.

The simple algorithm employed scans the 2D array for any pixels above the noise floor. If the signal strength of the current pixel is $(1 \pm 0.2) \cdot A$, it is noted down in a separate array as single photon hit. Next, if the combined signal strength of the pixel and its eight adjacent neighbours is $(1 \pm 0.2) \cdot A$, the cluster is classified as a multi-pixel hit and the most intense pixel is noted down as a hit. Again, since the signal is scarce, multi-photon hits on the very same pixel or adjacent clusters are extremely rare and hence disregarded.

Chapter 3

Molecular Dynamics Simulations of Inelastic X-Ray Scattering from Shocked Copper

3.1 Introduction

Whilst previous MD simulations have been post-processed to provide simulated high-pressure diffraction (i.e. elastic scattering) patterns[125, 64, 126, 99, 166–168, 100, 169], little work has been reported which attempts to investigate inelastic scattering in this regime. The aim here is to provide a modest first step in this direction, assessing the feasibility of using x-ray inelastic scattering to gather information about the phonons present behind the shock front in a shocked single crystal. Note that extremely high plastic strain rates are present in such systems, indicating that copious dislocations and other defects are homogeneously generated at the shock front, and these have certainly been seen in previous MD simulations, where, for example, dislocation densities of order 10^{13} cm^{-2} have been reported for shock pressures of order 100 GPa[170, 171, 125, 66, 172–174]. Such a high density causes disruption to the perfect periodicity of the lattice on the length scale of tens of lattice spacings, raising the question as to the lifetime of coherent oscillations within the system, and thus whether distinct phonon modes can be observed. Furthermore, such defects, whilst mobile during the time that they are relieving shear stress, will by interrupting the lattice give rise to a quasi-elastic scattering signal, even when scattering is occurring far from a Bragg peak. Experimentally, this quasi-elastic scattering must be differentiated from the inelastic scattering from the phonons, potentially placing limits on the energy resolution required.

Whilst it will not be attempted here to address fully all of the above questions here, it will be shown for the chosen conditions that although copious defects are indeed generated when the crystal is shocked above the Hugoniot elastic limit (HEL), distinct phonon modes can still be discerned, though the phonon dispersion relation is, as expected, significantly modified

by the compression process. Furthermore, the defects present (in this case mainly stacking faults[175, 176]) do indeed give rise to a quasi-elastic signal that competes with the inelastic features. As will be shown below, at least for these single crystal simulations, the inelastic signal should still be discernible in the first Brillouin zone, but care needs to be taken if measurements are made beyond this region of reciprocal space, as the stacking faults present will, at least along certain directions, completely overwhelm the inelastic signal. Finally, it is noted that given the level of energy resolutions achievable, in an experimental signal the particle velocity of the compressed portion of the sample will give rise to a potentially measurable Doppler shift of the scattered x-rays that could be used as a further diagnostic of the system.

This chapter is laid out in the following manner. First, in Section 3.2 the parameters of the simulations, both in terms of the MD simulations themselves, are described and the Fourier transform methods employed. In Section 3.3 the results are presented, where plots of the simulated scattered intensity as a function of wavevector and energy transfer are provided, and also a pathway to obtaining the mean particle velocity behind the shock front via the Doppler effect is laid out. The implications of the results and proposals for further investigations are discussed in Chapter 6.

The simulations and their analysis within this chapter were designed and performed by the author, and are included in the manuscript Karnbach 2021[151] published in the Journal of Applied Physics.

3.2 Simulations

3.2.1 Molecular Dynamics Simulations via `LAMMPS`

All simulations were performed using the open-source code Large-scale Atomic/Molecular Massively Parallel Simulator (`LAMMPS`)[163] on a parallelised CPU cluster. The atomic re-

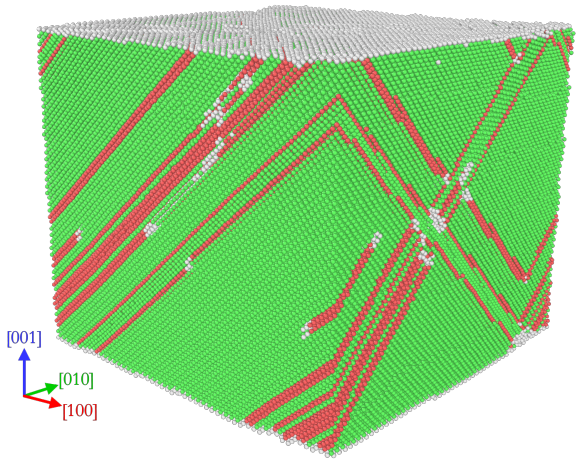

Figure 3.1: Section of the simulation box. The sample has been shocked along [001] to 30 GPa and exhibits stacking faults classified as hcp as highlighted in red. The bulk sample is in fcc configuration (green). The dominant types of one-dimensional defect are Shockley and Hirth dislocations according to the Dislocation Extraction Algorithm (DXA)[177].

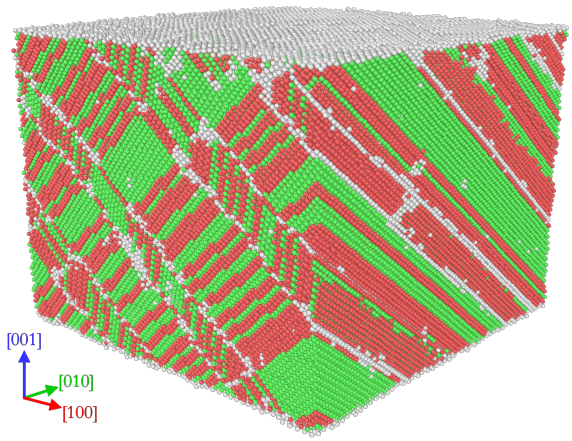

Figure 3.2: Section of the simulation box. The sample has been shocked along [001] to 70 GPa and exhibits stacking faults classified as hcp as highlighted in red. The bulk sample formerly primarily in fcc configuration (green) is dominated by defects and now consists in large part of hcp material.

sponse was modelled using the Cu EAM01 Mishin 2001 potential[178], which specifically was designed for high-pressure applications, accurately models dominant plasticity, e.g. stacking-fault energies, and hence is commonly used for shock simulations. The simulation box size was set to $50 \times 50 \times 455$ unit cells in the [100], [010], and [001] direction, respectively. The total of 4.55 million copper atoms were arranged in a perfect fcc lattice that was aligned with the coordinate system. In the x- and y-directions, the boundary conditions were periodic, whilst in the z-direction the boundary condition was left non-periodic to allow for compression.

The simulations were run with a time step of 1 fs and total duration of 30 ps. At first, the initialised fcc lattice is thermalised at 300 K for the first 2 ps under constant-NVE conditions, creating a realistic ambient crystal with temperature and pressure fluctuations on the order of ± 1 K and ± 0.5 GPa respectively. The crystal is then shock-compressed by driving a rigid piston consisting of $50 \times 50 \times 15$ unit cells at the lower z-edge, at fixed velocity, for 28 ps along [001]. The final pressure reached ranged from 0 to 70 GPa depending on the velocity of the piston (i.e. the particle velocity behind the shock front). The strain rates vary from $3 \cdot 10^{10}$ s^{-1} (10 GPa shock) to $6 \cdot 10^{10}$ s^{-1} (30 GPa shock) up to $9 \cdot 10^{11}$ s^{-1} (70 GPa shock). During the last approximately 8 ps of each of the 8 simulations, the real-space positions of all of the atoms in a central, fully shocked region of $50 \times 50 \times 50$ unit cells extent and an atom count of approximately 500,000 are saved ("dumped") every 32 fs; any further analysis will be only regarding these sets of atoms. The edge of the output box is approximately 50 unit cells distant from the piston, and its spatial extent is reduced for simulations with higher final pressure given the compression of the lattice, such that the number of dumped unit cells, and thus atoms, approximately stays the same.

The typical response of the crystal to the shock compression can be seen in Figures 3.1 and 3.2, where the atoms in the crystal have been colour-coded via a post-processing algorithm using the Ovito code[179], where the colours are assigned according to the common-

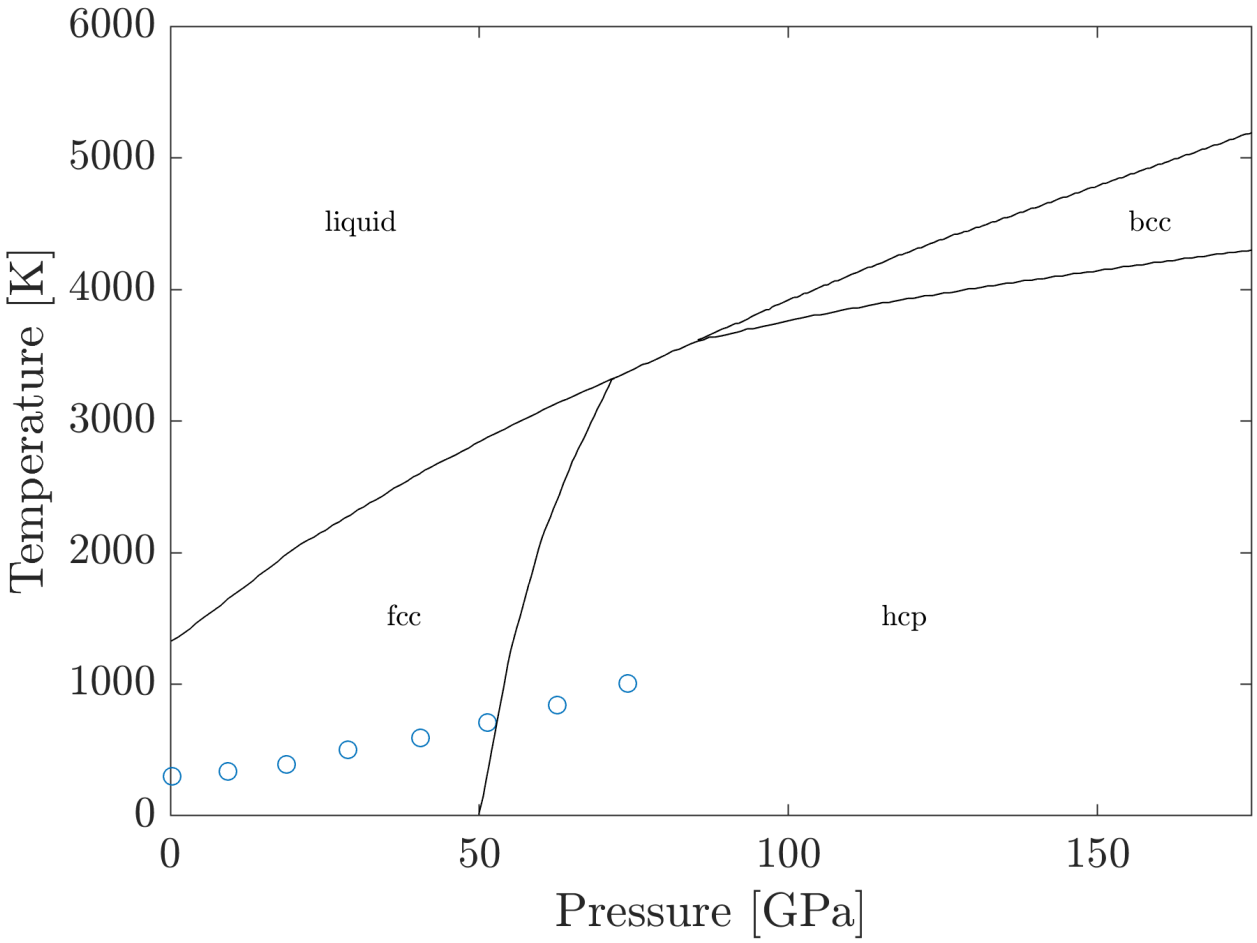

Figure 3.3: Phase diagram of Mishin copper[150] (black lines) with the pressure and temperature states reached in this work (blue circles). This correctly suggest a significant hcp phase above 50 GPa, yet given the directional shock nature of our MD simulations, the phase boundaries are only a rough indicator (compare with hcp and fcc fraction results listed in Table 3.1). Note that blue circles correspond to the 2D temperature in the $xy-$plane as calculated by `LAMMPS` through the kinetic energy, where the z-component is excluded due to the drift velocity of the centre of mass into z.

neighbour-analysis (CNA)[180–182] and the Dislocation Extraction Algorithm (DXA)[177], with atoms in an fcc environment being coloured green, and hcp atoms as red. The two plots shown correspond to pressures behind the shock front of 30 and 70 GPa, respectively. As has been found previously, for an initially perfect copper crystal the Mishin potential predicts an onset of shock-induced plasticity[183] (at the HEL) at around 30 GPa[184], with entirely elastic behaviour below this pressure. In Figure 3.1 this onset of plasticity is evinced by the appearance of stacking faults, which appear as thin regions of hcp material in the {111} planes. Furthermore, it is noted that for the Mishin potential employed here, a fcc-hcp phase boundary at a shock pressure of approximately 55 GPa has been found in a computational recrystallisation study[150]. This is illustrated in Figure 3.3, where the dynamically-reached pressure states featured in this work are plotted within the high-pressure Cu phase diagram. However, whilst in shock simulations, the fcc-hcp fraction saturates at equal fcc-hcp phase fraction at the highest pressures explored in this work (60 and 70 GPa) and no full fcc to hcp phase transition is found[185], during a shock the hcp material nucleated by plasticity can be thermodynamically similarly favourable as fcc, and thus forms extended bands of hcp material several atomic layers thick that cannot be realised by plasticity alone, as seen in Figure 3.2. Nonetheless, they shall be referred to these hcp bands as 'stacking faults' throughout, since the fcc phase fraction always exceeds the hcp phase fraction, or is on the same order of, for the shock pressures up to 70 GPa.

3.2.2 Modelling of the Elastic and Inelastic X-Ray Scattering

The approach to modelling the elastic and inelastic x-ray scattering from these shocked crystals is to take the space and time Fourier transform of their atomic coordinates as described by Equation 2.7. The intensity of x-rays scattered with change of wavevector $\mathbf{k}$

with an energy change of $\hbar\omega$ is calculated via

$$I\left(\mathbf{k},\omega\right)=\left|\sum_{j}\left(\sum_{i}\exp i\,\mathbf{k}\cdot\mathbf{r}_{i}\left(t_{j}\right)\right)\exp i\omega t_{j}\right|^{2} \tag{3.1}$$

with the atomic positions in real-space $\mathbf{r}_i$ and the simulation time steps t_j. Given the constraints of computational expense, calculation of the inelastic scattering (i.e. that which is a function of ω) is only undertaken along specific directions of interest in reciprocal space – i.e. in one dimension in reciprocal ($\mathbf{k}$) space, plus one dimension in frequency (ω) space. Such directions of interest can first be identified using calculations of the elastic scattering alone, which can be modelled from the atomic coordinates dumped at a single moment in time, but now calculated over a wide, three-dimensional volume of reciprocal space, as has previously been outlined in Warren[154] and is analogous to the calculations of Velterop[186] and Kimminau[187, 126, 188]. Note that the atoms are modelled with neither extent nor form factor, i.e. as 3D delta-functions in real space. In reality, a form factor arising from the spatially extended electron distribution will affect the long-range behaviour in reciprocal space, which in this work however is of lesser importance as for any given k-value this intensity-reducing effect identically affects both the elastic and inelastic signal alike.

It is noted that strictly speaking this approach cannot capture several aspects of the relevant physics, especially for the modelling of inelastic scattering. Firstly, phonons are quanta of vibrations of the normal modes of the lattice, and their discrete nature is not captured in a classical simulation. Secondly, in merely taking the temporal Fourier transform the creation and annihilation of phonons that occurs in the inelastic scattering process is completely ignored. However, it is contended that this approach still provides useful information, in that for modes with energies low compared with the thermal energy the classical amplitude predicted by the MD should be a good indicator of the expectation value of the quantum amplitude. Indeed, the use of classical MD simulations to identify and study physical pro-

cesses mediated by phonons is an established technique[189, 190]. As phonon creation and annihilation are not taken into account, the intensities of the Stokes and anti-Stokes peaks will not be related by detailed balance, which should be the case in practice. If desired, this could be mimicked by weighting the spectra as a function of k and ω by the factor[31] of

$$\frac{I\left(k,+\omega\right)}{I\left(k,-\omega\right)} = \exp\frac{\hbar\omega}{k_{\mathrm{B}}T}, \tag{3.2}$$

with the mode intensity I, the momentum transfer k, the mode energy $\hbar\omega$, the Boltzmann constant k_{B}, and the absolute temperature T in the sample, as introduced in Section 2.3.4. As this is trivial, and does not lead to any deeper understanding, this is not done in this work.

In undertaking these calculations, consideration must be given to the appropriate resolution in reciprocal space. Given that the largest spatial scale is that of the simulation box (which in reciprocal space will, as is seen, give rise to diffraction features itself), the spacing of the k-points in reciprocal space is chosen to be such that such size effects are resolved – i.e in this work $\Delta k \leq \pi/4L_i$, with L_i the simulation box extent in direction x,y, or z. For the inelastic scattering calculations the atomic positions were output every 32 fs for 8.192 ps and thus $N_{time} = 256$ data points were obtained at a sampling rate of 31.25 THz, yielding an energy resolution of 0.5 meV covering an energy range of $\pm$64.62 meV. To mitigate the influence of the finite time box, a periodic Hann window filter[191] is applied. Note that the finite mean velocity of the atoms in the shocked crystal (i.e. the particle velocity) will introduce a phase shift into the Fourier transform. In the results given below, this phase shift is removed, but on the observation of such a shift (which is related to the classical Doppler effect) will be commented on in Section 3.3.3.

3.3 Results

An example of such a calculation for the intensity of the elastic ($\omega = 0$) scattering is shown in Figure 3.4. Here the square modulus of the Fourier transform is plotted for a crystal shocked to 30 GPa (i.e. just above the HEL) as an intensity-threshold plot around the origin for a region in reciprocal space bounded by points with Miller indices $(\pm 3, \pm 3, \pm 3.45)$, where the indices are referenced to the ambient unshocked material. At this shock pressure the crystal has been compressed to 87% of its original volume.

This elastic scattering calculation exhibits several features of interest. Firstly, it is noted that from each of the intense points in reciprocal space streaks along the $\langle 100 \rangle$ directions (i.e. along the coordinate axes) are observed. This feature is highlighted at the origin of reciprocal space in the figure, by colour-coding it red. It is the artifact of the finite size of the simulation box in reciprocal space, i.e., in accordance with Equation 2.10, it is the well-known result that an orthorhombic shape in real space of dimensions L_x, L_y, L_z, will have a 'shape function' in reciprocal space that, in the vicinity of the reciprocal lattice vector $\mathbf{G}$, gives rise to a diffracted intensity

$$I(\mathbf{k}) \propto \left| \prod_{i=x,y,z} \operatorname{sinc} \left[\frac{L_i(k_i - G_i)}{2} \right] \right|^2 \quad , \tag{3.3}$$

which has prominent 'arms' along the $\langle 100 \rangle$ directions[154]. Indeed, the intensity in these directions due to the shape function of the box of atoms is so great that it overwhelms any thermal diffuse scattering. For the shocked crystals, the same intensity pattern will dress every reciprocal lattice point, which will have shifted owing to the crystal compression.

However, as well as this artifact due to finite size effects, lines of high intensity in reciprocal space can been seen linking certain reciprocal lattice points along different directions. Specifically, there is considerable intensity between some of the reciprocal lattice points along $[\bar{1}11]$ and $[11\bar{1}]$. This quasi-elastic scattering is associated with the planar stacking faults

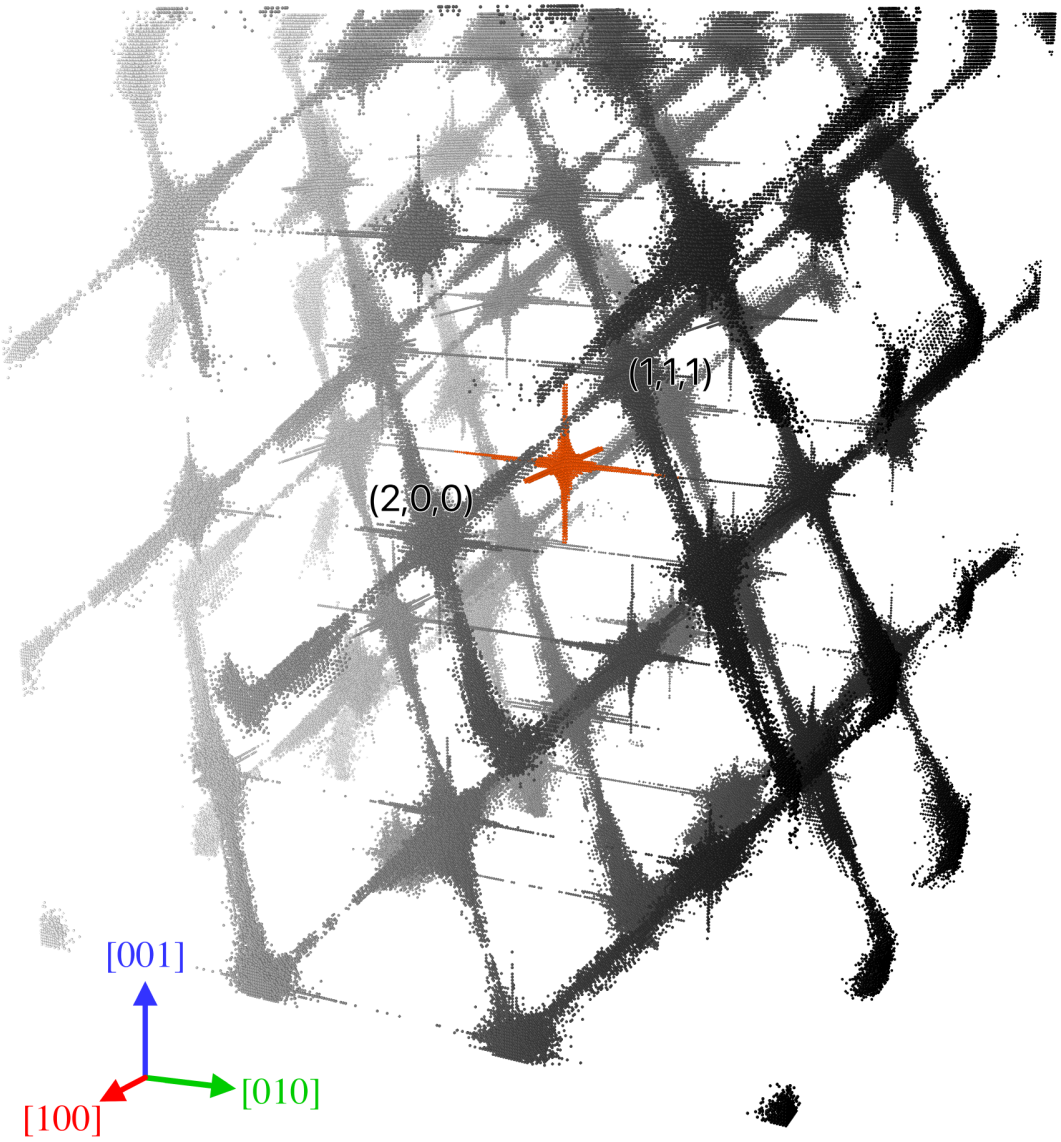

Figure 3.4: A calculation corresponding to the purely elastic scattering at a shock pressure of 30 GPa, obtained from the spatial Fourier transform of the atomic coordinates. The extent of the reciprocal space is defined by the two corners with Miller indices $\left(\bar{3}, \bar{3}, \overline{3.45}\right)$ and $(3, 3, 3.45)$. The colour scale threshold was chosen such that the Bragg peaks are clearly visible whilst the gradient from white to black indicates low to high [010]-coordinate. Intensity situated in the first Brillouin zone is colour coded in red. The fcc Bragg peaks in addition to stacking fault related diagonal streaks in $[\bar{1}11]$ and $[11\bar{1}]$ can be seen.

seen in Figures 3.1 and 3.2[192, 193]. The fact that particular points in reciprocal space will have a large streak in intensity emanating from them along directions associated with the normals to stacking faults is well known. As shown by Warren[154] and has been seen in previous atomistic and MD simulations[171, 192, 193], the phase shift, $\Delta\phi$, introduced into an x-ray as it traverses a stacking fault in the (111) plane is given by

$$\Delta\phi = \frac{2\pi}{3} n_{111} \left(h + k + l\right) \quad , \tag{3.4}$$

where n_{111} is the number of faulted planes. Analogous relations hold for the other stacking faults in the $\{111\}$ family of close-packed planes. Thus, linear streaks in reciprocal space caused by the disruption to the real lattice by the stacking faults are expected, along directions which are the normals to the stacking fault planes, for those reciprocal lattice points for which $\Delta\phi \neq 2m\pi$, where m is an integer. This is illustrated in Appendix A, where the reciprocal space for a perfect fcc crystal with a single stacking fault is plotted.

A study of Figure 3.4 shows that the main features are consistent with the above picture: strong scattering due to the stacking faults is not seen at the origin (where only the shape function is visible, at least at the threshold intensity in the plot) or, for example, around the reciprocal lattice points corresponding to $\{3, 3, 3\}$ in the unshocked system. As a result, such effects are not prominent in the first Brillouin zone. In contrast, strong elastic scattering due to the stacking faults can be seen close to, for example, reciprocal lattice points corresponding to $\{2, 0, 0\}$ in the unshocked crystal. This reduction in scattering due to these planar defects around lattice points for which $\Delta\phi = 2m\pi$ with integer m is referred to as the 'invisibility condition'[192]. As shall be found below, the density of stacking faults found in these shocked samples is actually so high, and the lattice so distorted, that the effects of the faulting can still be discerned, although at a level considerably reduced compared to the case where the invisibility condition is not satisfied.

To elucidate the above observations of this quasi-elastic scattering signal, and the effect

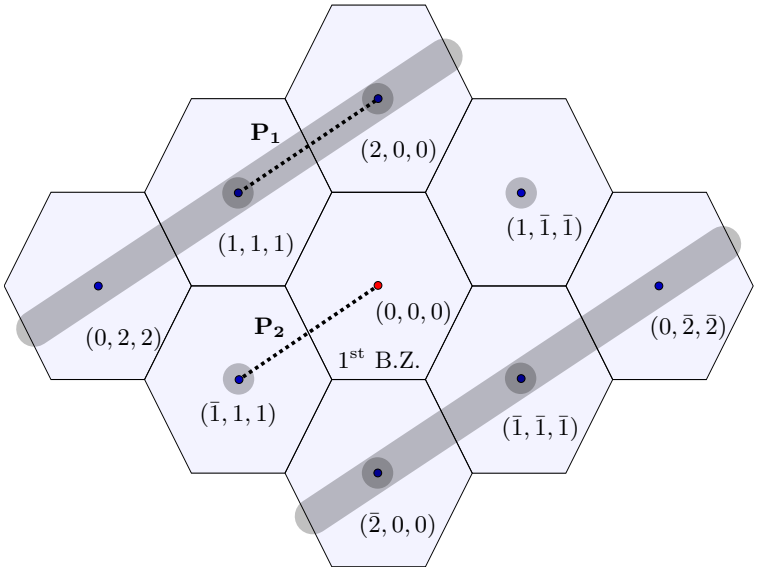

Figure 3.5: Two-dimensional schematic of Brillouin zones viewed in the $(0\bar{1}1)$ plane at 30 GPa. The origin $(0,0,0)$ is depicted in red. Dashed lines indicate the paths $\mathbf{P_1}$ and $\mathbf{P_2}$ along which spatiotemporal Fourier transforms are taken in this work. Grey shaded bars illustrate linear reciprocal-space features arising from $(\bar{1}11)$ faults. Grey circles indicate features in $[11\bar{1}]$ that protrude from the viewing plane.

that the stacking faults have upon it, the inelastic scattering along two high-symmetry paths in reciprocal space will be considered: the first path, which is labelled $\mathbf{P_1}$ in Figure 3.5, connects reciprocal lattice points $(2,0,0)$ and $(1,1,1)$ along the $[\bar{1}11]$ direction; the second path, $\mathbf{P_2}$, connects the $(0,0,0)$ and $(\bar{1},1,1)$ peaks. For an fcc crystal with perfect translational symmetry, in which all Brillouin zones are exactly equivalent, the reciprocal-space intensity along paths $\mathbf{P_1}$ and $\mathbf{P_2}$ would of course be identical. In the presence of the copious shock-induced stacking faults, however, $\mathbf{P_1}$ may coincide with an intense streak of quasi-elastic scattering. This signal – when it exists – arises specifically from stacking faults of the type $(\bar{1}11)$, whose invisibility criterion is failed by both $(2,0,0)$ and $(1,1,1)$ (and indeed by every reciprocal lattice point along the line passing through them). Path $\mathbf{P_2}$, by contrast, is permanently shielded from any such quasi-elastic signal because $(0,0,0)$ identically satisfies the invisibility criterion of every stacking fault variant. It thus becomes clear that quasi-elastic intensity detected between the Bragg peaks strongly depends on the Brillouin zone under

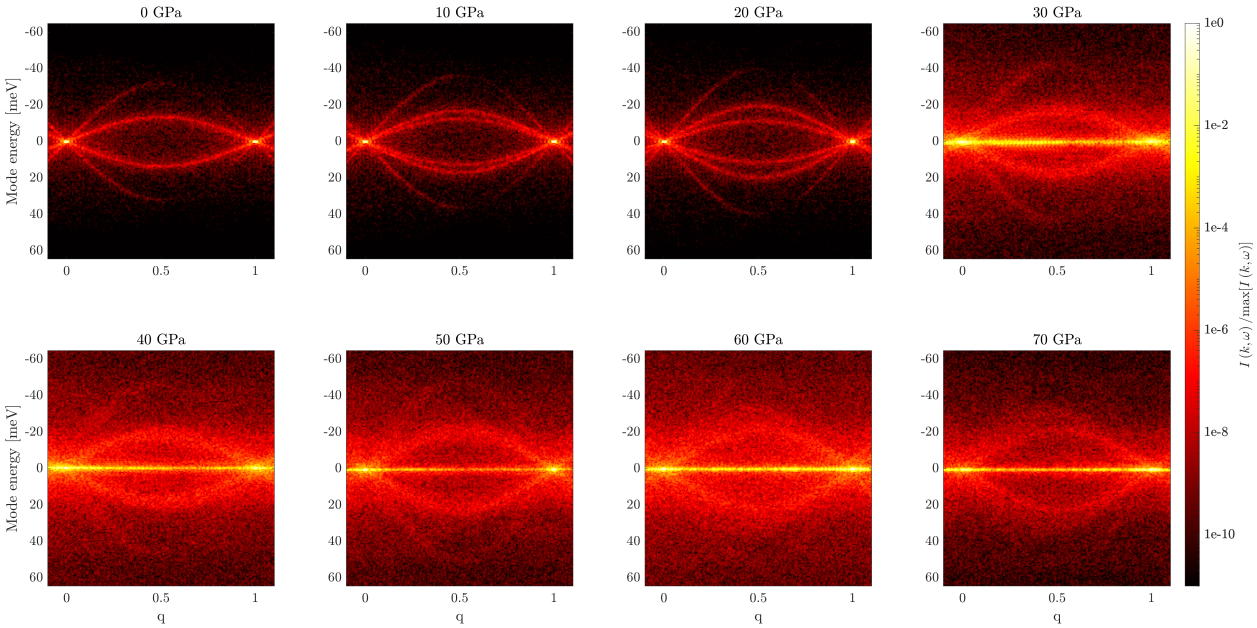

Figure 3.6: Spatiotemporal Fourier transforms along the path $\mathbf{k} = \mathbf{G}_1 + q(\mathbf{G}_2 - \mathbf{G}_1)$ connecting $\mathbf{G_1} = (\mathbf{2}, \mathbf{0}, \mathbf{0})$ and $\mathbf{G_2} = (\mathbf{1}, \mathbf{1}, \mathbf{1})$ in [001] shocked copper from 0 to 70 GPa. These peaks and various Stokes/anti-Stokes phonon modes are seen, as well as quasi-elastic x-ray scattering above the HEL, which for these perfect crystals is between 20 and 30 GPa. The logarithmic heat map indicates an increase of the absolute intensity of the spatiotemporal Fourier transform, normalised to the respective maximum intensity within each line-out. Explicit coordinates of the new reciprocal lattice vectors $\mathbf{G}_1$ and $\mathbf{G}_2$ for each shock pressure (accounting for the effects of lattice compression, plasticity-induced rotation, and stacking-fault-induced phase shifts) are given in Table 3.1.

investigation.

With this in mind, now the full spatiotemporal Fourier transforms of the crystal along paths $\mathbf{P_1}$ and $\mathbf{P_2}$ in reciprocal space will be examined. As shall be shown, the linear quasi-elastic features also have a signature that extends into the energy domain, which must be taken into account when considering inelastic scattering.

3.3.1 Phonon Modes under Shock Compression

To illustrate the significant impact of the stacking-fault features found in the {111}-directions, in Figure 3.6 the phonon modes along path $\mathbf{P_1}$ joining $(2, 0, 0)$ and $(1, 1, 1)$ for shock pressures between 0 and 70 GPa are shown using the method described in Section 3.2.2. The colour

scale indicates the intensity of a mode of energy $\hbar\omega$ with momentum $\hbar k$. At shock pressures below 30 GPa, distinct $(2,0,0)$ and $(1,1,1)$ Bragg peaks can clearly be observed along the zero-energy axis. Note that the effect of the star-like (triple-sinc-squared) shape function is only felt very close to the peaks, because in the {111} directions it decays extremely quickly. As the pressure is ramped up, the Bragg positions move in k-space, which is attributable to the shock-induced lattice compression, and, from 30 GPa onwards, to small plasticity-induced rotations[183, 68, 77] together with stacking-fault-induced phase shifts[154, 171]. These effects give rise to increased distances in reciprocal space between specific reciprocal lattice points along $\mathbf{P_1}$ and $\mathbf{P_2}$ in addition to apparent rotations of these paths of up to 3° – details of how paths $\mathbf{P_1}$ and $\mathbf{P_2}$ migrate due to compression and plasticity effects are shown for reference in Table 3.1.

P [GPa]	$\mathbf{G}_1 \left[\frac{2\pi}{a}\right]$	$\mathbf{G}_2 \left[\frac{2\pi}{a}\right]$	$\mathbf{G}_3 \left[\frac{2\pi}{a}\right]$	$\lvert\mathbf{P_1}\rvert \left[\frac{2\pi}{a\sqrt{3}}\right]$	$\lvert\mathbf{P_2}\rvert \left[\frac{2\pi}{a\sqrt{3}}\right]$	γ [°]	fcc [%]	hcp [%]	Other material [%]
0	$(2.00, 0.00, 0.00)$	$(1.00, 1.00, 1.00)$	$(\overline{1.00}, 1.00, 1.00)$	1.00	1.00	0	100	0	0
10	$(2.00, 0.00, 0.00)$	$(1.00, 1.00, 1.06)$	$(\overline{1.02}, 0.98, 1.04)$	1.02	1.02	0	99	0	1
20	$(2.00, 0.00, 0.00)$	$(1.00, 1.00, 1.10)$	$(\overline{1.02}, 0.98, 1.04)$	1.04	1.04	0	95	0	5
30	$(2.08, 0.01, \overline{0.10})$	$(1.12, 1.04, 1.00)$	$(\overline{0.98}, 1.02, 1.13)$	1.03	1.06	3	86	12	2
40	$(2.06, 0.06, \overline{0.09})$	$(1.12, 1.09, 0.95)$	$(\overline{0.98}, 1.06, 1.12)$	1.01	1.06	3	69	25	6
50	$(2.06, \overline{0.04}, 0.09)$	$(0.94, 1.02, 1.23)$	$(\overline{1.06}, 1.10, 1.11)$	1.11	1.07	3	51	38	11
60	$(2.02, 0.01, 0.04)$	$(1.04, 0.99, 1.30)$	$(\overline{0.98}, 0.98, 1.28)$	1.08	1.12	1	46	40	14
70	$(2.04, 0.04, 0.05)$	$(1.00, 1.00, 1.32)$	$(\overline{1.06}, 0.94, 1.26)$	1.10	1.12	2	10	79	11

Table 3.1: Reciprocal lattice points $\mathbf{G}_1 = (2,0,0)$, $\mathbf{G}_2 = (1,1,1)$, $\mathbf{G}_3 = (\bar{1},1,1)$, magnitude of paths $\mathbf{P_1}$ and $\mathbf{P_2}$ as shown in Figure 3.5, and apparent deflection angle of $\mathbf{G}_1$ relative to ambient $\mathbf{G}_1$ as function of pressure P. The reciprocal lattice points and distances are related to the ambient lattice constant a. The Bragg peaks move in reciprocal space due to shock-induced lattice compression, crystal rotations, and stacking fault phase shifts. Furthermore, the volume fractions of fcc, hcp, or unclassified material as a function of the final shock pressure within the dump box are given, determined using common neighbour analysis[180–182].

Above 30 GPa, there also exists between the Bragg peaks themselves a strong quasi-elastic signal along the zero-energy axis that arises from the presence of defects [namely the stacking faults of the kind $(\bar{1}11)$, which do not undergo significant changes on the lattice vibration time scale] whose pressure-dependent intensity is shown in Figure 3.7. Given that the distribution and abundance of {111} stacking faults vary between simulations, no

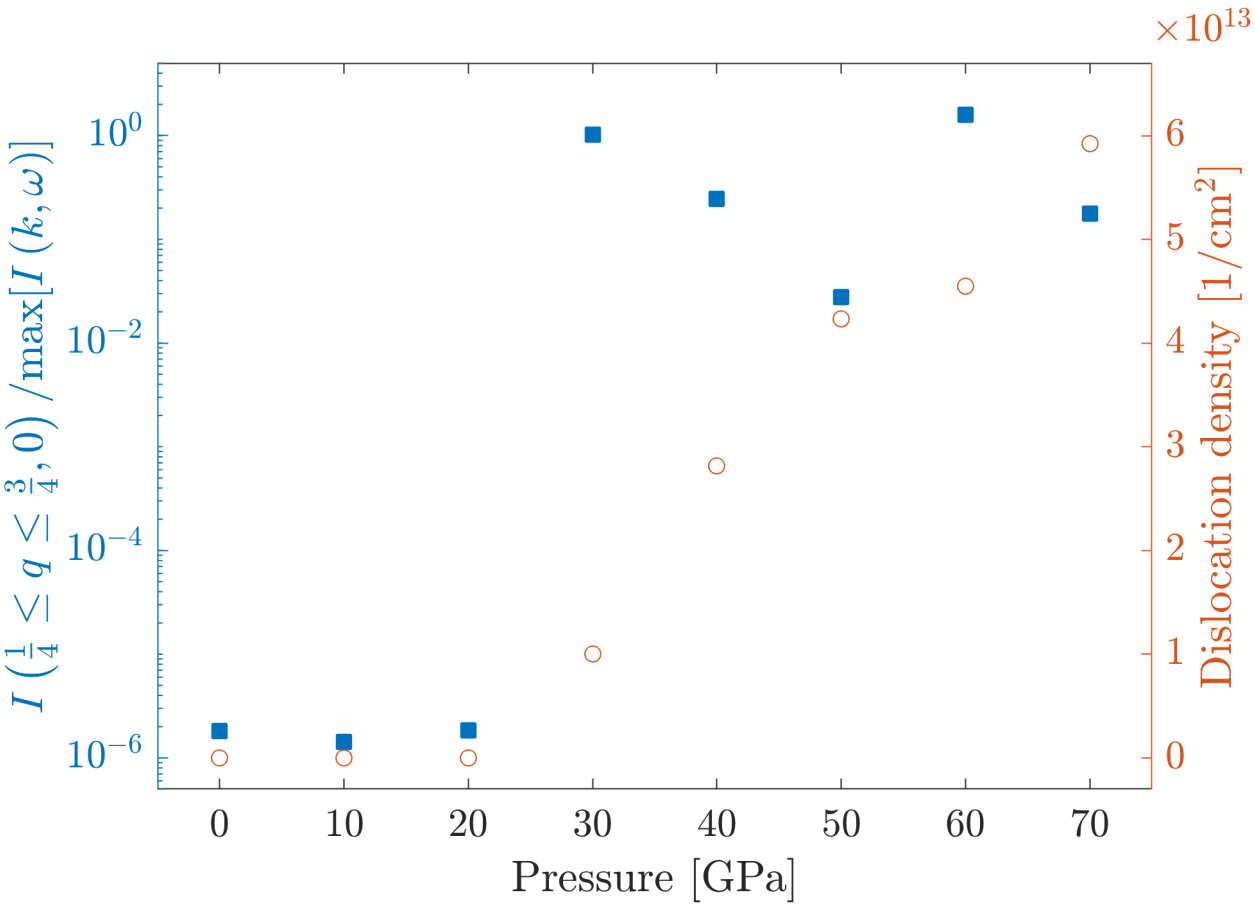

Figure 3.7: Central QES intensity (blue squares) and the density of any dislocation type within the dump box (red circles), as obtained by Ovito's DXA[179] as a function of the final shock pressure within the dump box. Prior to plasticity, the elastic scattering between the Bragg peaks is very low and the material primarily fcc. Once stacking faults and associated hcp appear, a sharp increase of QES can be found.

trivial pressure dependence of the plotted QES signal is found once the plastic regime is entered. Whilst the distinct jump between 20 and 30 GPa is clearly related to the sudden increase in defect density, only the binary relation can be resolved that once stacking faults in $(\bar{1}11)$ appear, the central QES signal increases by approximately five orders of magnitude relative to the ambient case; beyond this, the complex interaction of various defects and rotations means the signal strength along $\mathbf{P_1}$ in the plastic regime fluctuates by two orders of magnitude between different simulations.

As well as being connected by these quasi-elastic signals, the Bragg peaks are also linked

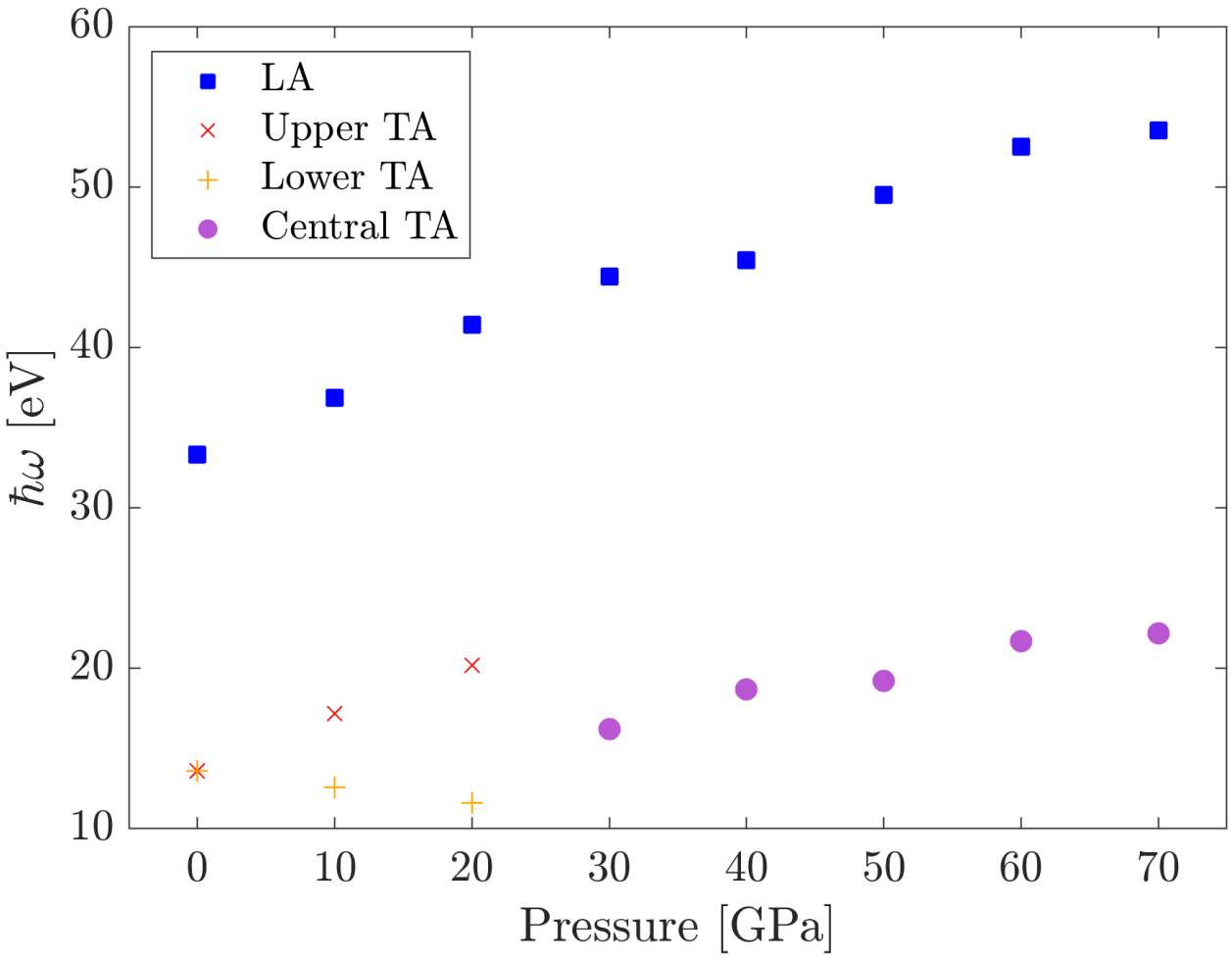

Figure 3.8: The Cu LA and TA phonons at $\left(\frac{3}{2}, \frac{1}{2}, \frac{1}{2}\right)$ are plotted as a function of final shock pressure. Due to the lattice being compressed along [001], the elastic constants increase and raise the phonon energy. In the elastic regime (below 30 GPa), the TA modes are split due to wavevector components along and perpendicular to the shock direction. Once plasticity arises, they can no longer be distinguished and the central mode of the TA band is shown.

up by arcs that span non-zero-energy regions of the spatiotemporal Fourier transform. These show the intensities of the classical Stokes- and anti-Stokes modes corresponding to the Cu [qqq] longitudinal-acoustic (LA) phonon (upper arc) and [qqq] transversal-acoustic (TA) phonon (lower arc). Compression of the crystal along its [001] direction causes its elastic moduli to increase via pressure hardening, which, in turn, causes the LA phonon energy to scale with shock pressure. This phenomenon is illustrated in Figure 3.8, in which the maximum energy of the classical modes at $\left(\frac{3}{2}, \frac{1}{2}, \frac{1}{2}\right)$ is plotted as a function of shock pressure.

It is noted in passing that the TA modes can be described by components oscillating in the (001) plane, and perpendicular to it in [001]. Hence, upon elastic compression of the crystal along [001], the associated loss of isotropy causes the TA modes to split into one approximately ambient component related to the (001) plane (lower TA), and one pressure-hardened component along [001] (upper TA). At 20 GPa, one can clearly distinguish two distinct TA modes because of the large anisotropy of the unit cell at approximately 5% elastic shear strain. Above the elastic limit, the plastic flow mediated by the stacking faults permits some fraction of the deviatoric elastic shear strains to relax and the residual shear strain is only about 1%. This lowers the elastic anisotropy of the crystal to such a degree that the two TA modes can no longer easily be distinguished, but instead form a continuum whose central frequency grows with pressure, much like the LA mode. The tendency of the phonon frequencies to increase with pressure should allow them to be more easily distinguished from the QES, a point to which shall be returned to in Section 3.3.2.

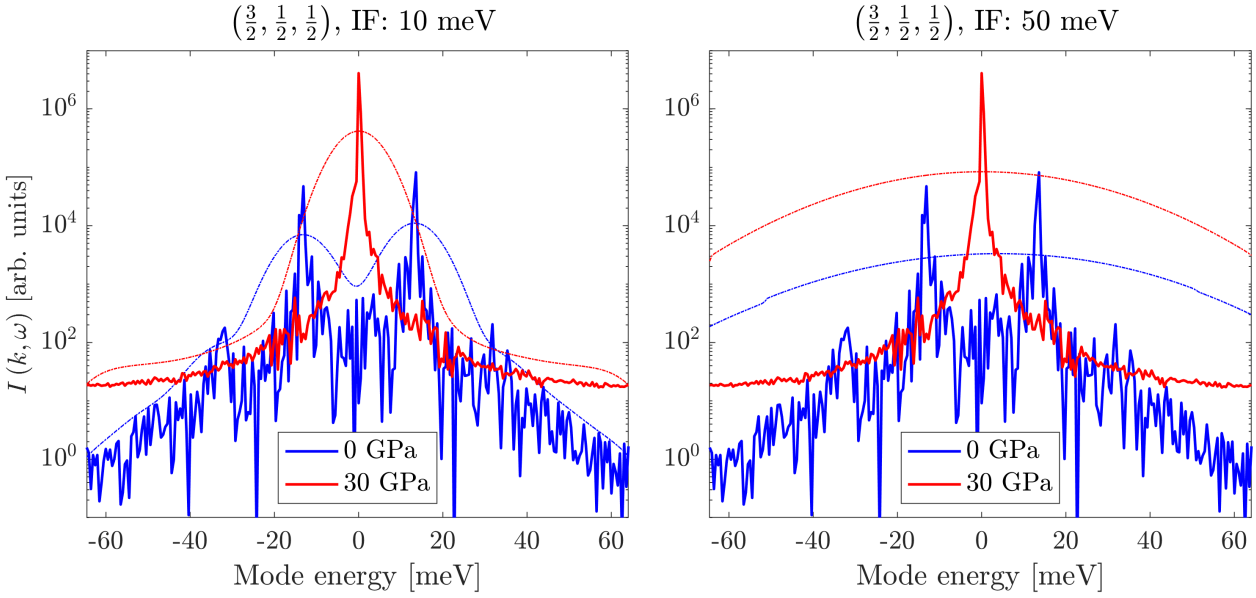

Figure 3.9: Line outs at $\left(\frac{3}{2},\frac{1}{2},\frac{1}{2}\right)$ for 0 and 30 GPa (solid line). The simulated signal is convolved with an Gaussian instrument function of FWHM 10 and 50 meV (dashed line). At 0 GPa, LA and TA phonons can be seen, whilst at 30 GPa intense QES linked to the stacking fault features dominates and only the LA modes are discernible. Note that for these energy resolution considerations no temporal Hann filter was applied.

In these shock simulations, the overall noise in the spatiotemporal Fourier transform increases at higher pressure due to a confluence of higher sample temperature, higher defect density, and also the emergence of the hcp phase (the volume fraction of which is shown in Table 3.1). When taken into consideration along with the aforementioned stacking-fault-induced QES, these plasticity effects can cause the phonon modes to become far harder to resolve at greater pressures. Such signal reduction could play an important role in real experiments, which is why next, the limiting effects of realistic instrument functions will be explored.

3.3.2 QES and Energy Resolution

Dynamical compression experiments involving laser-driven shocked samples probed using XFELs are of far-reaching interest to the HED physics community. The IXS technique represents another means of exploiting the power of the XFEL to diagnose material behaviour under extreme conditions. The method does, however, place stringent conditions upon the energy resolution required of the instrument used to collect the inelastic signal. The resolution in the simulations presented in this work is 0.5 meV, which is yet to be matched by dynamic experiments: at the IXS commissioning experiment of the HED end-station of the EuXFEL, the instrument function was on the order of 50 meV[146] – this has been and will continue to be further improved upon in the future at both the EuXFEL and LCLS. Whilst the influence of the instrument function on the scattering signal is in principle deconvolvable, shot noise poses a limit due to finite integration time at experiments. In this section, the spatiotemporal Fourier transforms calculated in Section 3.3.1 are used to estimate the kind of energy resolution required to distinguish the phonon modes in shock-compressed copper from the background QES owed to the copious defects.

In IXS geometries, usually photons that correspond to a small range of momentum transfer are recorded, which would correspond to a vertical line-out in Figure 3.6. For this reason,

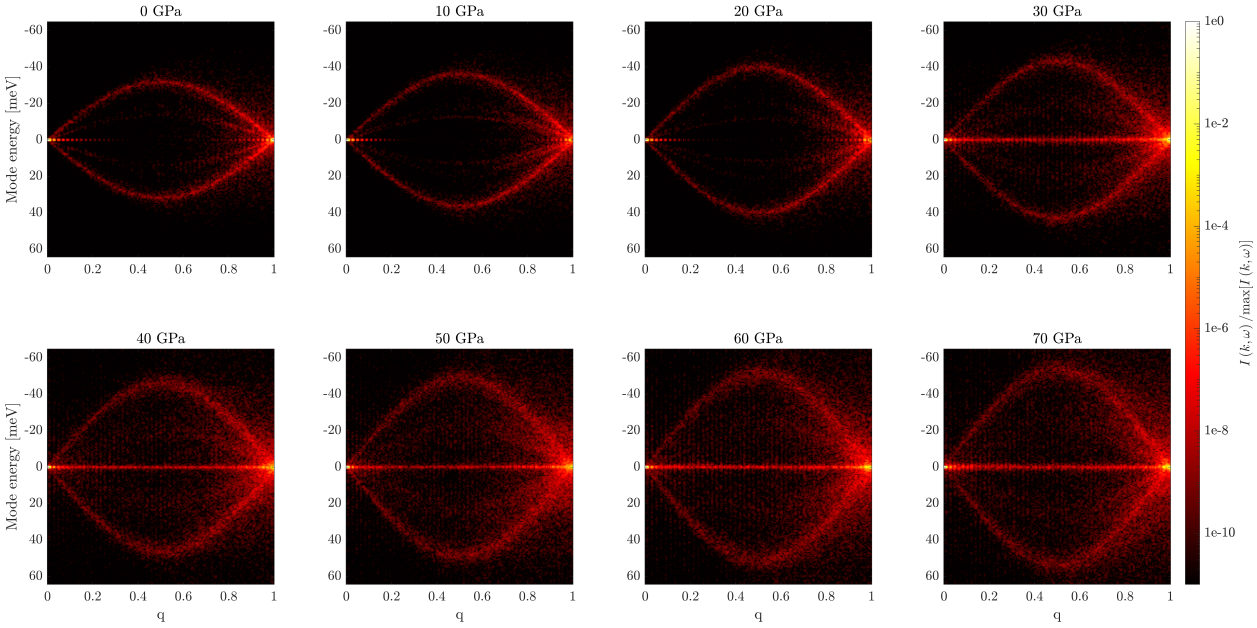

Figure 3.10: Spatiotemporal Fourier transforms along the path $\mathbf{k} = \mathbf{G}_0 + q(\mathbf{G}_3 - \mathbf{G}_0)$ connecting $\mathbf{G}_0 = (0, 0, 0)$ and $\mathbf{G}_3 = (\bar{1}, 1, 1)$ in [001] shocked copper from 0 to 70 GPa. These peaks and various Stokes/anti-Stokes phonon modes are seen, as well as quasi-elastic x-ray scattering above the HEL, which for these perfect crystals is between 20 and 30 GPa. The logarithmic heat map indicates an increase of the absolute intensity of the spatiotemporal Fourier transform, normalised to the respective maximum intensity within each line-out. Explicit coordinates of the new reciprocal lattice vector $\mathbf{G}_3$ for each shock pressure (accounting for the effects of lattice compression, plasticity-induced rotation, and stacking-fault-induced phase shifts) are given in Table 3.1.

in Figure 3.9 raw line-outs of the Fourier transforms along the energy axis are shown at a scattering vector of $\left(\frac{3}{2}, \frac{1}{2}, \frac{1}{2}\right)$ (i.e. at the midpoint of $\mathbf{P_1}$) for simulations at 0 and 30 GPa. Shown also are the same signals convolved with a normalised Gaussian of FWHM 10 (left) and 50 meV (right), whose purpose is to emulate the instrument function. The Stokes- and anti-Stokes peaks are, as expected, symmetrically spaced around the zero-energy modes. Given the classical nature of the simulations, aside from numerical fluctuations, their relative intensities are matched, and are not subject to the detailed balance described by Equation 3.2 – as mentioned previously, correcting for this detail is possible, but unnecessary for the purposes of the present study. The key question that will be addressed is whether these peaks can still be distinguished in the presence of the background QES.

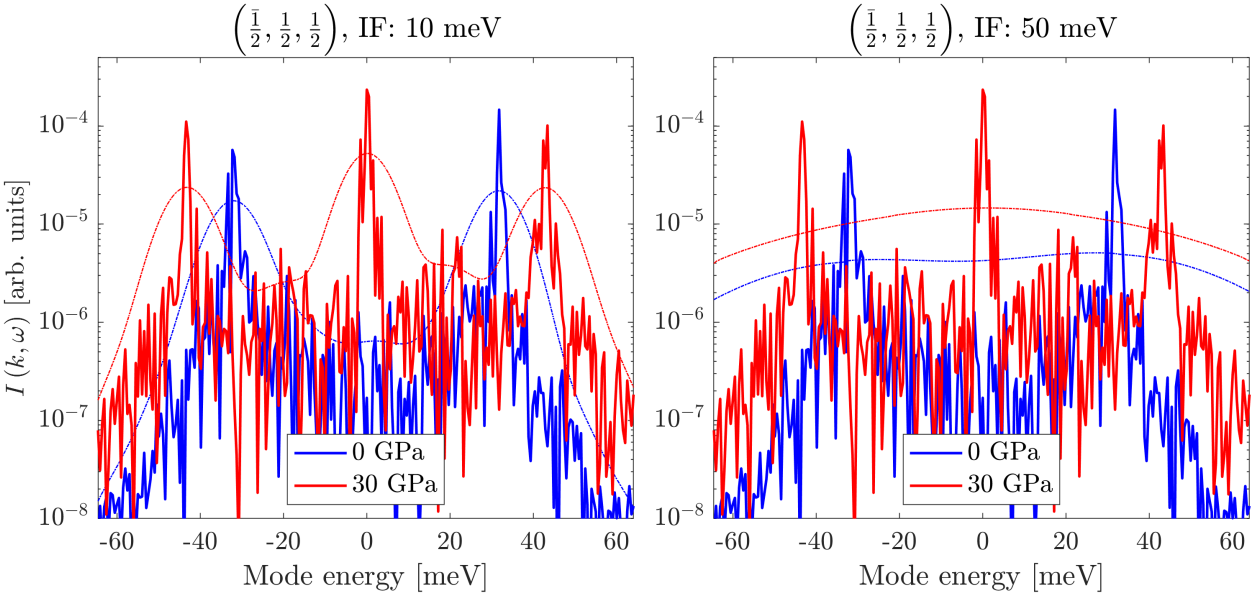

Figure 3.11: Line outs at $\left(\frac{\bar{1}}{2}, \frac{1}{2}, \frac{1}{2}\right)$ for 0 and 30 GPa (solid line). The simulated signal is convolved with an Gaussian instrument function of FWHM 10 and 50 meV (dashed line). At both pressures, LA and (faint) TA phonons can be seen, whilst in the plastic regime background QES linked to the increased disorder is also present. Note that for these energy resolution considerations no temporal Hann filter was applied.

At ambient pressure, peaks from the LA and TA phonons can be identified at approximately ±34 and ±14 meV respectively, while at 30 GPa (in the plastic regime) the QES arising from the stacking fault streaks overwhelmingly dominates the spectra, and only a faint TA signature can be made out at approximately ±15 meV. For an instrument function with FWHM 50 meV, phonons can be resolved in neither the ambient nor shocked case, and the signal is simply proportional to the total scattered photons. For an instrument function of just 10 meV FWHM, the TA modes *are* resolvable, but only under ambient conditions; the ambient LA modes, meanwhile, greatly suffer from noise due to their being in the second Brillouin zone (where the effects of stacking faults are large), and so remain unresolvable. Once the plastic regime is entered at 30 GPa, not even the TA phonons can be resolved thanks to the extremely intense QES, even with such high energy resolution. These spectra indicate that the presence of stacking faults could render measurement of phonon modes in the second Brillouin zone unfeasible, at least along these specific directions in the second

Brillouin zone in shock-loaded single-crystal copper.

However, as was illustrated in Figure 3.5, the stacking faults should not adversely affect the *first* Brillouin zone, which is why it is instructive to consider the same spectra obtained midway along $\mathbf{P_2}$, i.e. still along the $[\bar{1}11]$ direction, yet starting at the origin rather than $(2, 0, 0)$. The corresponding spatiotemporal Fourier transforms are illustrated in Figure 3.10. Just as in Figure 3.6, Bragg peaks are visible along the zero-energy axis [in this case, $(0, 0, 0)$ and $(\bar{1}, 1, 1)$] that are again connected by LA and TA modes. Once more, a splitting of the TA modes into two branches is visible in the elastic regime, becoming less distinct from 30 GPa onwards. Unlike those along path $\mathbf{P_1}$, the TA modes here in the first Brillouin zone are noticeably fainter than are the LA modes. The most striking difference between Figs. 3.10 and Figs. 3.6, however, is in the contrast between the classical modes and the QES: along path $\mathbf{P_2}$, the QES does not completely dominate the signal as it did along path $\mathbf{P_1}$. This, as explained in Section 3.3, is thanks to the origin satisfying the invisibility criterion for all four stacking fault variants.

In Figure 3.11 the corresponding raw line-outs and synthetic experimental spectra are shown at scattering vector $\left(\frac{\bar{1}}{2}, \frac{1}{2}, \frac{1}{2}\right)$, where the spectra are shown again for 0 and 30 GPa. The LA (TA) modes in this case are found at ± 34 (± 14) meV for 0 GPa and at ± 43 (± 16) meV for 30 GPa. A relatively weak yet still significant background QES is present, which may be due to the small but finite strains associated with the network of copious stacking faults and the general increased disorder in the plastic region behind the shock front. For the ambient crystal, the LA modes can be resolved with an instrument function as wide as 50 meV FWHM due to their higher energies compared with the dominant TA modes at $\left(\frac{3}{2}, \frac{1}{2}, \frac{1}{2}\right)$. However, the QES still dominates the synthetic spectra once the plastic regime is entered, and at 30 GPa no phonons can be resolved once again. For an instrument function of only 10 meV FWHM, however, the LA modes in both ambient and shocked copper can be measured, and at 30 GPa, even the effect of the TA modes on the spectrum can be

resolved. Ignoring the detrimental effect of the increased background QES that inevitably accompanies it, pressure hardening here is of great assistance: the inelastic peaks at higher pressure can be more easily identified due to the increased separation of the phonons in energy space – a crucial benefit conferred by the compression itself. In any case, these spectra indicate that, even within the first Brillouin zone, energy resolutions better than 50 meV will be required to perform IXS measurements of shock-loaded single crystal copper, at least along the directions studied.

3.3.3 Doppler Shift

As noted above, the current resolutions that have been demonstrated at 4th-generation light sources are in the region of 45 meV at a photon energy of 7.5 keV – i.e., a resolution better than one part in 10^5. In future developments, it is envisaged that the use of even higher photon energies – with even greater resolution – will be possible. Indeed, resolutions of order just a few meV (e.g. 3 meV at 17.79 keV) have been demonstrated in synchrotron settings[34]. It is important to note that the shock or ramp compression process will impart a bulk velocity shift to the compressed portion of the crystal – in the parlance of the shock community this is the 'particle velocity' (as opposed to the shock velocity at which the compression front moves). With the above spectral resolution, this bulk velocity will exhibit itself as a Doppler shift of the scattered signal whenever the collection geometry differs from pure forward scattering. In this final section, the prospects of exploiting this Doppler shift to experimentally measure the particle velocity behind the shock front is discussed.

Typically, for shocks in the 100 GPa range, the particle velocity U_p is several 1000 ms^{-1}, resulting in $\beta = U_p/c$ on the order of 10^{-5}, with c the speed of light in vacuum. This factor is sufficiently large that the relativistic Doppler effect will need to be taken into account when analysing the scattered signal: indeed, it will contain a direct measure of the particle velocity within the material. In these simulations, the bulk sample velocity U_p behind the

shock front equals that of the driving piston in [001], which could be 'corrected for' by transforming into the centre-of-mass frame of the shocked material. Without this correction, any spatiotemporal line-out with a component in [001] would experience a Doppler shift.

In general, for a given x-ray photon with energy $\hbar\omega_0$, the scattered frequency after absorption and re-emission is

$$\omega = \omega_0 \frac{1 - \beta \cos \Omega_a}{1 - \beta \cos \Omega_e}, \tag{3.5}$$

with angle of absorption Ω_a, and angle of emission Ω_e in the rest frame of the source and of the detector[194]. For a sample shocked to U_p in direction $\hat{\mathbf{n}}_s$ and probed by x-rays with incident and scattered wavevectors $\mathbf{k_0}$ and $\mathbf{k}$, the angle of absorption follows as $\Omega_a = \arccos \frac{\hat{\mathbf{n}}_s \cdot \mathbf{k_0}}{k_0}$, and the angle of emission as $\Omega_e = \arccos \frac{\hat{\mathbf{n}}_s \cdot \mathbf{k}}{k}$. Given that for x-ray Thomson scattering, the magnitude of the scattering vector $\mathbf{q}$ follows as $q = 2k_0 \sin \frac{\Theta}{2}$, this Doppler shift will hence be strongly dependent on the scattering angle[154]. Without loss of generality, setting

$$\hat{\mathbf{n}}_s = \begin{pmatrix} 0 \\ \sin\alpha \\ \cos\alpha \end{pmatrix} \qquad \text{and} \qquad \mathbf{k_0} = k_0 \begin{pmatrix} 0 \\ 0 \\ 1 \end{pmatrix}, \tag{3.6}$$

but subsequently confining scattering to the yz-plane, $\mathbf{k}$ reduces to

$$\mathbf{k} = \begin{pmatrix} k_x \\ k_y \\ k_z \end{pmatrix} = k \begin{pmatrix} 0 \\ \sin\Theta \\ \cos\Theta \end{pmatrix}. \tag{3.7}$$

This is illustrated in Figure 3.12, and in Table 3.2, a selection of such Doppler shift cases is shown. Note that this shift tends towards unity for direct forward scattering, for which the effects of absorption and re-emission cancel out. Typically, α is small, and thus the energy shift is most significant for back-scatter. Considering the example of copper at 100 GPa with $U_p = 1714$ ms^{-1} at $\alpha = 10°$, $\Theta = 30°$, and $\hbar\omega_0 = 7.5$ keV, as is typical for the

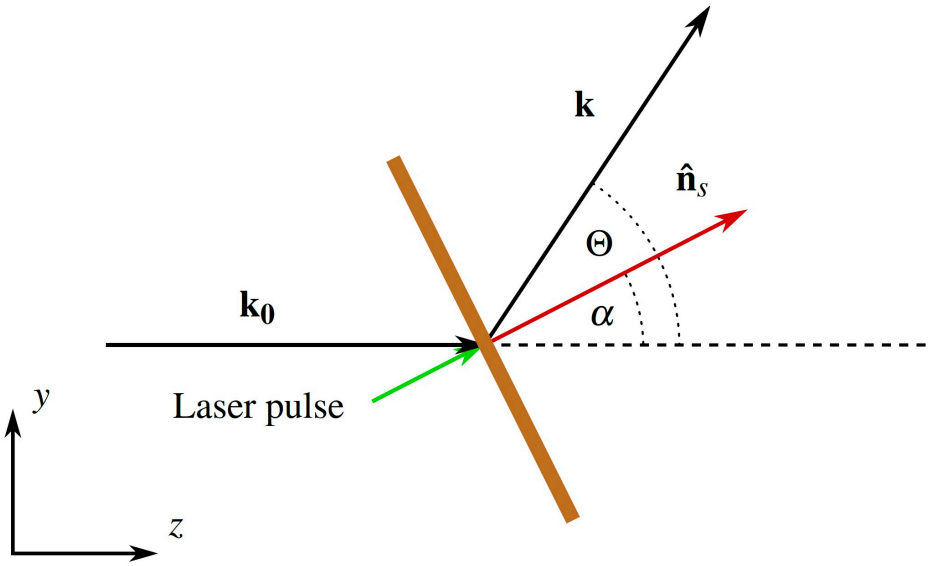

Figure 3.12: Scattering geometry for the particular case of incident x-rays with wavevector $\mathbf{k_0}$ scattered from a thin Cu foil into $\mathbf{k}$ in the $yz-$plane. The shock, e.g., arising from a short laser pulse (green), propagates in direction $\hat{\mathbf{n}}_s$ (red).

current EuXFEL HED configuration, this would cause a shift of just 2 meV. For back-scatter, however, at $\Theta = 170°$, this increases to 82 meV, significantly shifting the signal and providing the opportunity to directly extract U_p even with the current modest spectral resolutions of 45 meV. If higher resolutions in the sub-5-meV range could be obtained at FELs at the greater photon energies cited above, then particular velocities should be directly measurable with accuracies well below 100 ms^{-1}. Whilst this Doppler-shift approach to measuring particle velocity cannot compete with a standard VISAR diagnostic[132–134], it would give a velocity measurement *within* the material, without need for observation of motion of a boundary, and without making the assumption that the velocity at a free surface is twice the particle velocity. Furthermore, as it does not rely on optical reflection from a surface, such an approach would not be subject to 'blanking' due to poor reflectivity. These considerations illustrate that the Doppler effect in IXS could yet play an important role in the diagnosis of materials rapidly compressed by laser-ablation.

Shock angle α [°]	Scattering angle Θ [°]	$\frac{\omega}{\omega_0}$	$\Delta\omega$ [meV]
0	0	1	0
	90	$1-\beta$	-25
	180	$\left[\frac{1-\beta}{1+\beta}\right]$	-50
90	0	1	0
	90	$\left[\frac{1}{1-\beta}\right]$	$+25$
	180	1	0
	270	$\left[\frac{1}{1+\beta}\right]$	-25
180	0	1	0
	90	$1-\beta$	-25
	180	$\left[\frac{1+\beta}{1-\beta}\right]$	$+50$

Table 3.2: Doppler shift as function of the angle made by incident x-ray beam with the direction of the shock, α, and of the scattering angle, Θ, when the scattered beam is confined to plane spanned by $\hat{\mathbf{n}}_s$ and $\mathbf{k_0}$. The final column gives illustrative values for a particle velocity of 1 $\mathrm{km\,s^{-1}}$ and incident beam energy of $\hbar\omega_0 = 7.5$ keV.

3.4 Summary

In summary, this work has made two modest steps towards understanding the physics of shock experiments that use high-resolution IXS as a diagnostic. First, it was shown how and why quasi-elastic scattering can be a challenge when measuring phonons via inelastic scattering, particularly when intending to reliably determine the absolute temperature of shock-compressed material by trying to resolve the Stokes and anti-Stokes peaks. Second, it was demonstrated that through the shock-induced Doppler shift of the inelastic scattering signal, it should be possible to directly extract the yet-inaccessible net particle velocity behind the shock front.

The simulations presented here provide insight into a rich selection of physics. Upon shock, the phonon energies rise due to pressure hardening. The resulting enhanced separation of the Stokes- and anti-Stokes peaks proves experimentally to be advantageous, as it relaxes the energy resolution required to distinguish them. However, it also was shown that collecting photons between the Bragg peaks (in order both to maximise this phonon energy

and to avoid elastic scattering signal) can still be a challenging task when looking at defective matter traversed by stacking faults, which give rise to QES. In particular, the 3D spatial Fourier transforms show that certain regions in k-space are exceptionally affected, via linear features connecting certain Bragg peaks in higher Brillouin zones. Indeed, due to the overall increased disorder of the shock-compressed system, even within the first Brillouin zone there exists a background QES that could impair phonon measurements if the diagnostic's energy resolution were insufficiently great, at least along the particular directions studied. The simulations herein have provided an indication of the kind of resolution required to distinguish the inelastic peaks from the quasi-elastic signal threatening to swamp them (i.e. a few tens of meV).

To generate the spatiotemporal Fourier transforms shown in Figs. 3.6 and 3.10, the reciprocal-space paths along which the reciprocal space was probed were moved 'in sync' with the compression, in order that the paths always coincided with the Bragg peaks. For real experiments, however, it is more common to commit to one small, predetermined k-range. This could mean that the streaks drift through the detector range, potentially saturating any phonon signal in temporally integrating setups. That being said, whilst the $\langle 111 \rangle$-streaks caused by stacking faults can impair inelastic measurements, deliberately probing higher Brillouin zones so as to maximise such linear features could be utilised to make statements about the plasticity-induced microstructure of the shocked material.

Chapter 4

Photometrics of X-Ray Thomson Scattering

4.1 Introduction

Through inelastic x-ray Thomson scattering, it is possible to directly measure the temperature of solid materials via the principle of detailed balance as described in Chapter 3, Equation 3.2. Photons scattered by the phonons within a thin solid are collected at a certain scattering angle Θ by Spherical Diced Crystal Analysers[195–198] (DCAs) and thereby dispersed onto an x-ray detector. It is essential that the instrument function of the setup is narrow enough to resolve the phonon peaks that are on the order of a few tens of meV, provided these high-resolution (hr) spectra are not limited by shot noise. This is why, so far, previous work only has showcased static hr IXS, done at synchrotrons of high photon flux with long integration times of mere-continuous x-ray beams. This work is part of a collaboration for proposal p2191 and p2656 at the EuXFEL HED instrument, which extended the applicability of such temperature diagnostic into the dynamic regime using XFELs.

For well-behaved samples such as monocrystals, the signal relevant for the temperature measurement consists of only two peaks[145], the Stokes and anti-Stokes, however, crystallographic defects such as grains add a third peak to resolve, a QES contribution[144]. To get an understanding of what IXS and QES signal strength to expect in various geometries, this chapter outlines work on a IXS photometrics code and benchmarks it against the experiments p2191 and p2656 at the EuXFEL HED instrument[146]. Furthermore, two simulation routes are pursued to illustrate the incoherent elastic signal arising from multigranular materials, whilst, lastly, an experimental attempt at characterising such samples is presented.

First, the photometrics code will be presented, followed by phonon signal predictions for a wide range of materials highlighting promising materials for hr IXS with 7.5 keV photons for an ambient proof of principle. Second, the setups of the experiment p2191 and p2656 are

introduced and the principle of the close-to-backscattering Bragg diagnostic is outlined. This is followed by numerical predictions of the relative signal strength arising from the samples shot, who, considering the experimental error margins, are found to be in good agreement. Next, the qualitative elastic signal arising from the random summation of spherical, cubic, cylindrical, and polygon-prismatic crystallites are presented to generate artificial Debye-Scherrer patterns of spherical polycrystals that illustrate the decay of Bragg peaks, a method commonly utilised in Small-Angle X-ray Scattering (SAXS) experiments[199–201, 122, 193]. Similarly, based on MD simulations, the spherically averaged elastic signal is calculated between the Cu $\{1,1,1\}$ and $\{2,0,0\}$ Bragg peaks upon shock compression in [001] as a first demonstration of the potential of the employed Fourier methods to model the signal of dynamic experiments. This is concluded with presenting Debye-Scherrer diffraction from Cu and rolled or electrodeposited Ni targets of p2656, which are exhibiting granular structures in the $\{1,1,1\}$ and $\{2,0,0\}$ rings. It is found that whilst for sufficiently poly-crystalline materials as numerically shown in this chapter, the QES at the same scattering angle yet rotated about the Debye-Scherrer ring axis is comparable, the number of illuminated grains is too low to inform the hr IXS analysis.

4.2 Inelastic X-Ray Scattering Photometrics

Due to the monochromatisation process required to achieve the extreme energy resolution, the XFEL beam is highly attenuated and hence the hr IXS signal-to-noise ratio affected. To resolve the Stokes and anti-Stokes peaks, it is crucial to collect a high number of photons. Since the interaction is linear, in principle the signal could be increased by integrating trains in the proof of principle experiments. However, to keep measurement times reasonably short, it is essential to optimise the scattering signal; particularly in light of future dynamic experiments with drive lasers where the samples are destroyed. This section presents predictive numerical work on which material to shoot at what scattering angle Θ and experimental

results on the number of photons expected to scatter inelastically.

4.2.1 Numerical Implementation

The IXS cross section of solids is given by Equation 2.11 and depends on a range of experimental ($\mathbf{q}$, ω_0, T) and intrinsic material parameters (Z, f, L, m_a, $\omega_{\mathbf{q}0j}$, $\mathbf{G}$). The total number of photons N_{DCA} that get inelastically scattered onto a DCA analyser covering the solid angle Ω_{DCA} is

$$N_{\mathrm{DCA}} = N_0' \frac{\int \frac{\partial\sigma(q)}{\partial\Omega} \frac{d\Omega_{\mathrm{DCA}}}{4\pi}}{A_{spot}}$$

where N_0' is the number of photons interacting with the sample and A_{spot} the EuXFEL spot size. It is found from N_0, the number of photons incident on the sample after monochromatisation as

$$N_0' = N_0 \cdot \frac{z_{abs}}{z} \cdot \frac{e^{\frac{-z/z_{abs}}{\cos\Theta}} - e^{-z/z_{abs}}}{1 - \frac{1}{\cos\Theta}}, \tag{4.1}$$

where z is the sample thickness, z_{abs} denotes the absorption length of the material, and sample-internal absorption of scattered photons is accounted for. Note that the QES contribution in Equation 2.6 from $S_E(\mathbf{q},\omega)$ will not be featured here but treated qualitatively in Section 4.4.

To evaluate the cross section, several steps are taken:

- Given the XFEL photon energy of 7.5 keV and its energy change upon scattering being on the order of meV, the fraction k'/k in equation 2.5 is set to unity.
- The polarisation factor $|\epsilon_\alpha^* \cdot \epsilon_\beta|^2$ can be rewritten as $1 - \cos\Phi^2 \sin\Theta^2$.
- Confining scattering to within the first Brillouin zone (reasonable experimental angles), only longitudinal modes will be considered. Hence, when integrating over energy, the

factor in the second line of Equation 2.11 reduces to $2\langle n(Q)\rangle + 1$.

- The atomic form factor is implemented as described by Brown[202] and numerically computed in accordance with Resel and Hadley[203].
- The Debye-Waller factor is approximated in accordance with Als-Nielsen & McMorrow[158], Section 5.4.

Thus, the cross section over solid angle can be calculated from

$$\frac{d\sigma}{d\Omega}(Q) = r_e^2 \left(1 - \cos^2\Phi \, \sin^2\Theta\right) \frac{\hbar Q^2}{2 m_a \omega_Q} N_s \times Z^2 f^2(Q) e^{-2W(Q)} \left(2\langle n(Q)\rangle + 1\right),$$

where $N_s = \frac{\rho_m}{m_a} V = \frac{\rho_m}{m_a} z \, A_{spot}$ denotes the total number of scatters within the illuminated sample volume $V = L^3$ with mass density ρ_m. These scattered photons are collected by DCAs, reflected, and thereby dispersed onto a detector. Each DCA consists of approximately 2500 square, flat silicon crystals that are arranged on a spherical dome with $R = 1\,\mathrm{m}$ curvature, i.e., a focal length of $f = 50\,\mathrm{cm}$. As shown later in this chapter, these are providing ultra-high dispersion through close-to-backscattering reflection ($\Theta \approx 90°$) off the (533) planes. The cross section relevant to the EuXFEL experiments using DCAs is found as

$$\sigma = \int \frac{d\sigma(q)}{d\Omega} \frac{d\Omega_{\mathrm{DCA}}}{4\pi}$$

with Ω_{DCA} the solid angle covered by the DCA. The numerical code then integrates over each crystallite, where the total solid angle covered is approximately $\frac{Md^2}{l^2}$ with M the total number of silicon crystallites, d^2 the area of each individual crystallite, and l the distance between the sample and the DCA. The final number of photons detected by the x-ray camera

per analyser is found by

$$N = N_0' \frac{\sigma}{A_{spot}} \eta_{\mathrm{DCA}} \eta_{det},$$

with η_{DCA} the analyser and η_{det} the detector efficiency, where the former takes into account the rocking curve and angular dependence of the (533) reflection.

4.2.2 Potential Targets at p2191 and p2656

Based on this numerical code to predict the IXS signal strength for the p2191 and p2656 campaigns, the results informing their target selection are presented here. In addition to the photon count considerations, it also is essential to

- keep the thickness z of the material small and the scattering angle Θ low to avoid source broadening,
- maintain a wide peak spacing along the energy axis to ensure they can be resolved by the instrument,
- and avoid highly toxic or radioactive elements for the proof of principle runs.

Thus, for the photon energy of 7.5 keV set by the EuXFEL, numerous materials were considered and an overview of prime candidate elements is provided in Table 4.1 for 10^{10} incoming photons on the target. The scattering angles are chosen to be just halfway between [000] and the first Bragg peak for the most energetic phonon with the highest density of states. Since the signal strength is maximised when z is close to the absorption length z_{abs}, depending on the central XFEL photon energy, materials will vary in their suitability where Be, Mg, Si, and Al can be ruled out. Diamond resembles a strong scatterer with wide phonon spacing, however, given the planned polycrystalline experiments were intended to be done at room temperature, its Debye temperature of 2250 K suggests a low anti-Stokes peak[144]. To

increase the peak height, scattering would need to be collected from a less energetic phonon in closer proximity to the zone boundaries (Bragg peaks), which in turn would have the detrimental effect of an increase in the QES contribution (cf. Section 4.4).

	Z	Lattice	ρ_m [g/cm^3]	T_D [K]	z_{abs} [µm]	z [µm]	Q [Å^{-1}]	ω_q [meV]	Θ [°]	N_{DCA}
Beryllium	4	hcp	1.8	1031	4200	4100	0.9	62	13	210
Diamond	6	fcdc	3.5	2250	530	510	1.5	130	23	62
Cobalt	27	hcp	8.9	386	22	22	0.8	27	11	25
Magnesium	12	hcp	1.7	330	120	120	0.6	22	9	21
Nickel	28	fcc	8.9	345	19	18	1.5	35	23	12
Silicon	14	fcdc	2.3	692	55	54	1.0	45	15	11
Copper	29	fcc	9.0	310	18	17	1.5	30	23	9.8
Aluminium	13	fcc	2.3	390	60	58	1.4	40	20	3.9
Chromium	24	bcc	7.2	424	4.5	4.3	1.1	39	16	2.8
Iron	26	bcc	7.9	373	3.4	3.3	1.6	38	24	1.9

Table 4.1: Selected materials of interest for the EuXFEL p2191 and p2656 experiments. For $N_0 = 10^{10}$ incoming photons at 7.5 keV the total IXS photons N_{DCA} on a single DCA are shown, where diamond and Be are particularly strong scatterers.

Thus, to optimise the contrast of Stokes and anti-Stokes intensity other materials with a more closely matched Debye temperature are considered. Overall, Co, Ni, and Cu proved to be the most desirable samples due to their peak spacing, scattering intensity, and limited extent along the optical axis (as for these thicknesses, source broadening is not relevant since the instrument function is dominated by the bandwidth of the incident beam and the analyser[146]).

4.3 High-Resolution X-Ray Thomson Scattering at the HED Instrument

In the following the experimental setups for both proposal runs p2191 and p2656 are presented. The p2191 setup is designed similar to the McBride experiment at LCLS[204, 144] and introduced in detail by collaborators from the EuXFEL[146].

Both experiments use an XFEL incident on a thin target inside a vacuum chamber, giving rise to Thomson scattering. Photons are collected at a predefined scattering angle by DCAs

in a close-to-backscatter Rowland geometry of ultra-high dispersion and focused onto an x-ray detector. After coarse alignment of each DCA onto the ePix100 or Jungfrau detectors with the full SASE or seeded source, the beam is hr monochromated and poly-methyl-methacrylate (PMMA) is shot. Its amorphous structure gives rise to a strong omnidirectional elastic Thomson signal and, due to its low sound speed, only low energy inelastic modes. It is used to fine tune the DCA tilting and positions of detector, DCA, and sample on the Rowland circle. In p2656, a Laue diffraction and an XRTS detector were added for additional information on the sample structure and XFEL energy. Then, metal targets are illuminated and over the course of several hours, detector readouts for each train at 10 Hz are taken. For practical purposes, the data acquisition is split into 'runs', where each run lasts between a few seconds up to several tens of minutes. This is to keep the generated data files of the accumulated data (10 detector images per diagnostic per second) on the EuXFEL cluster at a manageable size. Runs of the same experimental configuration then will then be merged in the ensuing post-processing steps.

4.3.1 Setup of p2191

A schematic of the experimental geometry in p2191 is shown in Figure 4.1. From the left through a vacuum system connected to the EuXFEL accelerator system, the x-ray beam enters the HED interaction chamber 1, partially scatters and partially propagates through the targets at the very chamber centre, and then gets absorbed in a beam dump. The XFEL gives rise to XRTS, in particular Laue diffraction and scattering off phonons, the latter which is collected by three DCAs of 10 cm diameter and energetically dispersed onto an ePix100-detector[205] next to the sample.

The target holder is mounted on a 2D-translational mount and contains PMMA of 50 µm thickness, a thin yttrium-aluminium-garnet (YAG) to aid alignment through x-ray fluorescence, and the target foils of 12.5 µm Co, 25 µm electrodeposited Ni, and 25 µm rolled Ni.

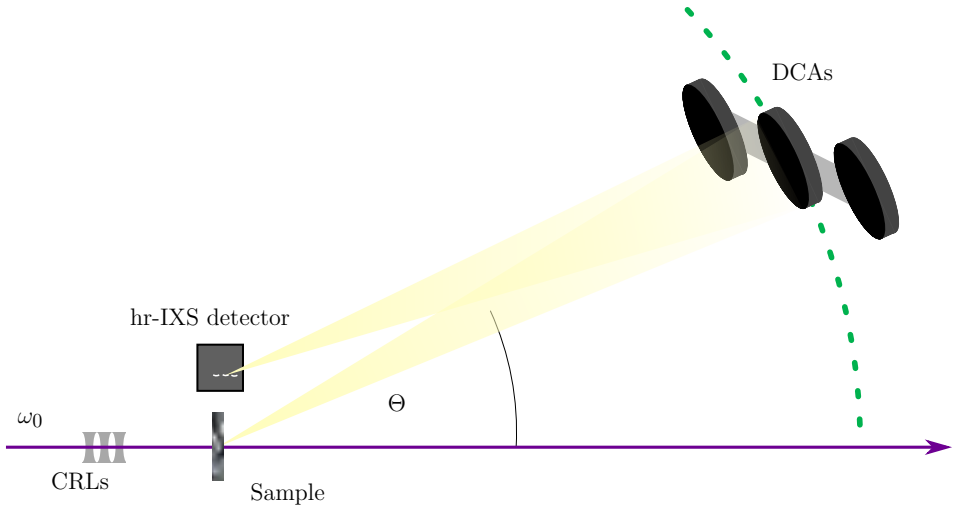

Figure 4.1: Schematic of the experimental setup of the HED p2191 experiment at the Eu-XFEL (not to scale), where the (monochromated) x-ray beam of central energy $\hbar\omega_0$, incident from the left, is collimated by compound-refractive Be lenses (CRLs), and interacts with the sample. Scattered photons are collected by three DCAs and detected by an ePix100-detector (yellow, only shown for central DCA). The DCAs are mounted on rails with a respective horizontal distance of 10 cm and can move along curved rails with a radius of 1 m (green dashed trajectory) to adjust the scattering angle Θ. The whole experiment is located within an interconnected system of vacuum chambers.

The DCAs are mapping reflected photons onto the detector, the latter which is put as close as possible to the target position, and forms with the sample and DCAs a Rowland circle of approximately 1 m diameter. All DCAs shown in Figure 4.1 are mounted on a single translation stage that allows for the scattering angle Θ to be varied. Their straight, horizontal mounting results in slightly higher scattering angles for the outer DCAs (referred to as DCA 0 and DCA 2) relative to the central one (DCA 1): for the two configurations of 12° and 21° for the central analyser (optimal for a temperature measurement of materials under investigation, cf. Section 4.2), the outer ones are at 15° and 23°. The DCA reflection efficiency is about 10% for the approximately 7.5 keV XFEL photons, covering a total bandwidth of about 460 meV.

The change of energy as a function of position on detector is found through the Bragg equation as shown in Figure 4.2. For small angles, the energy difference ΔE between two

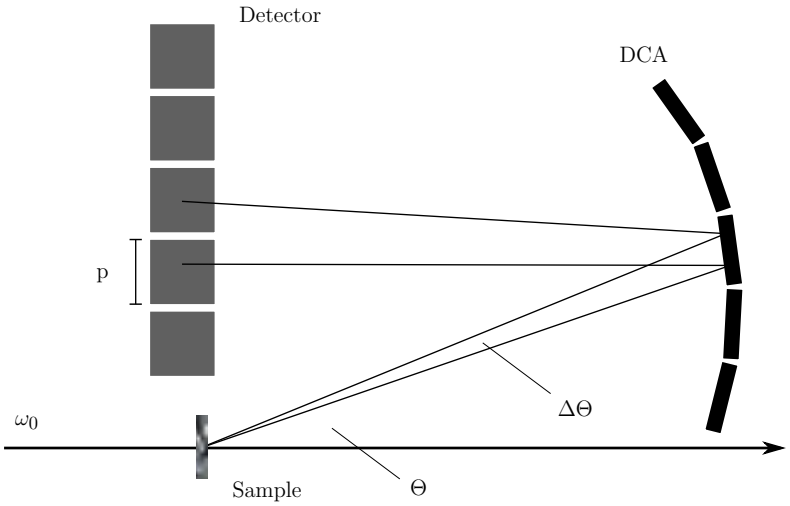

Figure 4.2: Sketch to illustrate the dispersion per pixel in the p2191 and p2656 campaigns, where the XFEL beam impinges on a sample and scatters onto the DCAs, being reflected and dispersed onto a detector with pixels of width p (not to scale). For two XFEL photons that were sent one pixel apart, one followed a scatter angle of Θ and the other $\Theta + \Delta\Theta$. By means of geometry and the Bragg equation, their energy difference will be ΔE as described by Equation 4.3.

photons hitting one pixel apart (pixel-size p) can be geometrically related to a variation in Bragg angle of $\Delta\Theta$ by taking the fraction of the derivative of the Bragg equation to itself,

$$\frac{\Delta\lambda}{\lambda} = \frac{\Delta\Theta}{\tan\Theta},$$

and using the identity $\Delta\lambda = -\frac{\Delta E\lambda^2}{hc}$ to obtain

$$\Delta E = -\frac{\Delta\lambda hc}{\lambda^2} = -\frac{\Delta\Theta E}{\tan\Theta}. \tag{4.2}$$

From Figure 4.2 one can find the geometric expression of $\Delta\Theta = \arctan\left(\frac{p}{2l}\right)$ with the diameter of the Rowland circle $l = 1m$. Substituting this, and the rearranged Bragg equation solved for Θ, into Equation 4.2, one obtains the analytical expression for the pixel dispersion

$$\Delta E = \frac{-pE}{2l\tan\left(\arcsin\frac{hc}{2dE}\right)}, \tag{4.3}$$

where d denotes the Si lattice spacing of the DCA (533) reflection.

The EuXFEL can provide a wide range of x-rays to the HED instrument as described in Section 2.3.1, where at p2191, single pulses of photon energy of 7,492 eV at 10 Hz were delivered. The SASE pulses had a resulting typical pulse energy of 600 µJ with a bandwidth on the order of 20 eV. To align the three DCAs with the PMMA, the entire SASE spectrum was used, which resulted in three fully illuminated squares on the detector. For the hr IXS measurements, the EuXFEL bunches were heavily monochromated by Si(111)- and Si(533) monochromator pairs (at room temperature) to a bandwidth of about 50 meV and defocussed by CRLs to an approximately 25 µm spot onto a metal foil sample.

At this, the temporally chaotically-varying SASE structure of the pulses within the bunches is not of importance as for the linear process of Thomson scattering, only the total photon count is relevant. However, since throughout the experiments the foils are not scanned but static, and shots on the same spot are accumulated, care has to be taken as to whether the metal samples remain unchanged by the x-rays. Whilst for the 50 fs XFEL pulses potential intra-pulse lattice dynamics (typically on the order of ps) can be ruled out, single shot melting and heat accumulation with temperatures reaching beyond the melting point could affect the target microstructure within the XFEL spot.

The average temperature change ΔT from absorbing the fraction η within a small volume V that contains N atoms can be approximated given by

$$3Nk_{\mathrm{B}}\Delta T = \eta E,$$

where $N = V \cdot \rho / m_A$ with the mass density ρ and average atomic mass m_A of the absorbing material. The optimal thickness of the metal targets is about one absorption length, which results in $\eta \approx 0.4$. After the hr monochromators, the highest pulse energy estimate provided by the EuXFEL is about $E_p = 20\,\mu\mathrm{J}$, and the spot size 25 µm in diameter. This rough estimate results in an average temperature increase of 200 K for nickel, a change which,

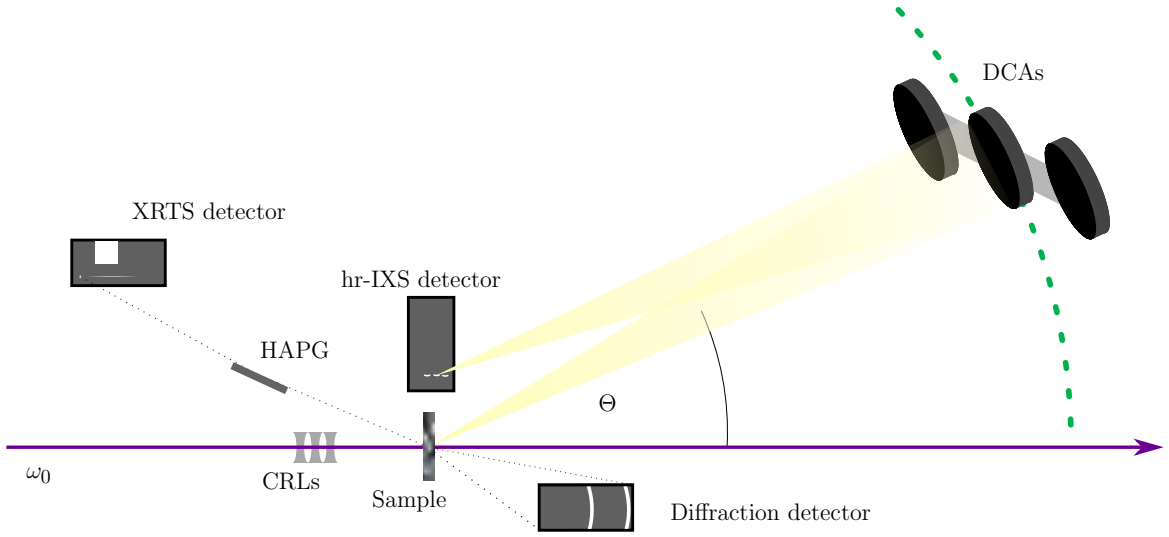

Figure 4.3: Schematic of the experimental setup of the HED p2656 experiment at the Eu-XFEL (not to scale). The hr IXS setup is identical to p2191, whilst a backward XRTS spectrometer and a forward diffraction detector have been added in this campaign.

starting from room temperature, is far below its melting point of 1728 K. Furthermore, at single pulse operation at a repetition rate of 10 Hz, the temporal spacing of the XFEL pulses is 100 µs. Given that the thermal diffusion coefficient of the metals targets is on the order of $100\frac{\text{mm}^2}{\text{s}}$, an approximate diffusion length of 3 mm indicates that once the next pulse arrives, no residual heat remains within the micron-sized XFEL spot.

4.3.2 Setup of p2656

A schematic of the experimental geometry in p2656 is shown in Figure 4.3, where a top and side view of the expanded experiment in the HED interaction chamber 2 can be seen. Similar to p2191, the XFEL beam of 7,501 eV, defocussed to about 25 µm, gives rise to IXS in a Rowland geometry that consists of thin targets, the DCAs, and a Jungfrau detector[206]. In addition, a Laue diffraction detector (further details and results in Section 4.5) and a Highly Annealed Pyrolytic Graphite (HAPG) von Hámos spectrometer are added.

The scattering angle Θ for the outer DCAs (DCA 0 and DCA 2) is 23° and for the central one (DCA 1) 21°. The Laue setup using a Jungfrau detector covers the forward scattering

angle range from 35° to 58° that contains a 12° radial section of the {111} and {200} Debye-Scherrer rings of Cu and Ni. The HAPG spectrometer as backscatter diagnostic at $\Theta \approx 170°$ collected XRTS photons, focussing and dispersing them onto a Jungfrau detector, where an energy range from 6680 to 7542 eV is covered.

Again, the targets are mounted on a 2D-stage perpendicular to the x-ray optical axis and feature poly-methyl-methacrylate of 50 µm (PMMA) thickness, a thin YAG, a foil of 17.5 µm Cu, and the same Ni targets as shot in p2191: 25 µm electrodeposited Ni, and 25 µm of rolled Ni.

Since the commissioning experiment p2191, the EuXFEL was further developed and in p2656, for the first time, a seeded beam of two pulses per train (444 ns intra-train peak separation) and about 175 µJ was used for hr IXS. The bandwidth provided to the HED instrument was on the order 1.2 eV prior to hr monochromatisation, whilst pulse energy fluctuations were 100%, resulting in some pulses to be twice as intense as the average, or entirely non-existent. In principle, there can be significant heat retention between the first and second intra-train pulses if their temporal spacing is too narrow (for a 444 ns gap, the diffusion length is on the order of 7 µm), however, it was found that upon monochromatisation, transmitting the first pulse reduced the transmission of the second one to below the noise floor of the photodiodes monitoring the XFEL intensity. This is attributed to the thermal expansion of the monochromators, which then changes the backscattering angle and causes the second pulse to experiences increased partial absorption and to be misdirected, hence not reaching the experimental chamber anymore. In principle, for a intra-train pulse pattern with sufficient time for the metals to cool down again (e.g., having a time spacing of $5 \cdot 444$ ns) in order to avoid the build-up of heat, the signal strength would highly benefit from the extra photons, however, even for two pulses with the maximum intra-train spacing ($49 \cdot 444$ ns), the monochromatisation setup would not transmit more than the first existing pulse. Still, the experiment was run with two such bunches at maximum intra-

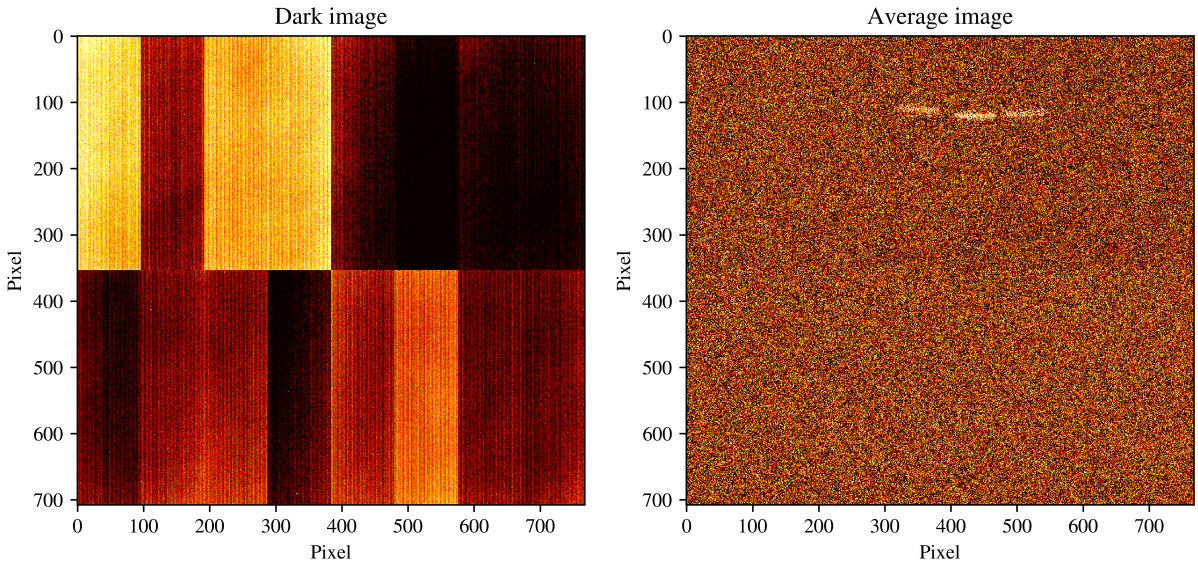

Figure 4.4: Representative median/dark image (left) and mean signal (right) of p2191. This run on PMMA at 21° contained 1099 trains. In the median image, the four square ePix100-sub-arrays can be seen, together with an even finer substructure resulting from the readout process. For the strong signal of PMMA, in the mean image photons from the three DCAs can just about be distinguished by eye within the noise.

train separation, since given the fluctuations, using two pulses still enhanced the total flux: if the first pulse happened to not be delivered, the second pulse encounters an unchanged monochromator and is transmitted.

4.3.3 Raw Data Processing of p2191

The ePix100 detector consists of 768 x 702 square pixels of 50 µm edge length and its readout is synchronised with the XFEL beam, resulting in stacks of 768 x 702 x N_{trains} with N_{trains} the number of trains per run. A single photon of 7.5 keV creates a signal of about 120 analogue-to-digital-unit (ADU), which however is much lower than dark currents of the detector. That is why raw images need to be corrected for their background (reference to signal zero) and for malfunctioning pixels. Given the photon signal throughout the hr IXS experiments is extremely low (about one photon per train), the data shots can be treated as dark images (detector signal without XFEL beam). The pixel-wise median, as shown

in Figure 4.4, is subtracted from each raw image as background correction. Furthermore, the standard deviation of each pixel is computed, and any signal from pixels that have an extremely low (dead/cold pixel) or strongly varying standard deviation (hot pixels) are set to zero. In Figure 4.4 also the mean image for all PMMA runs at 21° is shown, where three regions of interest – the foci of the DCAs – can be seen. However, the signal is embedded in a significant noise floor and is hardly discernible for the average photons per shot on metals. Whilst the development of these cutting edge detectors is very challenging and in this work they will be covered only in a limited depth of detail, it is important to note that an x-ray photon can excite multiple pixels at once, spreading their generated charge across several pixels, causing neighbouring signals below 120 ADU that will sum to the full signal. Similarly, the read out process can occasionally spread the generated charge and thereby cause artificial multipixels. These effects can be seen in Figure 4.5, where the histogram of the corrected image stack is plotted. The peak around 0 ADU is the noise floor (most pixels are not hit by an x-ray), whilst single photon hits can be found around 120 ADU. There also are a few multi-photon hits above 130 ADU, and multipixel hits below 110 ADU. Such multipixel hits and the significant noise floor in the mean images is why a SPC routine will be employed, as described in Section 2.4.2.

The sum of all SPC images for all PMMA runs at 21° in equivalent experimental configuration is shown in Figure 4.5, where the three regions of interest (ROIs) corresponding to each DCA can be distinguished. In Section 4.3.5, the average photon count per such region will be compared with the numerical predictions based on the code presented in Section 4.2.

4.3.4 Raw Data Processing of p2656

The experiment p2656 was conducted more than two years later than p2191, by which time development of XFEL seeding had progressed. These improvements, together with more experimental time to integrate the signal, encouraged p2656. As shown above, the hr IXS

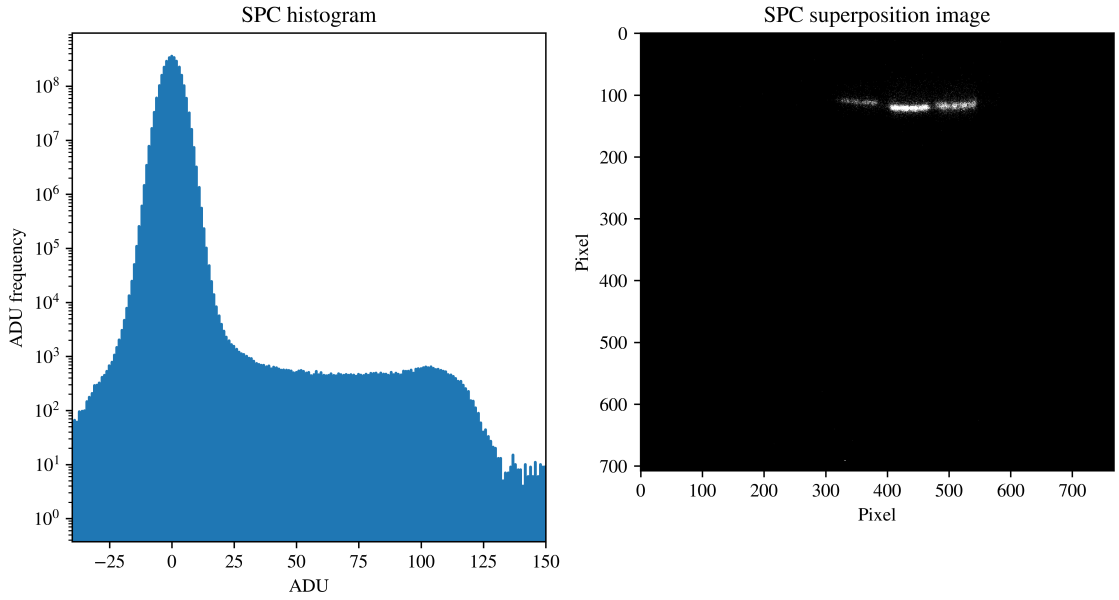

Figure 4.5: Histogram of the corrected stack of all images of PMMA at 21° with 5242 trains and 14987 photons in total. The noise floor is around 0 ADU, single photon hits are around 120 ADU, a few multi-photon hits are above 130 ADU, and multipixel hits are below 110 ADU. Corresponding single photon image. Apart from a few outliers (noise), the focal spots of the three DCAs can be seen.

setup is almost identical, yet instead of an ePix100, a Jungfrau hr IXS detector is used, in addition to an added HAPG and diffraction detector.

The Jungfrau detector consists of 1024 x 512 square pixels of 75 µm edge length, again resulting in stacks of 1024 x 512 x N_{trains}. Due to the detector featuring three gain stages (signal amplification depending on how many photons are incident), the background correction is more involved[206] and an automated routine implemented at the HED instrument, where essentially three dark images at each gain stage are applied. With this calibration, a single photon of 7.5 keV creates a signal of 7.5. Afterwards, the same hot/cold pixel corrections and SPC routine as for the ePix100 are applied. The SPC images are then added for runs of equivalent experimental configuration.

4.3.5 Relative Photon Numbers at p2191 and p2656

In the following, the hr IXS photon numbers are shown and compared with the code predictions in Section 4.2. Due to commercial availability, the actual thickness of the Co, Ni, and Cu targets shot during the experiments were 12.5 µm, 25 µm, and 17.5 µm respectively, whilst the number of incident photons after monochromatisation of either SASE or seeded beam was on the order $N_0 = 10^9$. The average photon numbers per train of all runs are obtained through SPC and shown in Table 4.2.

Experiment	Sample	Θ [°]	N_{det}
p2191	Co	12°	0.08
	Ni(r)	12°	0.09
	Ni(r)	21°	0.07
	Ni(e)	21°	0.14
p2656	Ni(r)	21°	3.8
	Ni(e)	21°	3.6
	Cu	21°	5.2

Table 4.2: Average photon numbers per train for three DCAs at p2191 and p2656 for the Co, Ni (rolled), Ni (electrodeposited), and Cu targets. Due to XFEL intensity fluctuations, care needs to be taken when comparing the scattering signal of different runs and elements.

In principle, based on these experimental numbers, the code could be calibrated by replacing the undetermined efficiencies η_{det} (close to 100%), η_{DCA} (on the order of 10%, yet alignment-dependent), and N_0. Whilst there is some uncertainty arising from the analysis, e.g., mutlipixel hits that contain contributions split up below 25 ADUs that are filtered out, the photons per train for two different runs on the same material exhibit significant variations. This is shown in Figure 4.6 of p2656 run 244, where the counted photons per train fluctuate in time. This is attributed to intensity fluctuations of the XFEL, which were found to arise from pointing jitter through the HED x-ray optics, i.e., the mirrors and monochromators. The beam fluctuations consist of non-deterministic jumps plus a multi-minute-timescale decay and thus imply only a short time correlation.

Hence, the only inter-material correlation is between adjacent trains of subsequent runs

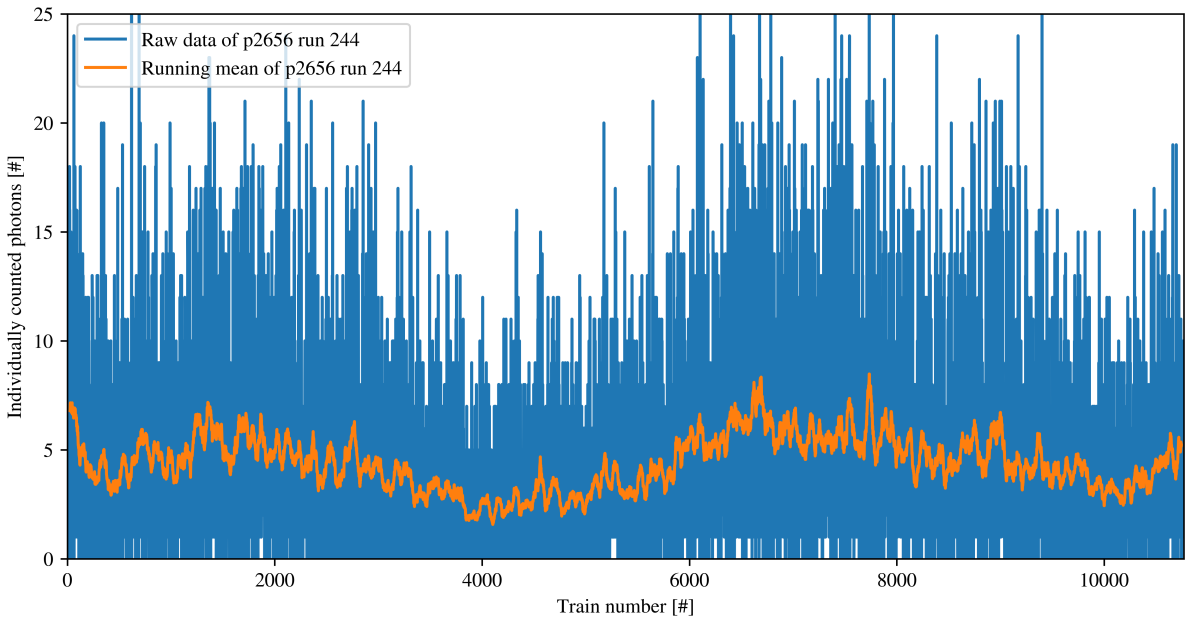

Figure 4.6: Number of photons obtained via SPC as a function of train. The XFEL operated at 10 Hz, implying that this run lasted 18 minutes. Whilst fundamentally the number of photons per train will vary due to shot noise, long term drifts on the order of several minutes can be observed due to variations in the XFEL intensity.

to ensure a comparable XFEL intensity. This could be done in p2191 for runs 451 and 452 for Ni(r) and Co at 12°, and in p2656 for runs 234 and 234+235 of Cu and Ni(e) at 21°, as shown in Figure 4.7. The intensity fractions Cu/Ni(e) and Co/Ni(r) (for the last and first 100 trains) are 1.27 and 1.13 respectively. Note that the overall signal-to-noise ratio is much lower for p2191.

The respective numerical predictions yield $\mathrm{Cu/Ni} = 0.97 \pm 0.05$ and $\mathrm{Co/Ni} = 1.14 \pm 0.07$. The theoretical errors refer to the effect of potential thickness fluctuations of the foils that are quoted by the manufacturer as ±15%. Provided the potential QES contribution to the counted single photons for any of the samples did not demand a significant signal reduction, within the significant beam fluctuations the relative IXS strength predicted matches the experimental observations.

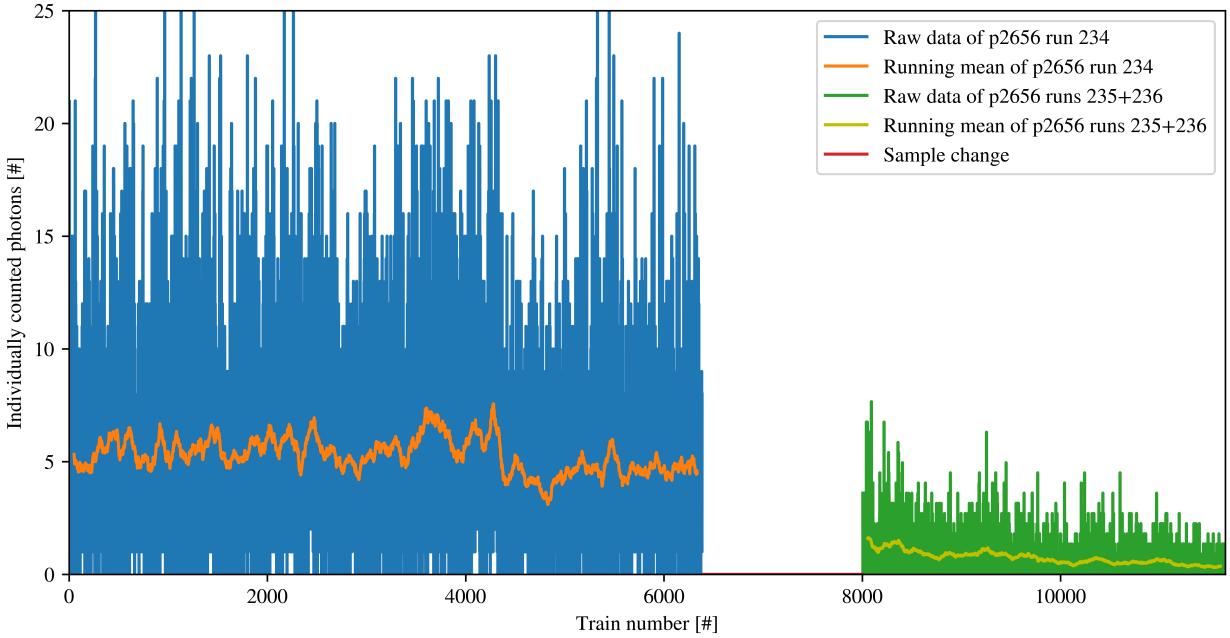

(a) Signal of p2656 Cu followed by Ni(e)

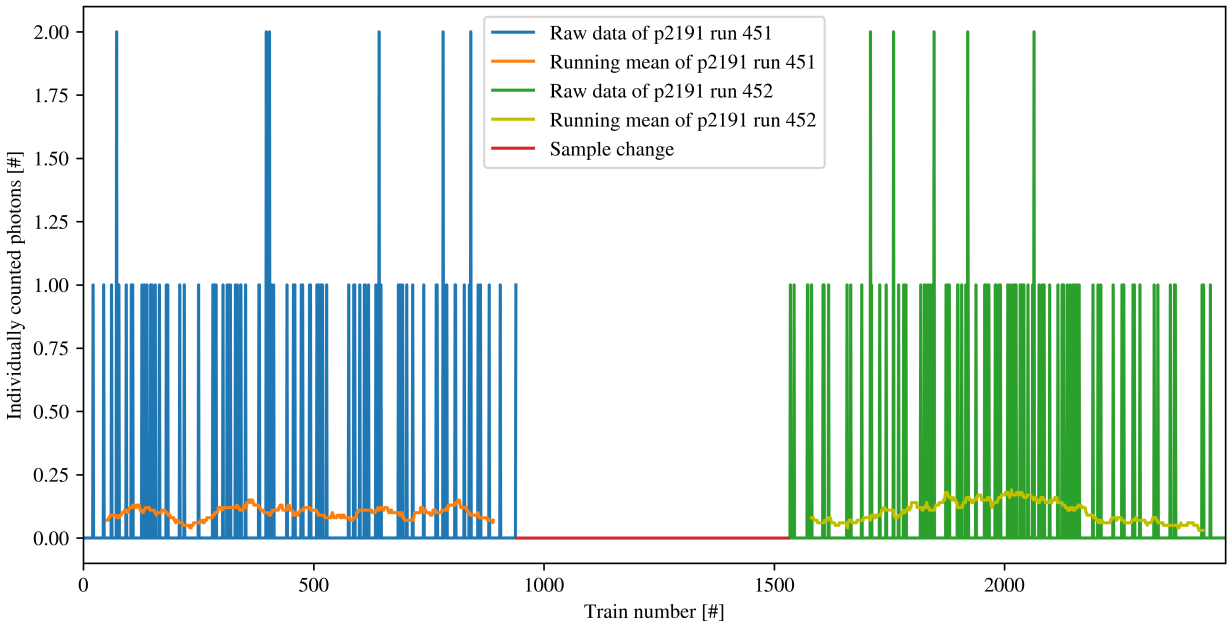

(b) Signal of p2191 Ni(r) followed by Co

Figure 4.7: Number of photons obtained via SPC as a function of train for adjacent runs of p2191 (top) and p2656 (bottom). The XFEL operated at 10 Hz. Again, a long term drift can be observed due to variations in the XFEL intensity, which complicates the direct comparison of signal strength.

4.4 Qualitative Modelling of Quasi-Elastic X-Ray Scattering

In addition to predicting the IXS part of the signal, it is crucial to understand the origin of the QES contribution. Its nature is less deterministic since often the grain structure of the material under investigation is not (well) characterised. However, this section aims at providing some qualitative models to aid intuition when designing or analysing experiments with the goal of using hr IXS to measure temperature. First, analytical diffraction patterns for several crystallite shapes will be presented to cover a few fundamental building blocks of QES, followed by a synthetic Debye-Scherrer pattern for spherical diamond crystallites. Then, spherically averaged diffraction from a mock defected polycrystal will be presented.

4.4.1 Shape-Function Diffraction

As shown in Equation 2.10, the diffraction signal of a single crystallite is proportional to the Fourier transform of its shape function that replaces each sharp Bragg peak. It follows that for a spherical crystallite of radius R, described by a shape function

$$g_S(\mathbf{r}) = \begin{cases} 1 & \text{if } |\mathbf{r}| \leq R \\ 0 & \text{else} \end{cases},$$

the diffraction pattern behaves as

$$I_E \propto \left| \sum_{\mathbf{G}} R^3 \frac{\sin(x) - x\cos(x)}{x^3} \right|^2, \tag{4.4}$$

where $x = R\,|\Delta\mathbf{k} - \mathbf{G}|$. Similarly, a cuboid of dimensions L_x, L_y and L_z is described by

$$g_S(\mathbf{r}) = \begin{cases} 1 & \text{if } x \in [-L_x, L_x] \wedge y \in \left[-L_y, L_y\right] \wedge z \in [-L_z, L_z] \\ 0 & \text{else} \end{cases}$$

and thus

$$I_E \propto \left| \sum_{\mathbf{G}} \prod_{j \in \{x,y,z\}} L_j \, \mathrm{sinc}\left(\frac{L_j \left(\Delta k_j - G_j \right)}{2} \right) \right|^2 ,$$

where $\Delta \mathbf{k}_j$ denotes the j-component of the photon momentum change vector in an orthonormal coordinate system. A cylinder of height h aligned with the z-axis and radius R is described by

$$g_S(\mathbf{r}) = \begin{cases} 1 & \text{if } x^2 + y^2 \leq R \wedge z \in [-h/2, h/2] \\ 0 & \text{else} \end{cases}$$

and behaves as

$$I_E \propto \left| \sum_{\mathbf{G}} R^2 \frac{J_1\left(R\sqrt{\Delta k_x^2 + \Delta k_y^2} \right)}{R\sqrt{\Delta k_x^2 + \Delta k_y^2}} h \, \mathrm{sinc}\left(\frac{\Delta k_z h}{2} \right) \right|^2 ,$$

with J_1 the Bessel function of the first kind. Finally, the Fourier transform of a general flat polygon is described by Chu & Huang in [207, 208], which aids the description of the signal arising from a hexagonal prism. Thus, in analogy to the cylindrical case, $\widetilde{g}_S$ is the product of this transformed polygon with a sinc-function in the direction of the prism axis.

These considerations provide an expression for elastically scattered intensity into the direction defined by $\Delta \mathbf{k}$. Based on a chosen shape function, a numerical code creates a diffraction pattern, covering up to 4π. For this overview, the much weaker contribution from $S_I(\mathbf{q}, \omega)$ is disregarded.

For a diamond lattice with [001] aligned with the z-axis, the forward diffraction pattern for the four different shape functions presented here can be found in Figure 4.8. Bragg peaks up to $\{2, 2, 0\}$ are included. The elastic intensity is not confined to the Bragg peaks anymore, but is spread into all of 4π and the non-trivial patterns suggest sharp, distinct signatures in

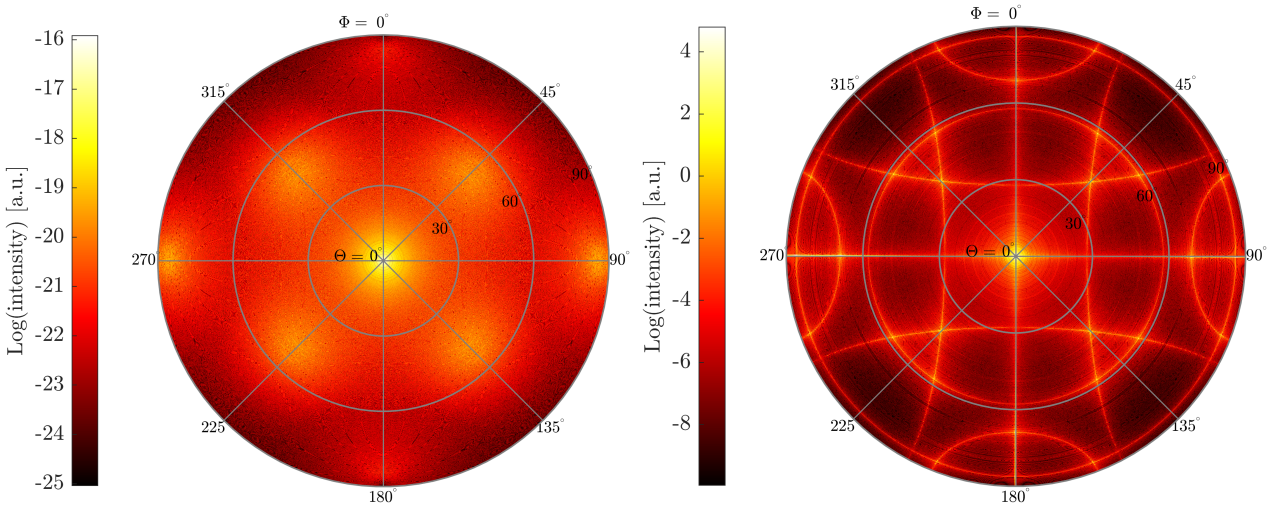

(a) Spherical shape function

(b) Cuboidal shape function

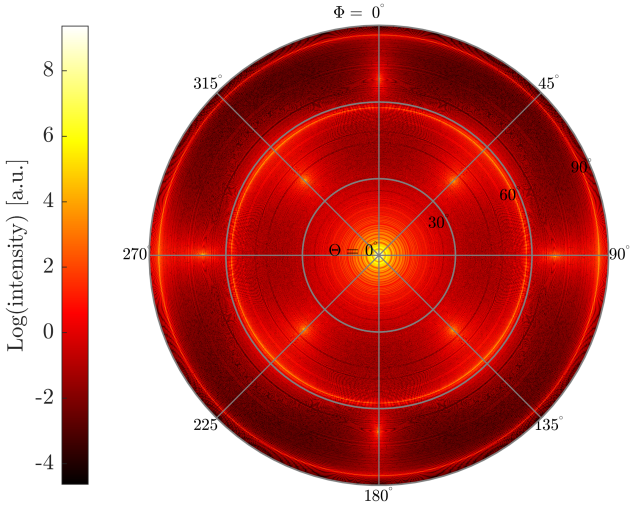

(c) Cylindrical shape function

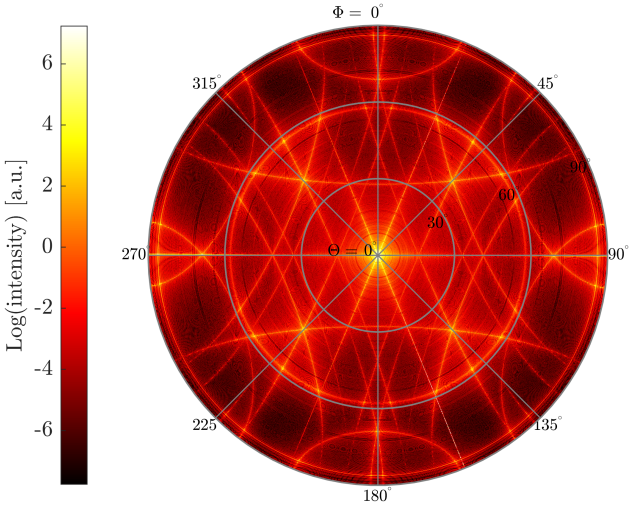

(d) Hexagonal prism shape function

Figure 4.8: Shape functions of a single diamond sphere (top left), cuboid (top right), cylinder (bottom left) and hexagonal prism (bottom right) at 7.5 keV for the Bragg peaks $(0, 0, 0)$, $\{1, 1, 1\}$, and $\{2, 2, 0\}$. Θ varies radially, Φ clockwise.

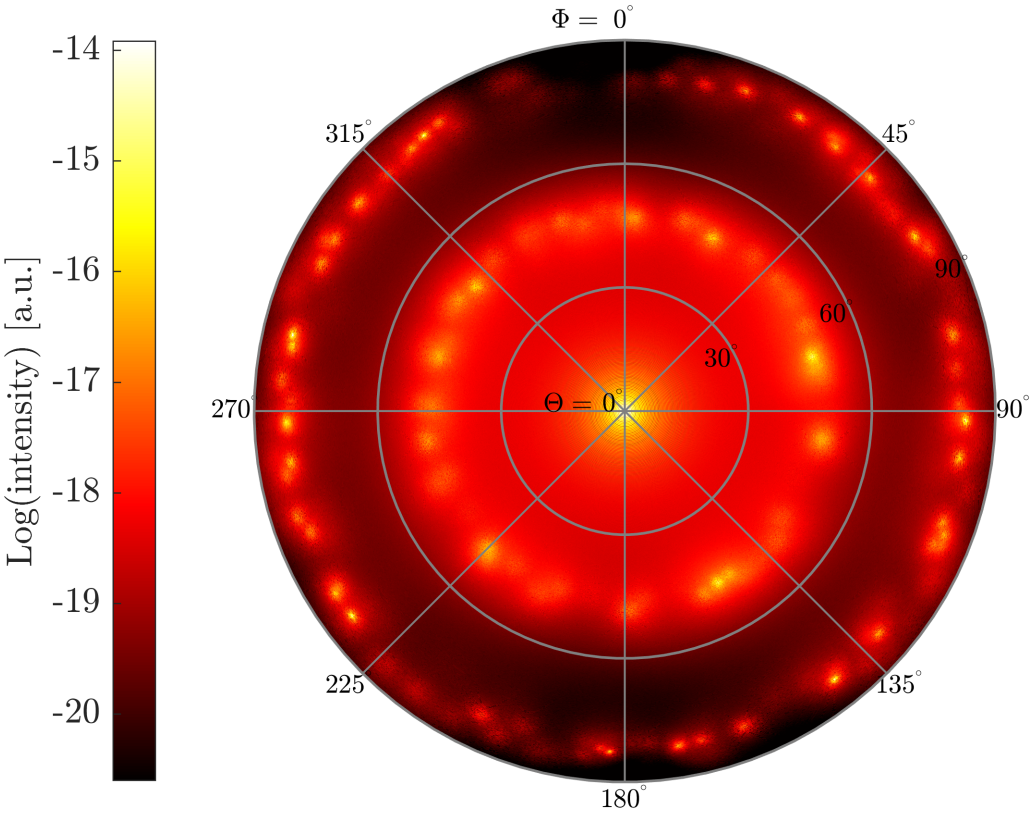

Figure 4.9: QES from 100 randomly orientated spherical diamond crystallites at 7.5 keV, where the $\{1, 1, 1\}$ and $\{2, 2, 0\}$ Debye-Scherrer rings are visible. Θ varies radially, Φ clockwise.

reciprocal space for these single crystallite cases.

To model an experimentally more common scenario, the code can randomly vary the crystallite orientation of the crystal planes, i.e., $\mathbf{G}$, relative to the shape, which allows for the generation of Debye-Scherrer-like patterns. In Figure 4.9 the QES of 100 randomly orientated spherical diamond crystallites with $R = 500$ nm at 7.5 keV is shown. The pattern is angularly weighted by the Thomson polarisation (the x-rays are horizontally polarised), Debye-Waller and atomic form factor and attenuated due to absorption within the crystal as described by Equation 4.1. The fundamental Bragg peak in addition to the $\{1, 1, 1\}$ and $\{2, 2, 0\}$ Debye-Scherrer rings are visible. The polarisation factor reduces the intensity at $\Phi = 0°$ and $180°$. Significant elastic intensity is present between these rings, as seen upon azimuthal integration in Figure 4.10.

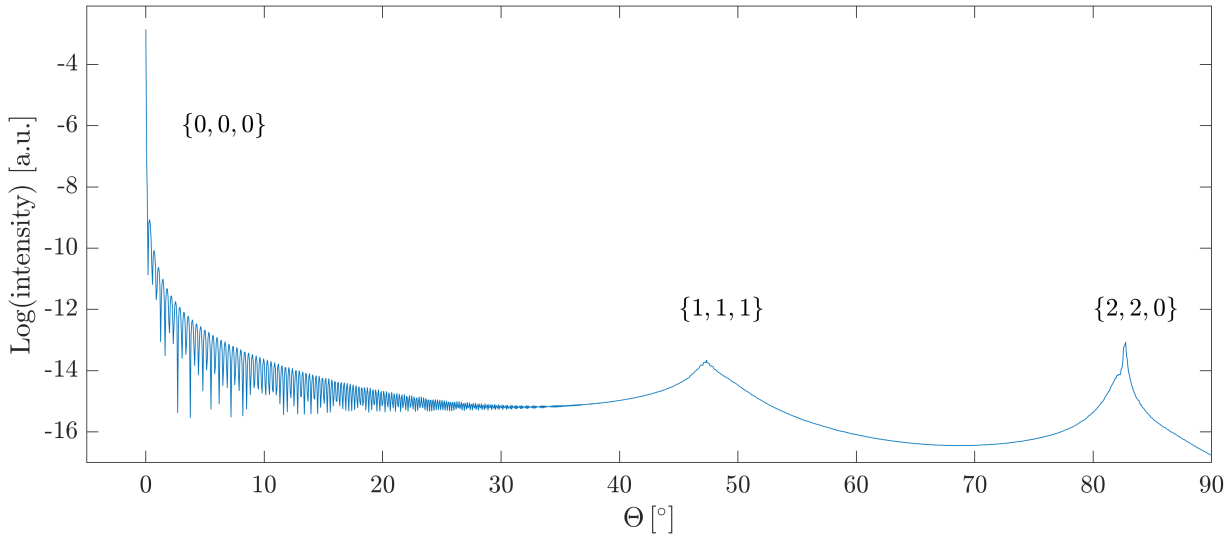

Figure 4.10: Azimuthally integrated intensity of the 100 randomly orientated diamond crystallites of Figure 4.9. The Debye-Scherrer peaks $(0,0,0)$, $\{1,1,1\}$, and $\{2,2,0\}$ together with QES intensity in between them can be seen. Close to $(0,0,0)$, the fast oscillations of the Bessel shape function are resolved, whilst around the other peaks effects of the sample granularity are visible.

This basic model aims to provide qualitative insight into how shape function alter the diffraction patterns. In the next section, polycrystalline diffraction with defects aims at providing a first step towards understanding QES in polycrystalline shocked samples.

4.4.2 Polycrystalline Diffraction through Molecular Dynamics Simulations

Thus, to get an initial understanding of the signatures in reciprocal space of shocked polycrystals containing defects such as stacking faults, the 3D-averaged Fourier transform of the dump boxes featured in Chapter 3 is calculated.

Hereby, a polycrystal is mimicked by, first, randomly selecting a direction in k-space of the [001] shocked copper crystal, second, calculating the line out between a k-range of 1.65 and 2.60 $\frac{2\pi}{a}$ (Cu lattice constant a) along that random direction (covering the $(0,0,2)$ peak for the 70 GPa compression of 77%), and, third, incoherently adding a large number of these. To avoid a directional signature from the cuboidal simulation box in the form of sinc function along the cardinal direction, a sphere fitting within the box was defined, where all

atoms outside that sphere were dropped. This ensures the isotropic Bessel shape function as described by Equation 4.4.

Due to the significant computational cost of evaluating Equation 2.7 for about 250,000 atoms, the code was parallelised with the Python package `numba` and run on a computing cluster. The resulting Debye-Scherrer patterns from these reciprocal space shells are shown in Figure 4.11. For elastic shock pressures (0 to 20 GPa), the $\{1,1,1\}$ and $\{2,0,0\}$ Debye-Scherrer rings are visible (dressed by Bessel functions), where a pressure induced shift stems from the z-component being affected by the compression. Once plasticity arises and the system moves towards the hydrostatic pressure regime, the Bragg peaks split up and QES between these peaks significantly increases. The actual positions of the Bragg peaks were found by taking the 3D Fourier transform of each dump sphere and their positions are indicated as triangles.

Note that since faulting will be different for shocks along different crystal axes, the averages presented here only are of qualitative merit. Shocks in other directions generate different defects, particularly in real crystals where the limited simulation size is not affecting the stacking fault density. Furthermore, the actual shape functions of crystallites will not be perfect spheres but a superposition of numerous shapes with defects on the grain boundaries such as gaps and strain fields. Overall, whilst this numerical method has its limits, it is clearly demonstrated that high QES arises even when averaging over multiple crystallites of isotropic orientation with a stacking fault density as found in Chapter 3.

4.5 Debye-Scherrer Diffraction at the EuXFEL

To gauge the microstructure of the targets shot in p2656, as described in Section 4.3.2, a diffraction detector was added to monitor the $\{1,1,1\}$ and $\{2,0,0\}$ Debye-Scherrer rings of Cu and Ni, and, in reference to these peaks, the QES signal between them.

The Jungfrau detector was placed close to the focal spot in forward direction, covering

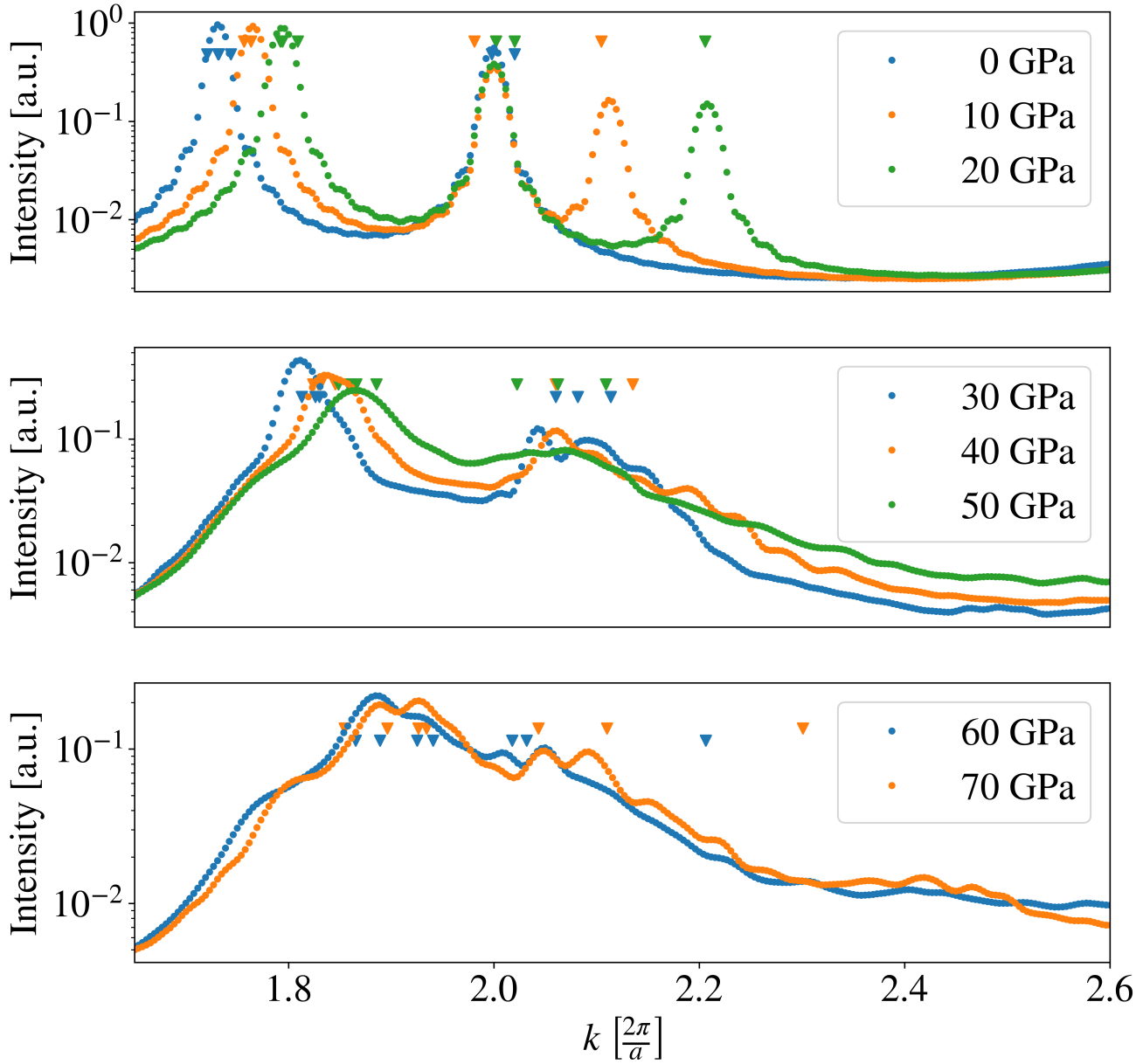

Figure 4.11: For the sphericalised dump boxes of the shock simulations in Chapter 3, the shell averages of the reciprocal space for $k \in [1.65, 2.60]$ with 248 steps are plotted in addition to an overlay of the Bragg peaks. The intensity of each line out is normalised by the number of atoms in each spherical dump box and the number of line outs (about 10^7). From 0 to 20 GPa, the Bragg peaks (dressed by the Bessel shape function) are well defined and move towards higher k due to the compression along [001]. Beyond that, they split and significant QES arises between them.

a wide angular range from 35° to 58° which includes two diffraction peaks. The EuXFEL at a central photon energy of 7.5 keV is defoussed onto the Cu, electrodeposited Ni, and rolled Nickel with a 25 µm spot. The raw images were corrected as described in Section 4.3.4 (yet, due to much higher signal, without any SPC) and damaged detector regions masked. The results can be seen in Appendix B, where for each material two vertical lines are found, sections of the anticipated the $\{1, 1, 1\}$ and $\{2, 0, 0\}$ rings. Based on these, the patterns are calibrated and unwarped with `Dioptas`[209], with the final 2D patterns shown in Figures 4.12 and 4.13 (Φ varies anti-clockwise with a rotation axis aligned with the XFEL propagation). Hereby, since the XFEL intensity fluctuates, the pattern for each batch is normalised by the number of single hr IXS photons counted within that batch. Whilst the diffraction intensities between materials vary as described by Equation 2.8, in order to compare Ni(e) and Ni(r), only the IXS contribution should be used in the normalisation process (which is influenced by, yet not as sensitive to the grain structure). Due to the lack of absolute XFEL intensity, the normalisation by counted single photons (of both IXS and QES) resembles the best possible guess. In addition to the Debye-Scherrer rings, in Figures 4.12 and 4.13, stray signal is visible. Some of it is localised, as, for example, in the first batch of Ni(e) in the region (Φ, Θ) of $(2°, 51°)$, some spread out wider as in the first batch Ni(r) in the region of $(8°, 50°)$. Furthermore, even though the sample stages were ordered to move to the same coordinates, for batches with the same targets, a slight deviation in the granularity of the Debye-Scherrer rings can be noticed, which showcases the limited spatial resolution of the stages.

The aims of these diffraction measurements are to get an understanding of the target granularity, to characterise the decay and QES between the Bragg peaks, and to extrapolate these findings to lower angles in order to inform the hr IXS temperature measurement. Hence, first, a normalised metric Γ based on the standard deviation (std) along the ring is

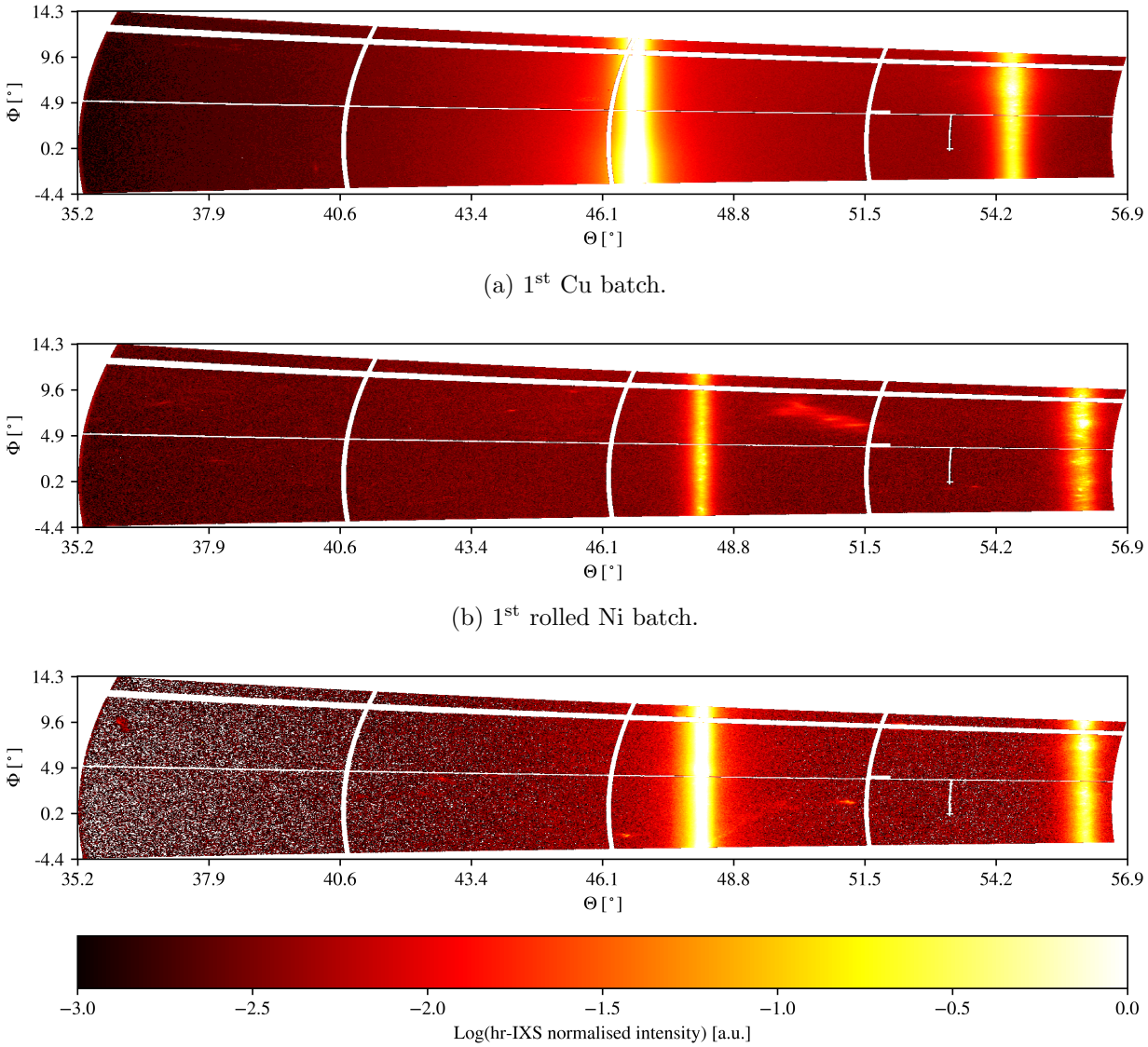

(a) 1st Cu batch.

(b) 1st rolled Ni batch.

(c) 1st electrodeposited Ni batch.

Figure 4.12: Unwarped normalised diffraction patterns for the samples shot at p2656 (1st set of experimentally equivalent positions). From left to right, the $\{1,1,1\}$ and $\{2,0,0\}$ fcc Debye-Scherrer rings can be seen. The Jungfrau also detected sample-position dependent stray signal.

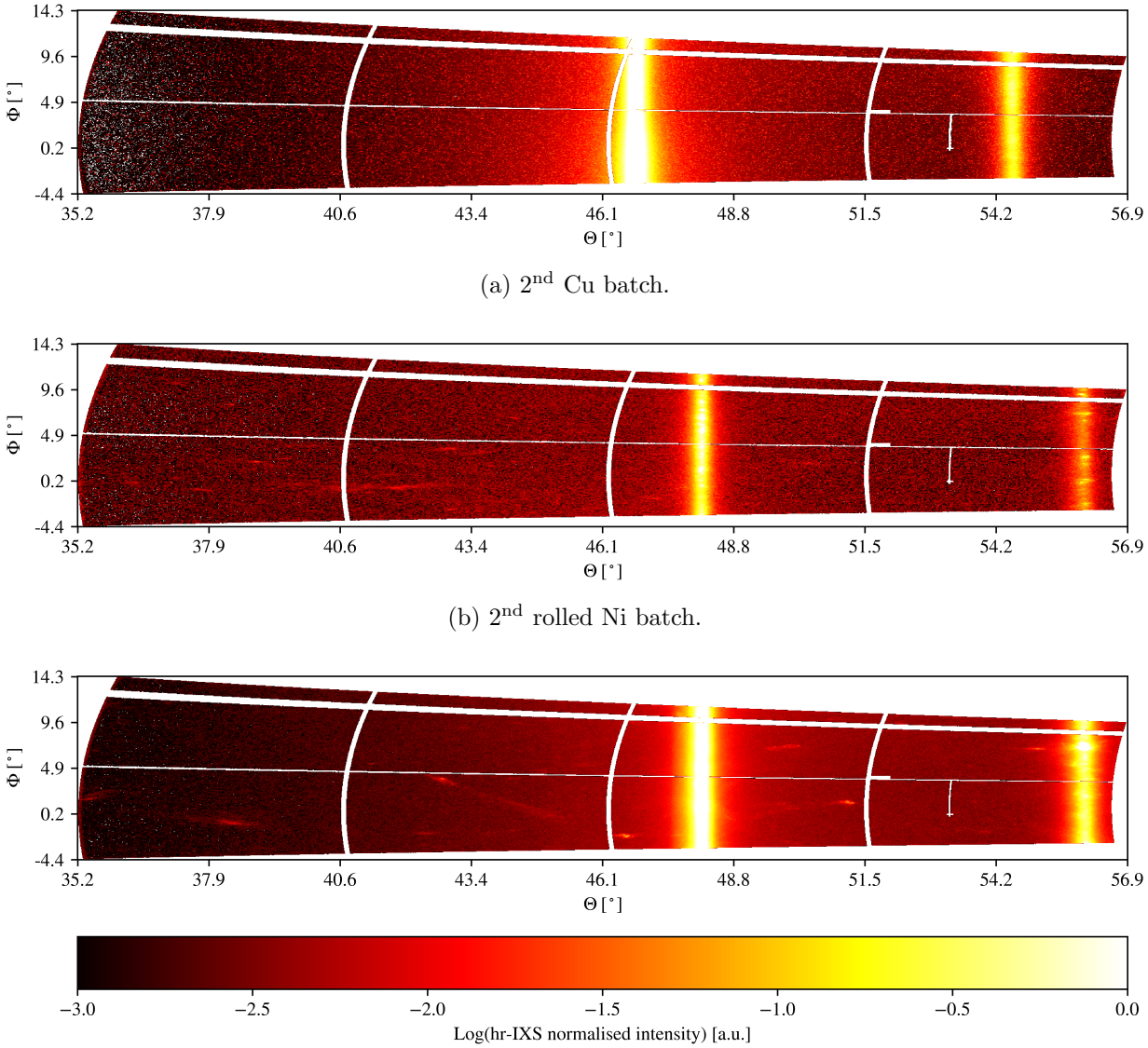

(a) 2nd Cu batch.

(b) 2nd rolled Ni batch.

(c) 2nd electrodeposited Ni batch.

Figure 4.13: Unwarped normalised diffraction patterns for the samples shot at p2656 (2nd set of experimentally equivalent positions). From left to right, the $\{1,1,1\}$ and $\{2,0,0\}$ fcc Debye-Scherrer rings can be seen. The Jungfrau also detected sample-position dependent stray signal which mostly differed to that seen in the 1st batch.

calculated through

$$\Gamma = \frac{\mathrm{std}_i \left(\sum_j L_{i,j} \right)}{\sum_{i,j} L_{i,j}}$$

where $L_{i,j}$ is the discrete line out along a ring in i-direction with a width of 11 pixels in j-direction. For a perfect polycrystal, the Debye-Scherrer rings are isotropic, no Φ dependence is expected, and Γ vanishes. The results are shown in Table 4.3.

Sample	Batch	$\Gamma_{\{1,1,1\}}$ [a.u.]	$\Gamma_{\{2,0,0\}}$ [a.u.]	$\sigma_{\{1,1,1\}}$ [°]	$\sigma\{2,0,0\}$ [°]
Cu	1st	$2.2{\cdot}10^{-3}$	$2.1{\cdot}10^{-3}$	0.13	0.24
	2nd	$2.1{\cdot}10^{-3}$	$1.0{\cdot}10^{-3}$	0.13	0.25
Ni(r)	1st	$1.4{\cdot}10^{-3}$	$10.3{\cdot}10^{-3}$	0.18	0.15
	2nd	$2.0{\cdot}10^{-3}$	$2.9{\cdot}10^{-3}$	0.14	0.25
Ni(e)	1st	$7.2{\cdot}10^{-3}$	$9.3{\cdot}10^{-3}$	0.08	0.12
	2nd	$2.1{\cdot}10^{-3}$	$12.1{\cdot}10^{-3}$	0.10	0.11

Table 4.3: Normalised metric Γ taken along the Debye-Scherrer ring sections. The higher the value, the higher the granularity. On average, the Ni(e) samples exhibit the highest Γ. Furthermore, the FWHM of the rings is listed.

Second, the spectra are projected along Φ, shown in Figure 4.14, and their peak widths extracted to assess the average Bragg peak decay per batch. To do so, each peak is fitted with a local Voigt profile as shown in Figure 4.15 and the resulting FWHM $\sigma_{\{1,1,1\}}$ and $\sigma_{\{2,0,0\}}$ are listed in Table 4.3.

In general, whilst some Debye-Scherrer rings are visibly inhomogeneous and some peaks even exhibit some asymmetry, a slight change in the Ni(r) sample position caused a significantly altered diffraction signal, where the $\{1,1,1\}$ and $\{2,0,0\}$ peaks swap in being the most intense signal. Furthermore, the average Γ per target varies, where Cu appears to be the most constant along the ring, and Ni(e) the most variable. Upon examination of the two Ni samples in Figure 4.14, one can find that the overall decay of Ni(r) does not match the slope of Ni(e) (nor Cu).

As a rule of thumb, wider peaks suggest smaller grains (cf. Section 4.4) and thus a more

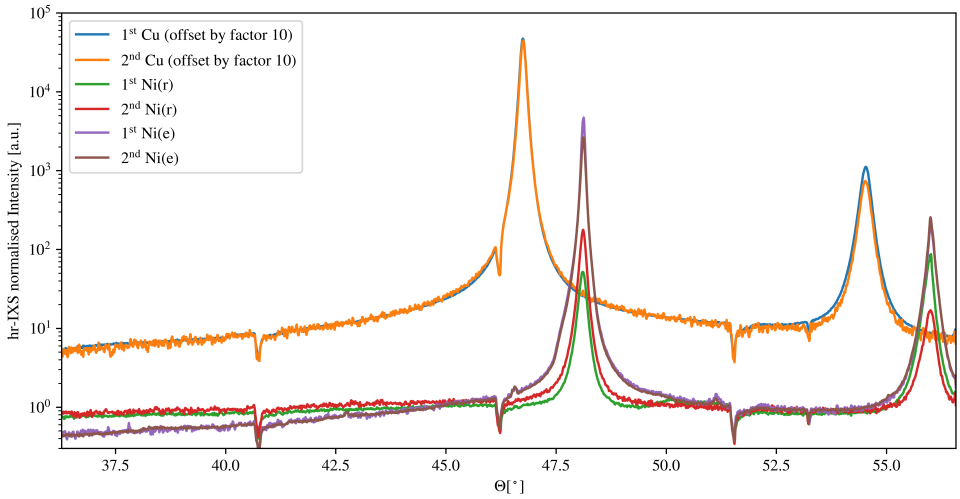

Figure 4.14: Diffraction line outs of p2656 obtained from radial summation along Φ. The signal of each batch was normalised by the number of hr IXS photons detected within that batch. The Cu signal was offset by one order of magnitude for clarity. In addition to the $\{1,1,1\}$ and $\{2,0,0\}$ Debye-Scherrer peaks, elastic intensity decreasing with peak distance can be seen. At 41°, 46°, and 51°, a drop of signal due to the detector pixel gaps can be found; similarly at 53° for a vertical mask. Due to the different sample positions, there are slight deviations of peak heights within each element arising from different illumated grains.

homogeneous Debye-Scherrer ring (averaging over more grains). However, whilst Γ of Ni(e) is significantly larger than that of Cu and Ni(r), there is no clear inverse correlation between Γ and σ. The stray signal of variable extent and intensity found on the detector chip, which depends on the sample mount position, should only affect the fainter parts of the diffraction signal and cannot be ruled out to alter the background of Ni(r), causing the atypical decay. Overall, the grain statistics were quite poor, where a few dominant grains cause asymmetries in the Debye-Scherrer rings and profiles, which limits the depth of analysis possible.

4.6 Summary

The aim of the work in this chapter is to inform experiments on expected signal strengths of IXS and QES through insight gained from the simulations and the past experiments presented here. From the inelastic Thomson cross section, a numerical code was presented that can

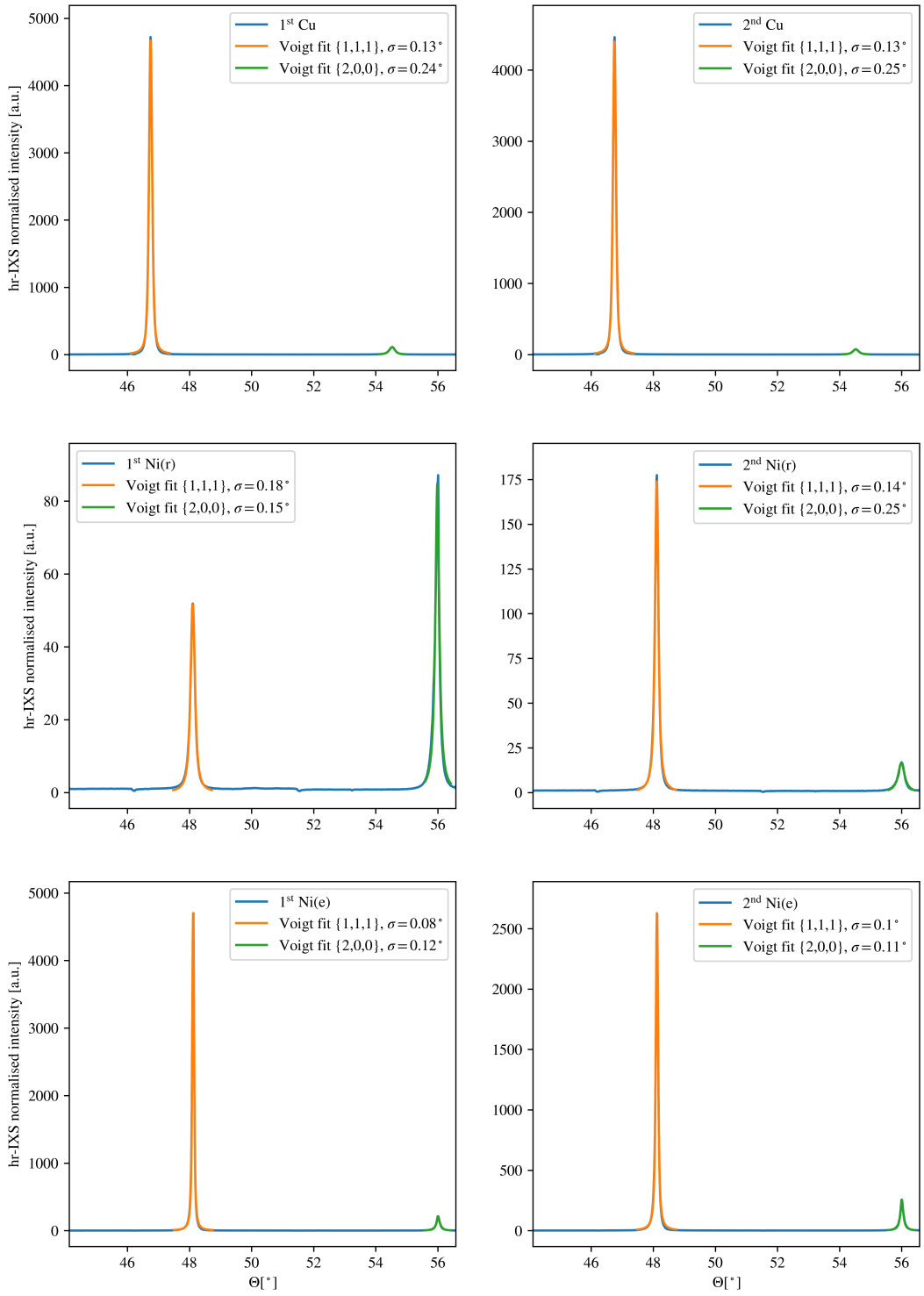

Figure 4.15: Voigt fits of the $\{1,1,1\}$ and $\{2,0,0\}$ Debye-Scherrer rings. The fits converge well around the intense parts, yet cannot describe the decay between the peaks which does not follow the Voigt shape. Overall, the FWHM of rolled Nickel is found to be the widest.

predict the intensity originating from crystalline targets, provided the beamline transmission and detector efficiencies are characterised. Hereby, the code successfully modelled the relative IXS between Cu, Ni, and Co to within the experimental error bars.

In addition to these IXS considerations, numerical work on the polycrystalline QES signal was showcased. Whilst the decay of Bragg peaks to assess the microstructure of samples is a whole field in itself, cf. SAXS, a route was laid out towards a rough understanding of the effect of crystallite shape functions and stacking faults that aids the design and interpretation of realistic shock experiments.

Lastly, the Debye-Scherrer diffraction found in p2656 shows significant structure within the $\{1, 1, 1\}$ and $\{2, 0, 0\}$ rings. Additionally, since the detectors were very close to the direct beam, sample position dependent direct scatter is detected. Both cause the line out background and peak width to vary and no reliable deduction of the grain structure/size of each foil can be made. There is a tendency that suggests that Ni(e) has less homogeneous Debye-Scherrer rings, which could explain the presumed high QES contribution to the Ni(e) hr IXS fits that will be outlined in Chapter 5: a dominant grain could be close to the probed spot in reciprocal space.

Future work will be centred around expanding the photon code capacity towards shocked polycrystals (average over pressure and temperature states) and advancements made at the experimental facilities. Concerning the latter, once the transmitted XFEL intensity can be characterised, it will be possible to further calibrate the IXS code, as for now, due to the significant monochromatisation, the (relative) photon flux onto the sample was too low to be detected with the current photodiodes installed at the HED instrument. Furthermore, with additional diffraction detectors covering a wider Φ section than merely 20° of the Debye-Scherrer rings, valuable predictions about the strength of QES collected by the hr IXS spectrometer can be made.

Chapter 5

Towards a Dynamic X-Ray Temperature and Microstructure Diagnostic of Polycrystals

5.1 Introduction

As introduced in Chapter 3, Equation 3.2, hr IXS can be used as a temperature diagnostic by applying the principle of detailed balance to phonon spectra. To successfully do so, the instrument function needs to be able to resolve the phonons with energies on the order of meV and the photon signal strong enough to reduce the limiting effect of shot noise. The work about the experiments p2191 and p2656 presented here aims at extending this measurement to dynamic experiments using XFELs and drive lasers. At the run p2191, collaborators from SLAC successfully obtained the temperature of ambient and resistively heated monocrystalline diamond[145]. This thesis reports on the Oxford results for polycrystalline metal foils for the commissioning run p2191, and for an extended setup in p2656, informing future experimental campaigns at further developed 4^{th} generation x-ray sources.

The structure of this chapter is as follows: first, further processing of the hr IXS detector images of the experimental setups of p2191 and p2656 at the EuXFEL HED instrument through polynomial unwarping will be described. Calibrated through PMMA shots, the first XFEL hr IXS spectra for cobalt, copper, and two nickel foils will be presented. One Ni foil was manufactured through rolling, and one through electrodeposition, resulting in a different microscopic grain structure. It will be shown that for p2191, the photon level is too low for IXS or QES to be extracted and the signal dominated by shot noise. In contrast, p2656 suffered from an instrument function three times as wide as the phonon energies to be resolved. Albeit the signal level in this second experimental campaign is much higher, and a clear spectral asymmetry is found (attributed to the Stokes and anti-Stokes peaks), a fit error analysis with the Markov Chain Monte Carlo method suggests that a significant

challenge in the parameter extraction remains.

5.2 High-Resolution IXS Spectra

In this section, the post-processing of the hr IXS detector images for p2191 and p2656 will be presented in order to obtain calibrated spectra like shown in Figure 2.6.

5.2.1 Advanced Processing of p2191 SPC Images

The raw SPC images obtained in the previous chapter exhibit three regions of interest corresponding to each of the three DCAs. The main direction of energy dispersion is along the vertical. Due to the imaging of the XFEL spot via the DCAs onto the detector (i.e., the image on the ePix100 is a projection of a radiation cone emerging from the DCAs) the three line outs have a finite curvature along their equi-energy lines and are unwarped via a subpixel shift routine. At this, each pixel is split up into 8×8 subpixels and the maxima for each vertical pixel strip in each of the three ROIs is determined. Then, approximating a conic intersection of large radius of curvature, a 2^{nd}-order polynomial is fitted and each vertical pixel stripe shifted such, that the polynomial is flattened to a constant. As an example, the result for analyser 0 (left) can be seen in Figure 5.1.

The line outs can then be found by summing along the horizontal. The elastically scattered photons will remain at their initial energy of 7,492 eV, which is used as a calibration for the energy-transfer zero. It is found by fitting the line out with a Voigt profile, modelling the instrument function consisting primarily of contributions from finite XFEL, hr monochromator and DCA bandwidth, and detector pixel size. The dispersion of about 9 meV per pixel is found through Equation 4.3, where the central XFEL energy E is inferred from the Bragg angle through a monochromator beam offset scan in a known geometry[146].

The resulting calibrated line outs for PMMA at 12° and 21° are shown in Figure 5.2 and 5.3 respectively, where the influence of shot noise can be seen through the error bars. The

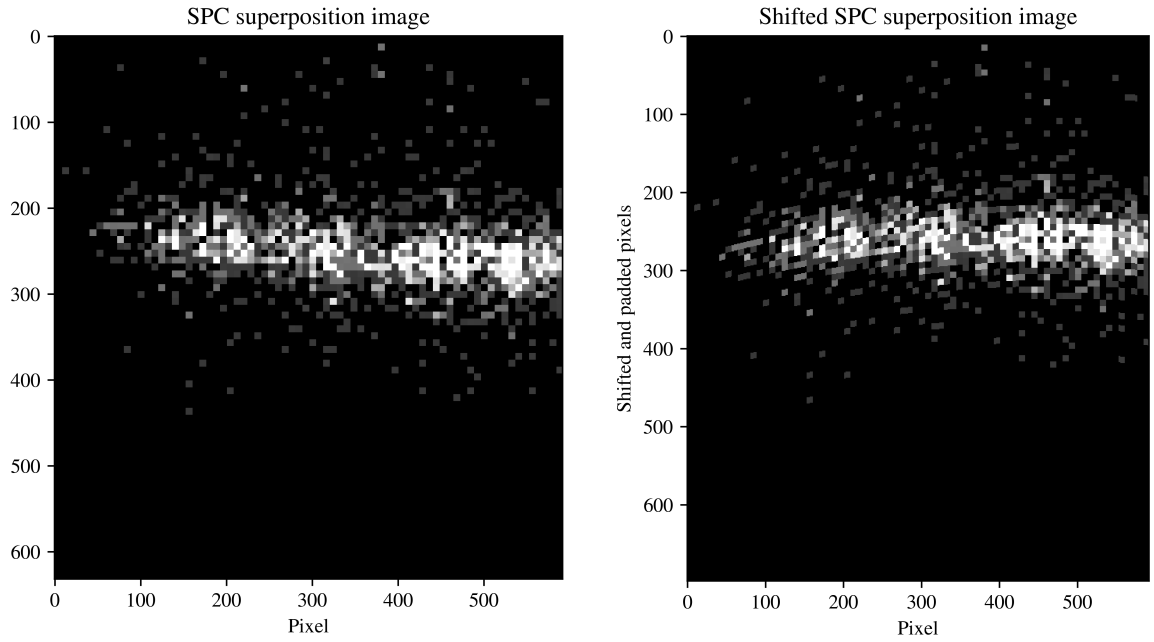

Figure 5.1: Example of curvature-corrected single photon image of all PMMA runs at 21° in equivalent experimental configuration for the ROI of analyser 0. Left, the raw image with a finite curvature is contrasted to the corrected image on the right.

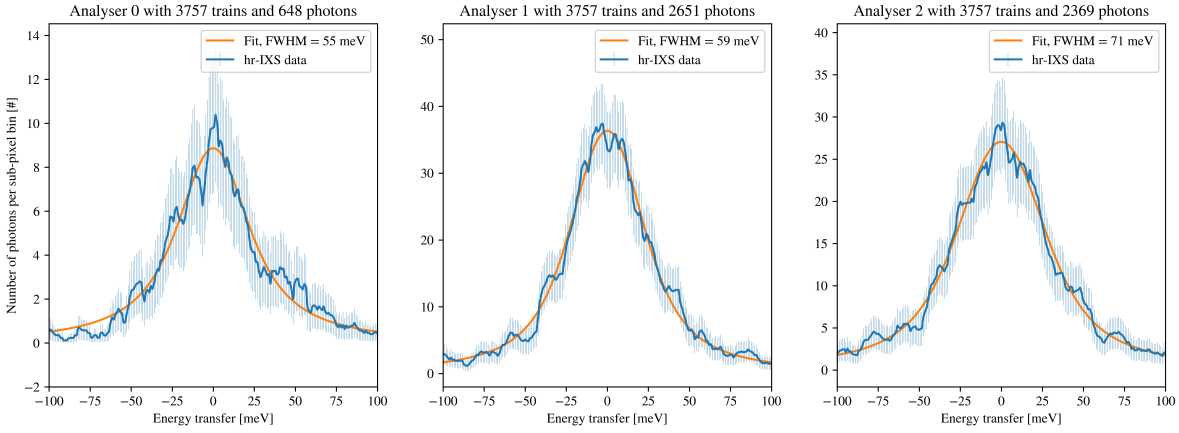

Figure 5.2: PMMA hr spectra of p2191 at 12°. The unwarped data with shot noise error bars and Voigt fits are plotted for each DCA. The instrument function of analyser 0 is best and as low as 55 meV, yet its photon count is the lowest which is assumed to arise from lower reflectivity due to higher surface roughness. Analyser 2 suffered from a significantly wider instrument function due to misalignment.

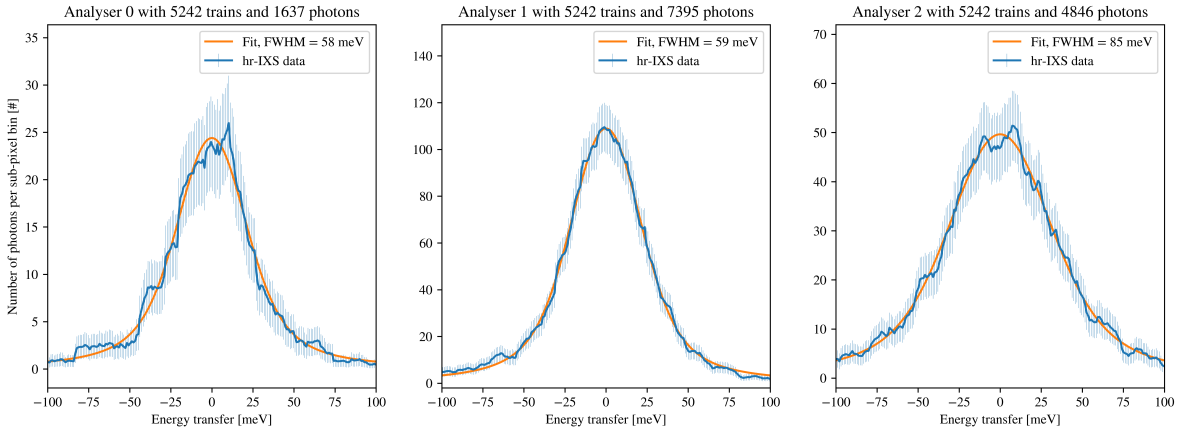

Figure 5.3: PMMA hr spectra of p2191 at 21°. The unwarped data with shot noise error bars and Voigt fits are plotted for each DCA. The instrument function of analyser 0 is best and as low as 58 meV, yet again its photon count is the lowest. Similarly, the instrument function of analyser 2 is the broadest.

instrument functions at 12° and 21° are (55, 59, 71) meV and (58, 59, 85) meV respectively for analysers (0, 1, 2). Note that the instrument function and photon count varies among analysers due to different alignment and DCA quality. Furthermore, for the same geometric reasons as outlined in Figure 4.2, the energy zero defined by the peak of the Voigt profile will shift for spectra recorded from samples positioned with a deviation Δz from the physical PMMA position along the XFEL optical axis.

5.2.2 Polycrystal Spectra of p2191

In the following, the line outs of p2191 from the polycrystalline metal foils are presented. Given a potential Δz upon changing targets with aid of the (imperfect) 2D-translation stage or from surface roughness, each spectrum can have a position-dependent shift along the energy axis. Thus, the runs have to be grouped into batches of equivalent experimental configuration. Only then can the line outs be added for improved statistics. Unfortunately, the significance of this effect has only been noticed after p2656.

In Figure 5.4, 5.5, 5.6 and 5.7, the line outs for the most intense batches for rolled Ni and Co at 12°, and rolled Ni and electrodeposited Ni at 21° respectively are shown. In addition

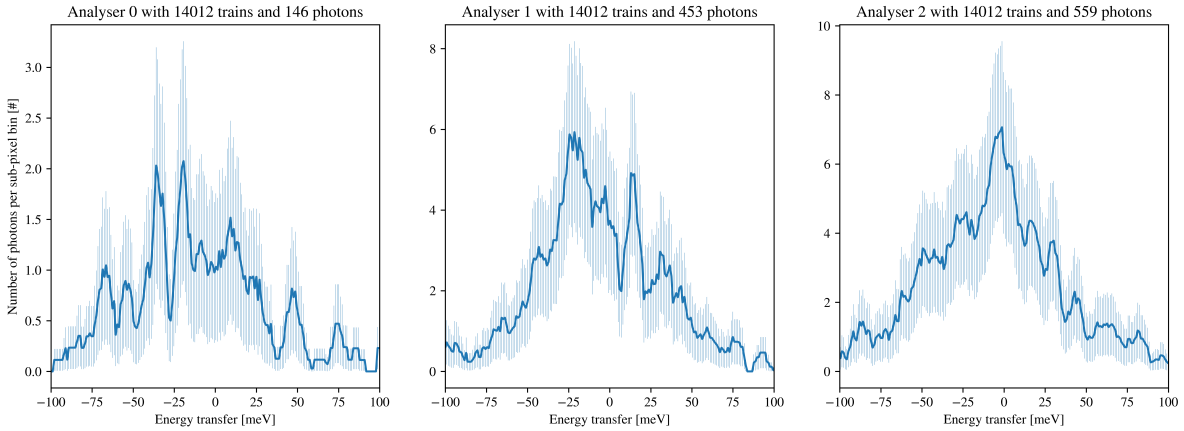

Figure 5.4: Rolled Ni hr spectra at 12°. The unwarped data with shot noise error bars are plotted for each DCA, where for the low photon signal the shot noise is significant.

to the spectra S (discrete functions of the subpixels) the shot noise errors σ_S are plotted, which scale as

$$\sigma_S = \sqrt{\frac{S^2}{S+1}}. \tag{5.1}$$

Also, the total number of trains and photons that gave rise to the spectrum are indicated, with a typical data acquisition time of only 1000 s. In principle, a (broadened) spectrum as shown in Section 2.3.2, Figure 2.6 is expected. Given the instrument function of 60 meV, and the phonons on the order of 30 meV, it is impossible to resolve the spectra for such low photon count. The latter was restricted due to the severe photon flux reduction from the SASE beam monochromatisation combined with the very limited experiment time.

5.2.3 Advanced Processing of p2656 SPC Images

For p2656, in addition to the change of detector from ePix100 to Jungfrau, a HAPG spectrometer[152] with a resolution of about 4 eV was added as an additional XFEL photon energy diagnostic. Since the data from the focus scan was corrupted (cf. p2191), the HAPG diagnostic is the only reliable quantification of the photon energy in p2656. It con-

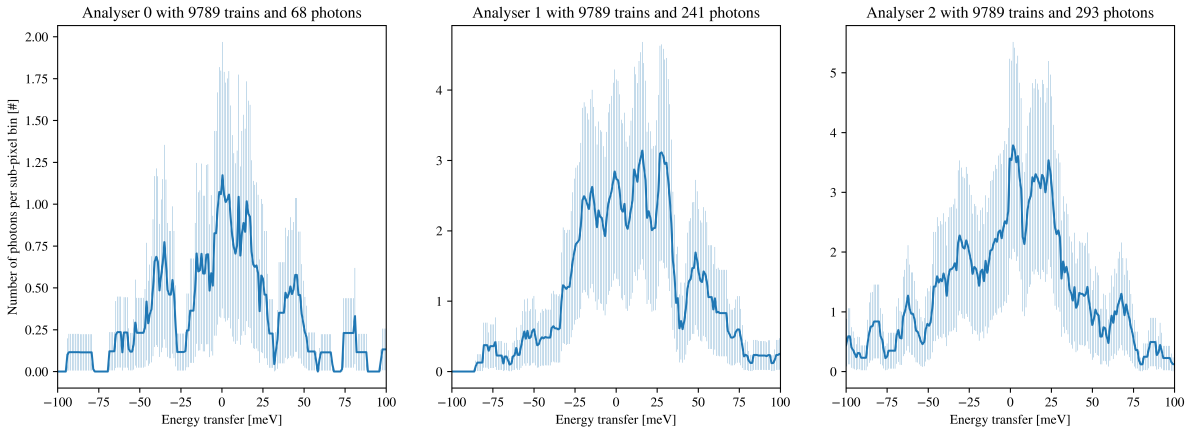

Figure 5.5: Co hr spectra at 12°. The unwarped data with shot noise error bars are plotted for each DCA. There is high shot noise.

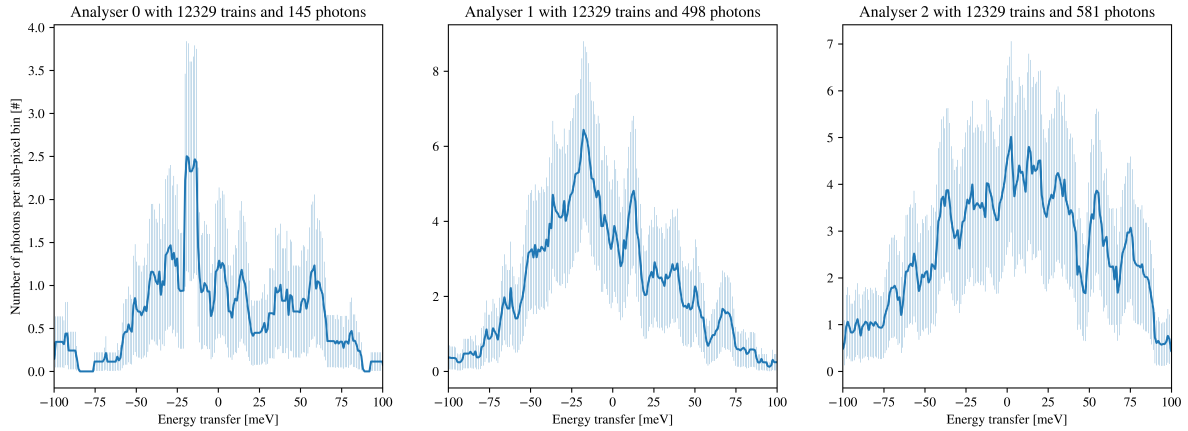

Figure 5.6: Rolled Ni hr spectra at 21°. The unwarped data with shot noise error bars are plotted for each DCA. Again, there is high shot noise.

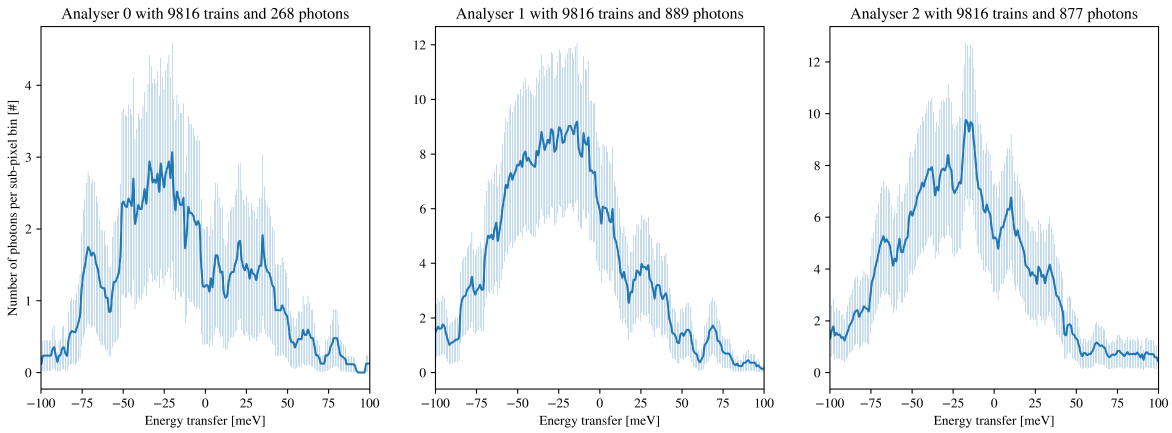

Figure 5.7: Electrodeposited Ni hr spectra at 21°. The unwarped data with shot noise error bars are plotted for each DCA. These runs of equivalent experimental configuration are the most intense of p2191, yet shot noise still is severe.

sists of a Jungfrau detector with a focussing and dispersing crystal using the (200) reflection of graphite, resulting in much higher transmission yet worse energy resolution than the Si (533). As described in Section 2.3.2, the dominating features of the backward XRTS spectra are a strong elastic peak at the XFEL energy in addition to a broad Compton feature at lower energies.

As for the hr IXS Jungfrau, first, the background and hot/cold pixel corrections are applied, where a typical detector image can be seen in Appendix C. Note that due to much higher photon flux onto the detector, no SPC can be applied. A narrow stripe along the focus of the main dispersion direction is summed perpendicular to its main direction of dispersion. The resulting spectra are calibrated using a linear dispersion and the known K_{α_1} lines of Ni and Co from dedicated calibration runs. Figure 5.8 shows the XRTS spectrum for PMMA, with the full spectral range on the left and a close-up of the fitted elastic peak on the right.

Analogously to p2191, the PMMA spectra are unwarped via subpixel shifting and a spectrum generated through summing along equi-energy lines. Using the HAPG energy, a dispersion of 18 meV per pixel is found with Equation 4.3. The resulting spectra and error bars for PMMA at 21° are shown in Figure 5.9, where the instrument functions of

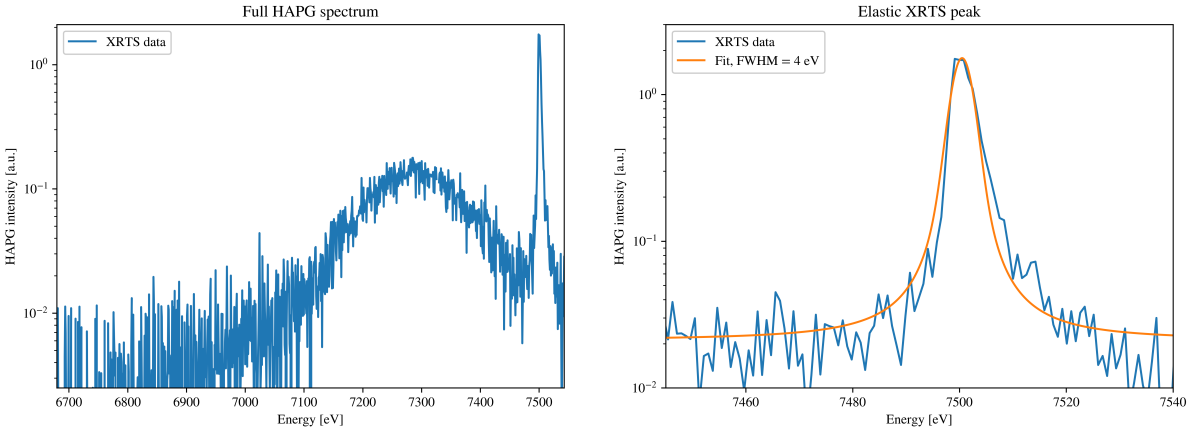

Figure 5.8: Left: full HAPG spectral range and spectrum for all p2656 PMMA runs of equivalent experimental configuration. Around 7.5 keV, the elastic XRTS feature can be seen, in addition to the broad Compton feature at lower energies. Right: Zoom into the elastic feature. The Voigt fit yields a FWHM of about 4 eV and a central XFEL photon energy of about 7,501 eV.

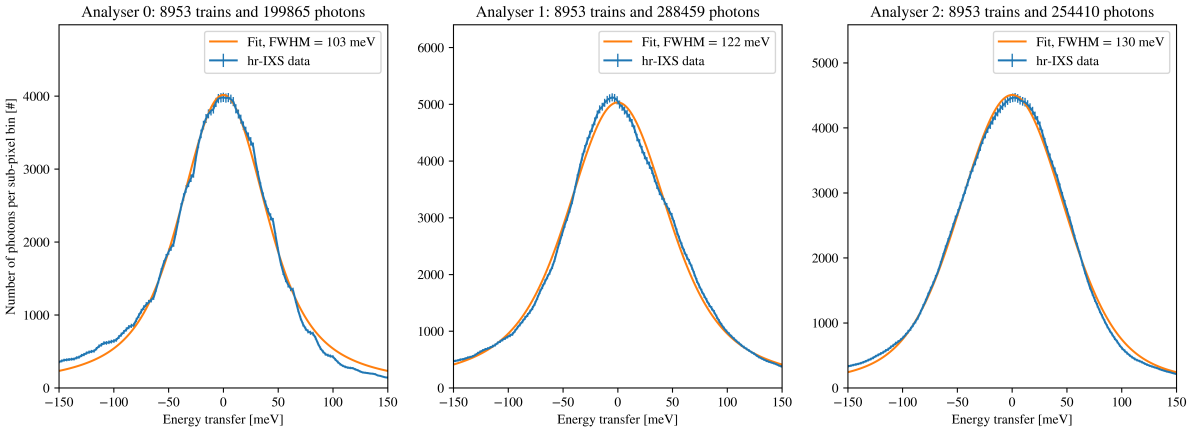

Figure 5.9: PMMA hr spectra of p2656 at 21°. The unwarped data with shot noise error bars and Voigt fits are plotted for each DCA. Similar to p2191, the instrument function of analyser 0 is best and as low as 103 meV that of analyser 2 is the broadest. The photon count is about 200 times as high as in the first campaign and shot noise very low. There are slight deviation of the data from the best Voigt fits due to the finite pixel size of the detectors and the slight asymmetry of the energy dispersion (cf. Equation 4.3).

(103,122,130) meV for analysers (0, 1, 2) are found through fitting Voigt profiles. As shown in Equation 4.3, because of the significantly higher XFEL photon energy the angular tolerance of DCA reflection is wider, and hence the instrument functions are on average 76% larger than they are for the same angle in p2191.

5.2.4 Polycrystal Spectra of p2656

Here, the spectra of p2656 from the polycrystalline metal foils of two batches of equivalent experimental configuration per element are presented for each DCA. In Figure 5.10 the line outs of the respectively strongest batches of copper (Cu), electrodeposited nickel (Ni(e)), and rolled nickel (Ni(r)) at 21° are shown. In Appendix D, the other nine spectra are given. Again, the error bars are found through Equation 5.1.

Whilst the photon signal is much higher in comparison to p2191, the significantly worse energy resolution broadens the spectra and impedes the analysis. However, even by eye the expected asymmetry is visible (skewed towards negative energy transfer), that would be expected when convolving the Stokes and anti-Stokes peaks with the instrument function. This sentiment is quantified through a discrete asymmetry metric of

$$\Lambda = \min_{k} \left\{ \sum_{n=1}^{m} \left| \hat{S}\left(n-k\right) - \hat{S}(-n) \right| \right\}$$

with the area-normalised discrete spectrum $\hat{S}$ of size m and $k \in [1, m]$. For $\Lambda = 0$, the input S is entirely symmetric, yet the higher Λ, the higher the asymmetry. In Figure 5.11, the results for the six batches of p2656 are plotted. Overall, there is a clear correlation between batches that featured the same target foil and their asymmetry: for a given material, the order of the analysers are the same and the value of Λ are similar. An exception is the 1$^{\text{st}}$ batch of Ni(e), which is attributed to its low photon signal/high shot noise, and the order of analysers between Cu and Ni(r), where analyser 1 at a more central position in the Rowland

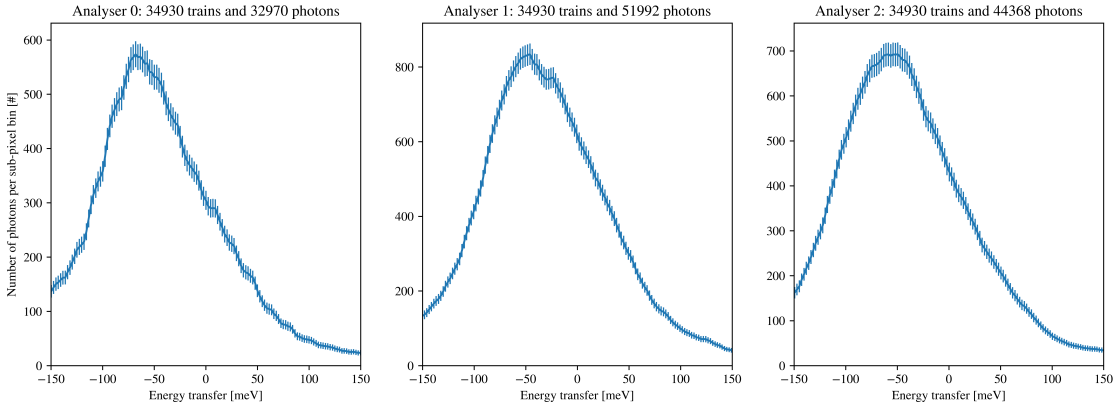

(a) 1st Cu batch.

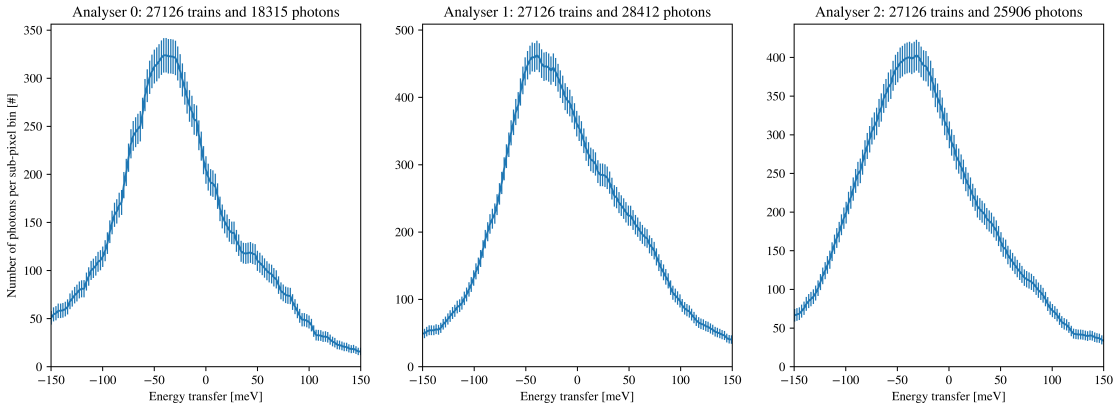

(b) 1st rolled Ni batch.

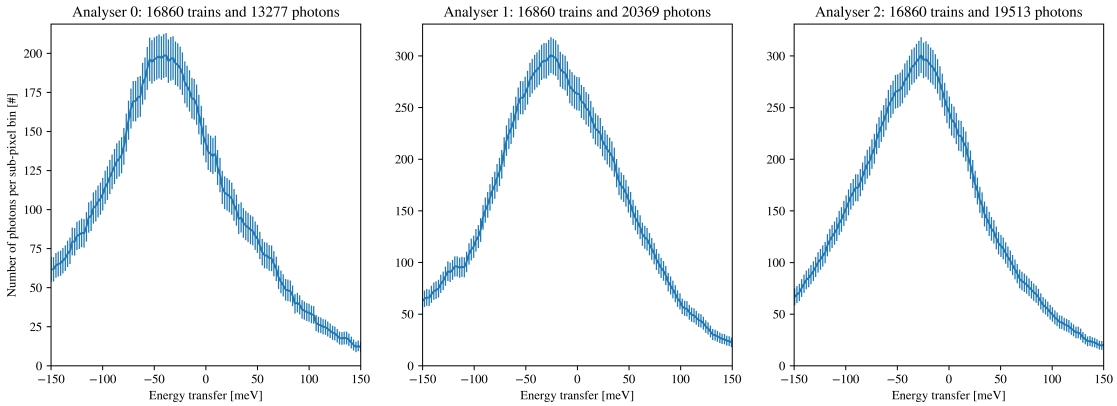

(c) 2nd electrodeposited Ni batch.

Figure 5.10: Strongest hr IXS p2656 batches at 21°. The unwarped data with shot noise error bars are plotted for each DCA, where the energy zero is relative to the PMMA calibration. Even for the wide instrument function, some asymmetry can be made out by eye.

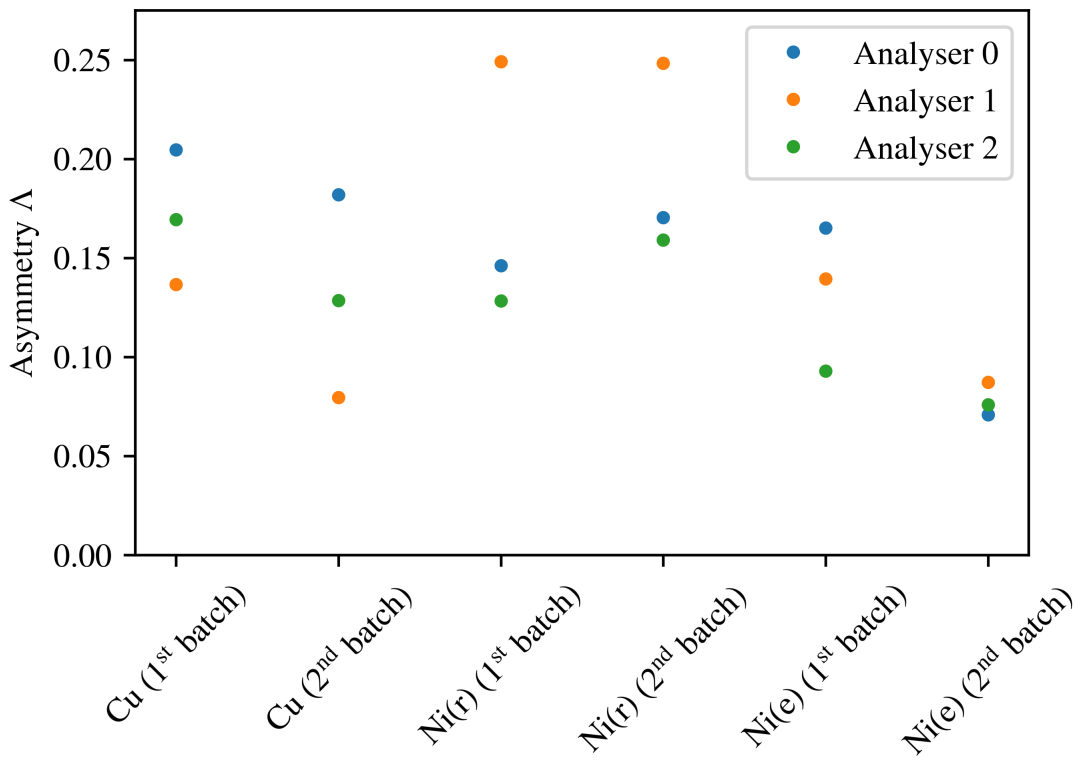

Figure 5.11: Asymmetry metric for the p2656 spectra as a function batch and analyser. On average, Cu and Ni(r) exhibit more asymmetric spectra than the second batch of Ni(e), where the first Ni(e) batch is disregarded in this analysis due to its low photon photon.

geometry appears to be particularly volatile to potential Δz-misalignment. Other minor deviations of Λ are attributed to slight differences in potential QES and Δz. Overall, the 2^{nd} batch of Ni(e) exhibits the least asymmetry of all samples.

5.3 Parameter Extraction and Error Estimation of p2656

Given the lower shot noise (relative to p2191) and observed asymmetry, in the following an attempt is made at extracting information about the structure of the samples through fitting, followed by an error estimation on these extracted fit parameters.

Based on Section 2.3.2, the signal is expected to consist of the sum of three Voigt profiles, related to the Stokes, anti-Stokes, and potential quasi-elastic peaks. Their intrinsic width

is negligible compared to the wide instrument functions, consistent with indications from the classical simulations presented in Section 3.3.2. Hence, each of the 18 line outs (three samples, three analysers, two batches of equivalent experimental configuration) is modelled by the fit $F(\omega)$ given by

$$F(\omega) = \sum_{j \in \{1,2,3\}} I_j \cdot V\left(\omega - \omega_j, \alpha_{G,j}, \gamma_{L,j}\right),$$

where $\omega = E/\hbar$ is the energy transfer, ω_j the shift of peak j with intensity I_j, and V an area-normalised Voigt profile with the Gaussian $\alpha_{G,j}$ and Lorentzian $\gamma_{L,j}$ width contribution. These would be twelve parameters per spectrum, which would not converge reliably for the finite level of shot noise encountered throughout the experiment. Hence, it is crucial to significantly reduce the parameter space by adding constraints based on known physics:

1. Given the small peak separation, the dispersion across the DCA focus can be taken as linear and hence the instrument function for each peak is the set to be the same, i.e., the one determined via the PMMA runs.

2. The QES will be at zero energy change, hence $\omega_2 = 0$ meV. The Stokes and anti-Stokes peaks are at the same energy, hence $\omega_q \coloneqq \omega_1 = -\omega_3$, with the energy ω_q of the involved phonon at that scattering angle Θ. Furthermore, in a polycrystalline sample, numerous directions will contribute to the IXS signal, yet it is assumed to be dominated by phonons from the peak of the respective dispersion relations, where the slope tends towards zero and the density of states is the highest. Given the scattering angle is known, the dominant phonon can be read off the phonon dispersion relation of the material under investigation.

3. Given the varied sample positions (Δz) relative to the PMMA calibration target, the energy zero of the spectra can be shifted and ω is replaced with $\omega - \omega_s$, where ω_s parameterises this unknown shift.

4. Since the pixel dispersion and the diameter of the Rowland circle come with a significant uncertainty (4 eV resolution of the HAPG spectrometer, 20 cm error of the optimised sample to DCA to detector distance), a parameter a_s to scale the energy axis is added to not artificially constrain the fit.

5. Similarly, as also the instrument function itself varies as a function of Δz, a scaling factor b_s is added.

This would result in a fit as described by

$$\begin{aligned} F(\omega) = & I_1 \cdot V\left(a_s\left[\omega - \omega_s + \omega_q\right], a_s b_s \alpha_G, a_s b_s \gamma_L\right) \\ & + I_2 \cdot V\left(a_s\left[\omega - \omega_s\right], \quad a_s b_s \alpha_G, a_s b_s \gamma_L\right) \\ & + I_3 \cdot V\left(a_s\left[\omega - \omega_s - \omega_q\right], a_s b_s \alpha_G, a_s b_s \gamma_L\right) \end{aligned}$$

with 1, 2, 3 corresponding to Stokes, QES, anti-Stokes. The free fit parameters are I_1, I_2, I_3, w_s, a_s, and b_s, i.e., six in total per line out. The phonon energies ω_q of Cu are (30,29,30) meV and of Ni (35,34,35) meV for analyser (0 ,1 ,2) respectively. Then, through I_1 and I_3, the absolute temperature of the metal foils, and from I_2, information about the microstructure, could be obtained. Unfortunately, given the broad instrument function in combination with moderate shot noise, also in p2656 a temperature measurement (reproducing the know 298 K) is not feasible since the fits do not unambiguously converge.

However, in the following an attempt at extracting the QES signal is shown, where the parameter space is reduced even further by adding in the known constraint of the known ambient temperature. According to Equation 2.12, peak I_1 and I_3 are related by

$$\frac{I_1}{I_3} = \exp \frac{\hbar\omega_q}{k_B T},$$

which reduces the fit function to

$$\begin{aligned} F(\omega) = & I_1 \cdot V\left(a_s\left[\omega - \omega_s + \omega_q\right], a_s b_s \alpha_G, a_s b_s \gamma_L\right) \\ & + I_2 \cdot V\left(a_s\left[\omega - \omega_s\right], \quad a_s b_s \alpha_G, a_s b_s \gamma_L\right) \\ & + I_1 \cdot V\left(a_s\left[\omega - \omega_s - \omega_q\right], a_s b_s \alpha_G, a_s b_s \gamma_L\right) \cdot \exp \frac{\hbar \omega_q}{k_B T}, \end{aligned}$$

leaving five free parameters per line out. Whilst still challenging, this multidimensional problem is explored via the Machine Learning algorithm `maleo` as used by Kasim[210], employing a covariance matrix adaptation evolution strategy (CMA-ES)[211] to find the best fit in combination with a Markov chain Monte Carlo ensemble sampler (EMCEE)[212] to get an understanding of the convergence of each parameter. Given the discrete signal of single photons, the following cost function is used:

$$\text{cost} = \sum_{n=1}^{m} \frac{\left[S(\omega_n) - F(\omega_n)\right]^2}{\left|S(\omega_n) + 1\right|}$$

with the discretised energy axis ω_n.

In Figure 5.12, 5.13, and 5.14, the line outs and CMA-ES fit of the three targets are presented, where the final parameters are given in Table 5.1. Furthermore, the representative EMCEE exploration for 1$^{\text{st}}$ Cu and 1$^{\text{st}}$ Ni(e) batch can be found in Figure 5.15 and 5.16, whilst the other parameter sensitivities are shown in Appendix E.

The Cu and Ni(r) data is in good agreement with the fits and no parameter limits are hit, whereas both batches of the Ni(e) data struggle to converge; particularly the 1$^{\text{st}}$ batch will be excluded in further commentary due to its much lower signal-to-noise ratio. The Ni(e) fit oscillation, and lack thereof in Cu and Ni(r), is attributed to a presumably higher/significant QES contribution to Ni(e) indicated by the lesser asymmetry found in the previous section. This suggests that instead of two Voigt peaks of about 60 meV spacing in the Ni(e) case, three peaks with only 30 meV have to be resolved.

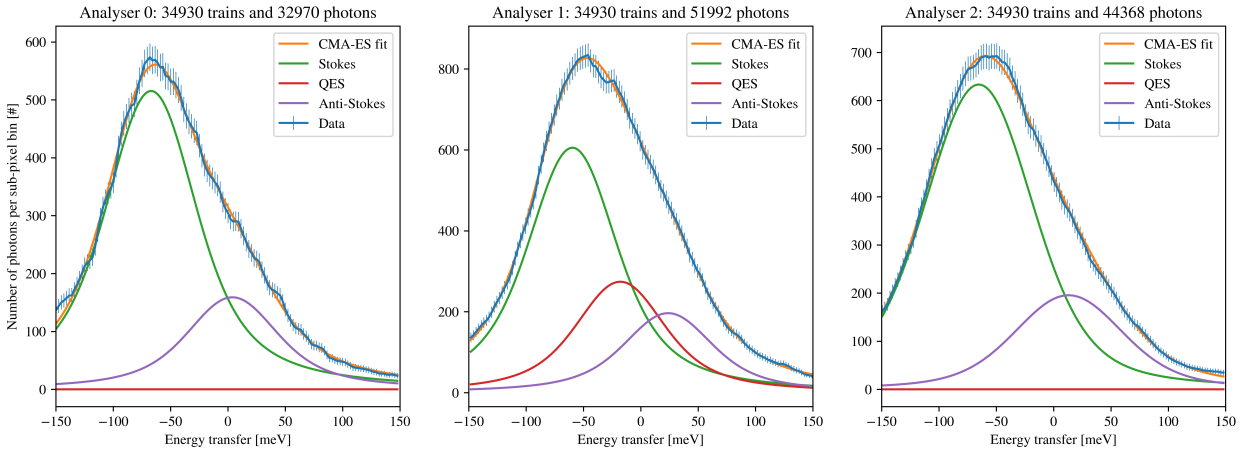

(a) 1st Cu batch.

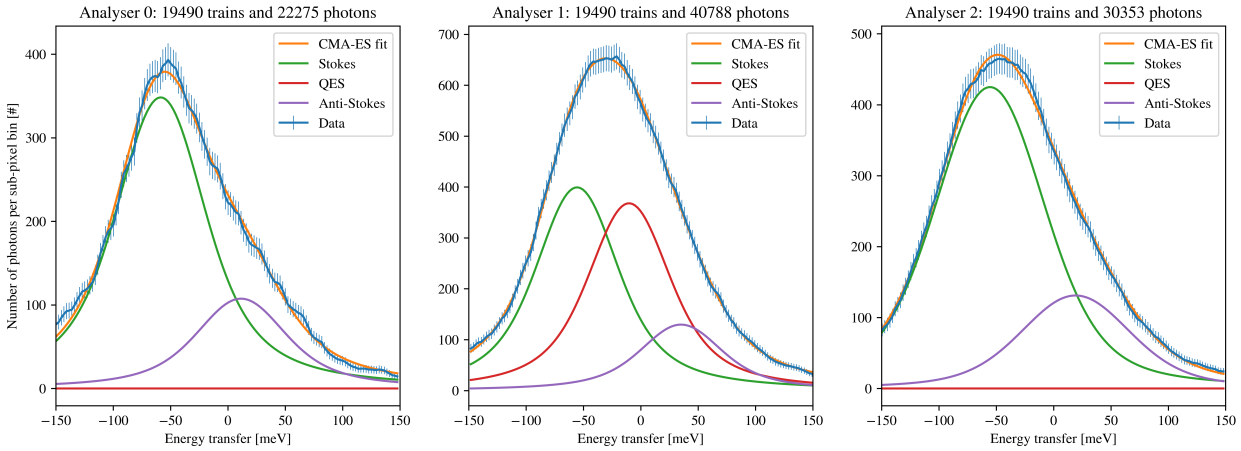

(b) 2nd Cu batch.

Figure 5.12: Cu hr IXS p2656 batches at 21°. The unwarped data with shot noise error bars together with the CMA-ES fits are plotted for each DCA, where the energy zero is relative to the PMMA calibration. The fit parameters are in Table 5.1.

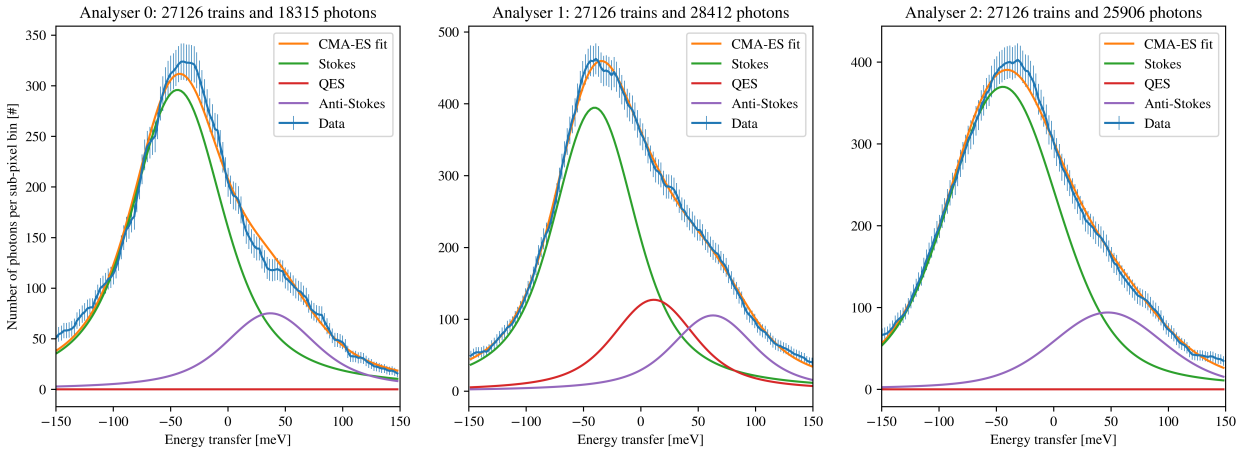

(a) 1st Ni(r) batch.

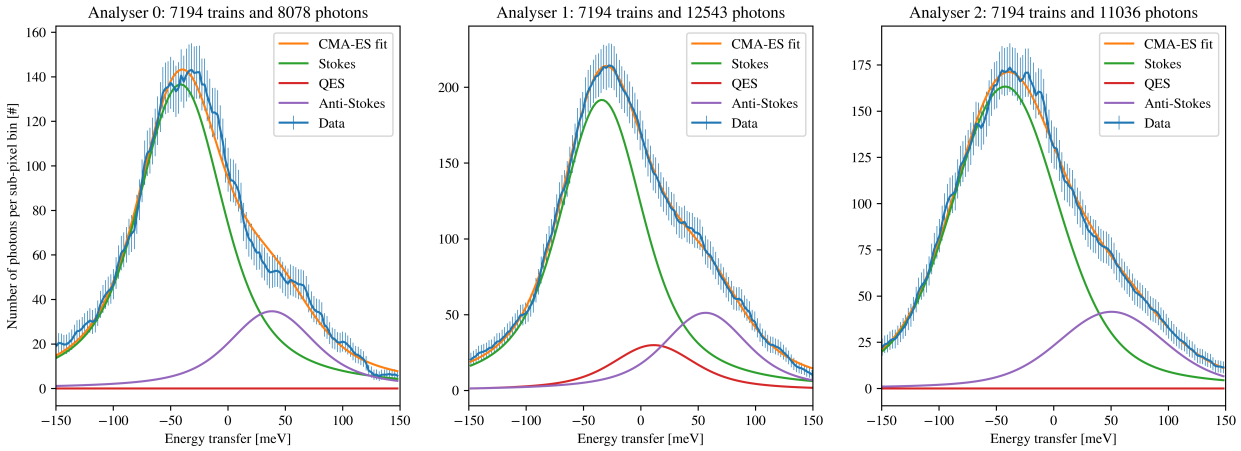

(b) 2nd Ni(r) batch.

Figure 5.13: Ni(r) hr IXS p2656 batches at 21°. The unwarped data with shot noise error bars together with the CMA-ES fits are plotted for each DCA, where the energy zero is relative to the PMMA calibration. The fit parameters are in Table 5.1.

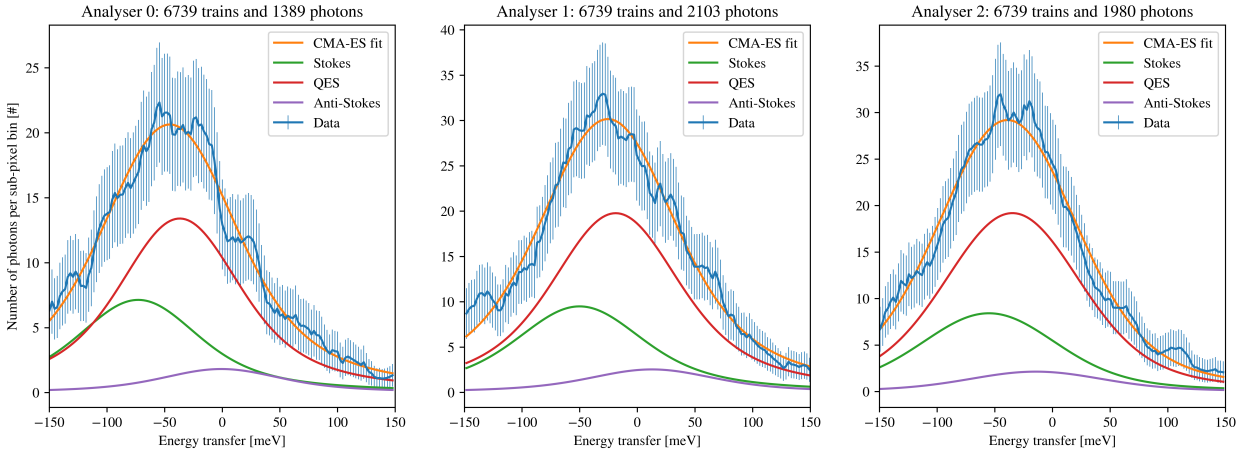

(a) 1st Ni(e) batch.

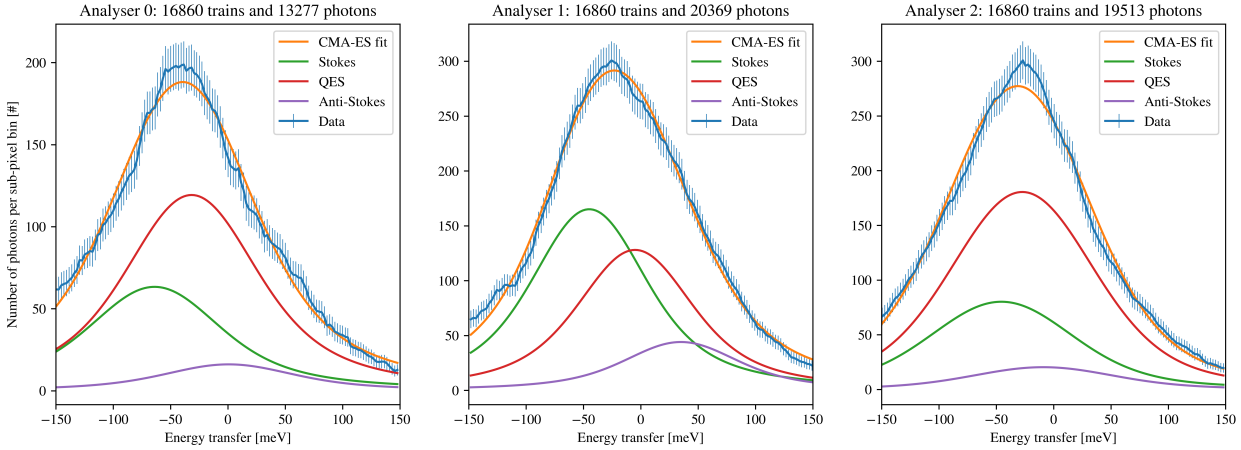

(b) 2nd Ni(e) batch.

Figure 5.14: Ni(e) hr IXS p2656 batches at 21°. The unwarped data with shot noise error bars together with the CMA-ES fits are plotted for each DCA, where the energy zero is relative to the PMMA calibration. The fit parameters are in Table 5.1.

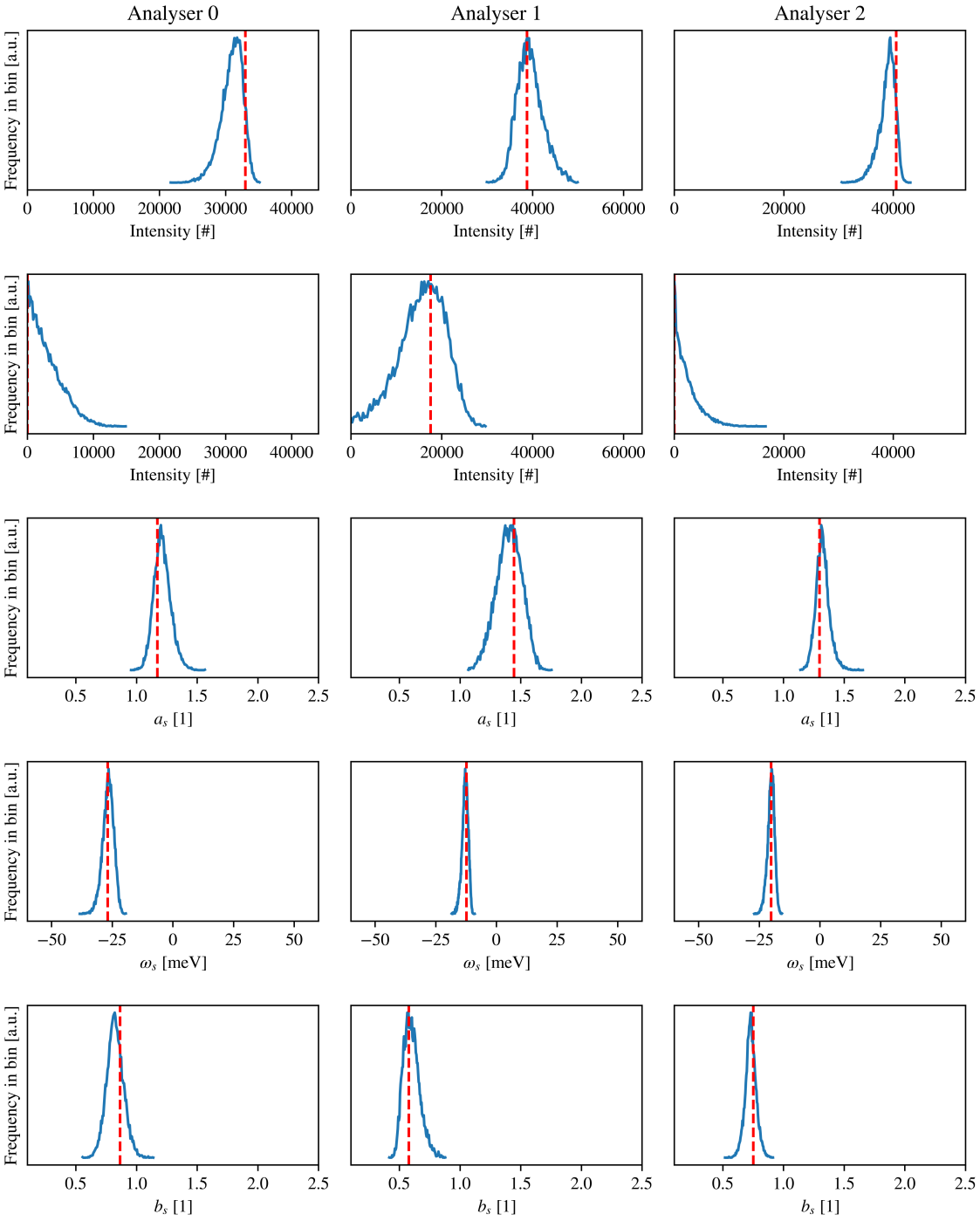

Figure 5.15: CMA-ES parameter sensitivity obtained through EMCEE exploration for the first Cu batch with about 50,000 EMCEE samples per analyser. The best fits are indicated by dashed orange lines and narrow distributions around these are found. The uncertainty is the largest for the central DCA.

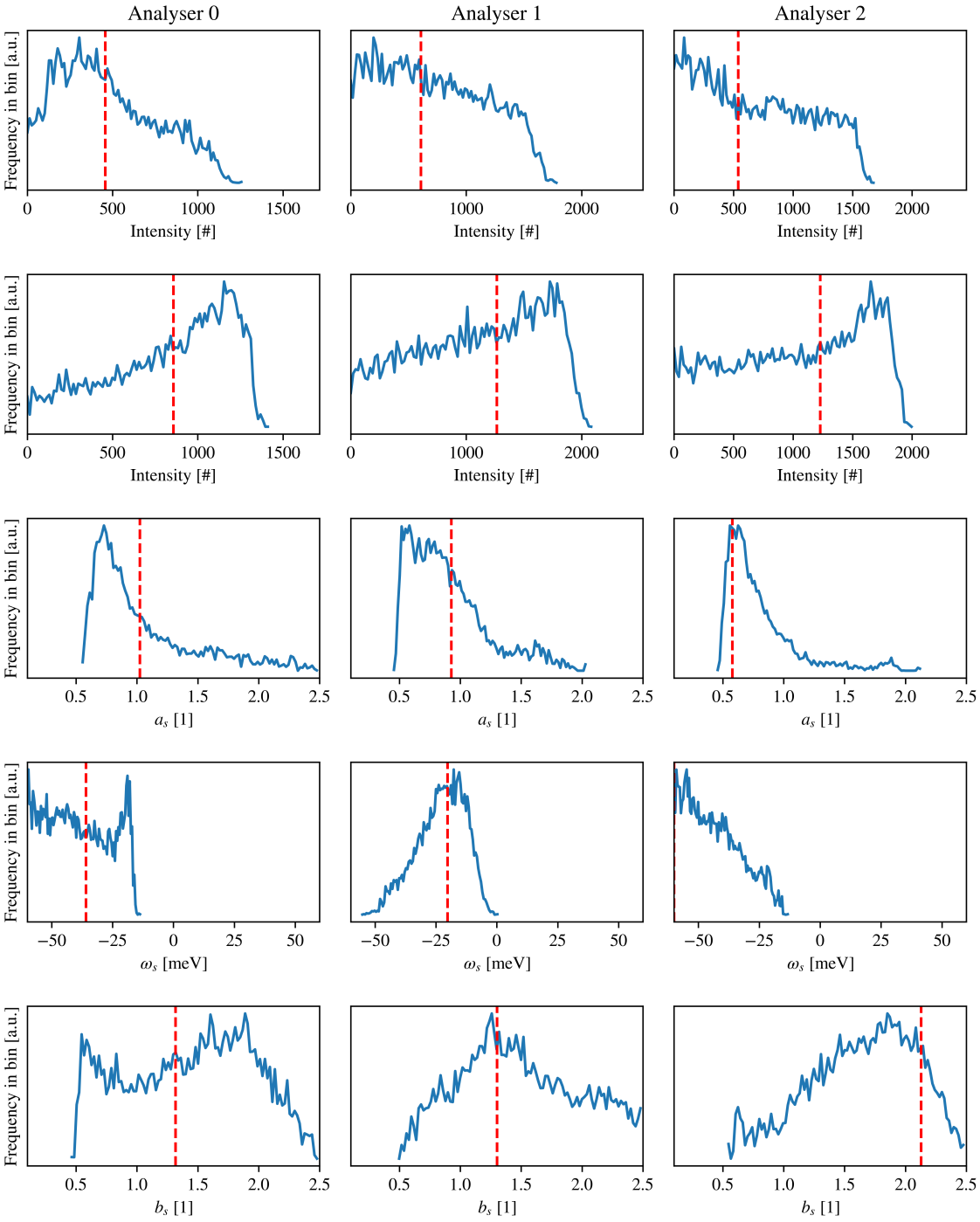

Figure 5.16: CMA-ES parameter sensitivity obtained through EMCEE exploration for the first electrodeposited Ni batch with about 50,000 EMCEE samples per analyser. The best fits are indicated by dashed orange lines. The fit cost is largely insensitive to significant parameter variation and no reliable convergence could be found.

Spectrum	Analyser	I_1	I_2	a_s	ω_s	b_s
Cu (1^{st})	0	32979	0	1.17	-27	0.86
	1	38745	17545	1.44	-12	0.58
	2	40538	0	1.30	-20	0.75
Cu (2^{nd})	0	22292	0	1.16	-20	0.86
	1	25555	23551	1.57	-7	0.49
	2	27188	0	1.23	-15	0.80
Ni(r) (1^{st})	0	18930	0	1.15	-3	0.87
	1	25241	8135	1.52	7	0.50
	2	23662	0	1.30	1	0.77
Ni(r) (2^{nd})	0	8740	0	1.13	-1	0.83
	1	12265	1912	1.33	8	0.58
	2	10449	0	1.32	3	0.73
Ni(e) (1^{st})	0	457	857	1.02	-36	1.32
	1	607	1265	0.93	-20	1.30
	2	538	1228	0.58	-60	2.13
Ni(e) (2^{nd})	0	4053	7636	0.92	-34	1.61
	1	10563	8194	1.18	-4	0.92
	2	5131	11550	0.52	-53	2.50

Table 5.1: Final results of the CMA-ES fits for all 18 spectra of p2656. The fit limits are $I_{1/2} \in [0, 1.2 \cdot S_{max}]$, $a_s \in [0.1, 2.5]$, $\omega_s \in [-60, 60]$, and $b_s \in [0.1, 2.5]$ where scaling parameters that are hitting the limits are highlighted in red.

However, whilst a consistently larger-than-unity a_s suggests that the XFEL energy was slightly underestimated, the central DCA Ni(r) and Cu results for a_s vary much more than the HAPG uncertainty $\sigma_E = 4\,\text{eV}$ and unknown sample to DCA to detector distance of $\sigma_l = 2 \cdot 10\,\text{cm}$ would suggest. According to the propagation of uncertainty for these independent variables, the error on the dispersion ΔE from Equation 4.3 is given as

$$\sigma_{\Delta E} = \sqrt{\sigma_E^2 \frac{\partial \Delta E}{\partial E} + \sigma_l^2 \frac{\partial \Delta E}{\partial l}}$$

For $E = 7,501$ eV and $l = 1$ m, this corresponds to a scaling of a_s between 0.76 and 1.24.

Whilst the results in Table 5.1 show that the fits can still distinguish between central and

outer analysers, the stark variation of a_s in combination with the chancy occurrence of QES only for the central analyser for Ni(r) and Cu suggests a systematic deviation. In p2656 due to the added freedom of shifting/scaling the energy axis and a variable instrument function, the fits are not sufficiently constraint. Hence, with the given shot noise level, ambiguous solutions are possible and neither temperature T nor QES I_2 can be extracted.

5.4 Summary

Whilst measuring the absolute temperature of solids through phonons is an established procedure for static experiments on a wide range of samples, advances in the dynamic range are quite recent. For well-behaved samples of monocrystalline diamond, Descamps[145] found in p2191 the ambient and resistively heated temperature. This chapter gave insight into the first polycrystalline metal foil endeavour via the two EuXFEL campaigns p2191 and p2656, aiming at extracting the absolute temperature and information about the microstructure of the targets, where both runs faced their individual experimental challenges.

In p2191, the photon count was extremely low due to the SASE beam losing a significant amount of pulse energy upon monochromatisation, and the extremely short experimental time at that commissioning run. In p2656, whilst the total number of photons collected was much higher due to XFEL seeding and more experiment time, the instrument function was about three times as broad as the peak separation to be resolved.

This results in the p2191 metal foil spectra signal-to-noise ratio being very poor where no peaks can be resolved and hence neither temperature nor microstructure extracted. In contrast, the p2191 part by Descamps[145] successfully obtained temperature, and, through the lack of a QES contribution, a confirmation of the sample monocrystallinity. The main differences here were the wider phonon spacing, the lack of a third, quasi-elastic peak to resolve, and the higher photon count through much longer integration time (in addition to intrinsically higher signal strength as found in Section 4.2).

These results encouraged p2656, where a higher photon count through increased flux and time was available. Hence, the results of p2656 suffered much less from shot noise. Yet the wide instrument function due to a suboptimal central XFEL photon energy complicated the analysis: whilst the Cu and Ni(r) spectra show a high asymmetry and the fits are more stable, the models struggle for the Ni(e) runs. The latter is the most symmetric (possibly due to a close strong Laue contribution in this more granular sample) and the fits find strong QES. They are not as clear (EMCEE explores rather wide) as for such instrument functions the three peaks (QES, Stokes, and anti-Stokes) cannot be resolved as well as if there were only two (Stokes and anti-Stokes).

Due to the error on the XFEL energy and sample positions, three scaling parameters had to be added. The energy dispersion scale a_s in particular is found to be inconsistently large compared to the experimental uncertainties on sample DCA detector distance and XFEL energy resolution. Overall, due to too little constraint of the parameter space, whilst the temperature could not be measured, some asymmetry of the spectra was seen. Future campaigns will require improvements particularly from the resolution side and the experimental implementation of reliable sample positioning.

Chapter 6

Conclusion

6.1 Summary

In this thesis, work on the development of a temperature and microstructure diagnostic using Thomson scattering was presented. Hereby, MD simulations on shocked crystals helped understanding the scattering signal in shocks and the experimental high-resolution x-ray spectra of ambient metals were analysed.

In Chapter 3, a Cu monocrystal was shock compressed to 0-70 GPa and its Thomson signal computed through Fourier transforms in space and in time. At higher pressure, the phonon energies increase, causing a wider Stokes- and anti-Stokes peak spacing, which will benefit any temperature measurements relying on resolving them. At the same time, compression beyond the elastic limit will generate defects such as stacking faults and thereby a highly directional QES contribution, which connects certain Bragg peaks and potentially poses a challenge to resolving the IXS signal. Whilst this QES signal can affect the temperature measurements, it can also serve as a simultaneous microstructure diagnostic, where, depending on the defect structure, only certain reciprocal space regions will exhibit such quasi-elastic peaks. Furthermore, in the same chapter a simple prediction about a shock-induced relativistic Doppler shift of the energy-resolved Thomson scattering outlines a novel diagnostic for directly measuring the particle velocity U_p behind a shock front, rather than relying on VISAR which is only sensitive to the rear surface velocity.

In Chapter 4, work on elastic and inelastic Thomson signal strength prediction was presented in order to inform the design of future experiments. A photometrics code was showcased that is based on the Thomson cross section, which was able to model the relative IXS strength of Cu, Ni, and Co of p2191 and p2656 within the experimental uncertainty. Absolute predictions can be obtained if the XFEL intensity on the target and the DCA

efficiencies are known. Additionally, numerical work on various crystallite shapes aimed at providing a qualitative understanding of QES signal. Hereby, also a mock polycrystal outlined future MD routes towards predicting relative intensities in faulted samples. This was concluded with the analysis of Debye-Scherrer diffraction recorded throughout p2656, where the signal suffered from poor grain statistics and direct stray intensity, hindering a potential QES estimate.

In Chapter 5, the hr Thomson spectra of the experimental campaigns p2191 and p2656 for polycrystalline Ni, Co, and Cu foils were presented. Their shared goal was to extract the absolute temperature together with information about the sample microstructure, where two different types of Ni were investigated. In the HED commissioning experiment p2191, a SASE beam was monochromatised and sent onto the targets at two different scattering angles. For monocrystalline diamond at wider peak spacing, stronger scattering, and longer integration times, the sample temperatures could be extracted. However, due to the low total photon count arising from monochromatisation and limited experimental time, the signal-to-noise ratio of the metal targets was extremely poor and the Stokes/anti-Stokes or QES peak extraction was rendered unfeasible. In the following campaign p2656 with more experimental time available, further EuXFEL development had taken place and a seeded beam provided higher photon flux. This reduced the shot noise of the spectra taken of the Cu and Ni foils, however, the instrument function turned out to be much broader due to an unfavourable central x-ray energy. Even given a clear spectral asymmetry, the fits turned out to be unreliable as the parameter space was too large, and hence, neither absolute sample temperature nor QES contribution could be extracted.

6.2 Further Work

For future MD investigations in addition to different crystal structures and materials, it will be instructive to investigate shock compression of fcc structures along other crystal axes of

high symmetry than the [001] direction to produce more isotropic plasticity[213]. Shocks propagating along [111] and [110] are expected to primarily affect the density of generated stacking faults and thereby the QES along the corresponding linear features in reciprocal space. Since many of the shock-compressed materials already are, or at some point in the compression process might be, in polycrystalline form, it also will be instructive to generate synthetic diffraction and phonon spectra of such systems consisting of a large number of grains.

Through being able to resolve the relativistic Doppler shift with hr setups such as found at the HED instrument, for future experiments a novel complement or alternative to VISAR measurements could directly obtain the particle velocity, where the expected energy shifts of tens of meV arise for average velocities on the order of several 1000 ms^{-1}. Hereby, the small size of the XFEL spot would ensure probing a limited volume, avoiding averaging over a wide range of particle velocities. This is particularly interesting for directly characterising ramp compression, where a gradient of material at different velocities contributes to the diffraction signal.

For the p2656 experiment presented, whilst the Ni(r) fits converge, a slight systematic shape deviation is found, which suggests that the model of Stokes, anti-Stokes and QES (three peaks) might be too simplistic for polycrystalline samples. In reality, many phonons of different directions and their projections are involved. In a perfect Debye-Scherrer sample (no inhomogeneity, e.g., a nanocrystalline powder), a distribution of scattering phonons could be calculated, however, here due to inhomogeneous samples, this is remains indeterminable.

At the same setup of p2191 for a central scattering angle of 8° and instrument functions on the order of 80 meV, Descamps led work on successfully extracting the temperature of ambient and resistively heated monocrystalline diamond[145], where the results are shown in Figure 6.1. The Stokes and anti-Stokes peaks with a spacing of about 59 and 87 meV are visible by eye and the fit results suggest temperature errors of a few tens of K. Whilst for

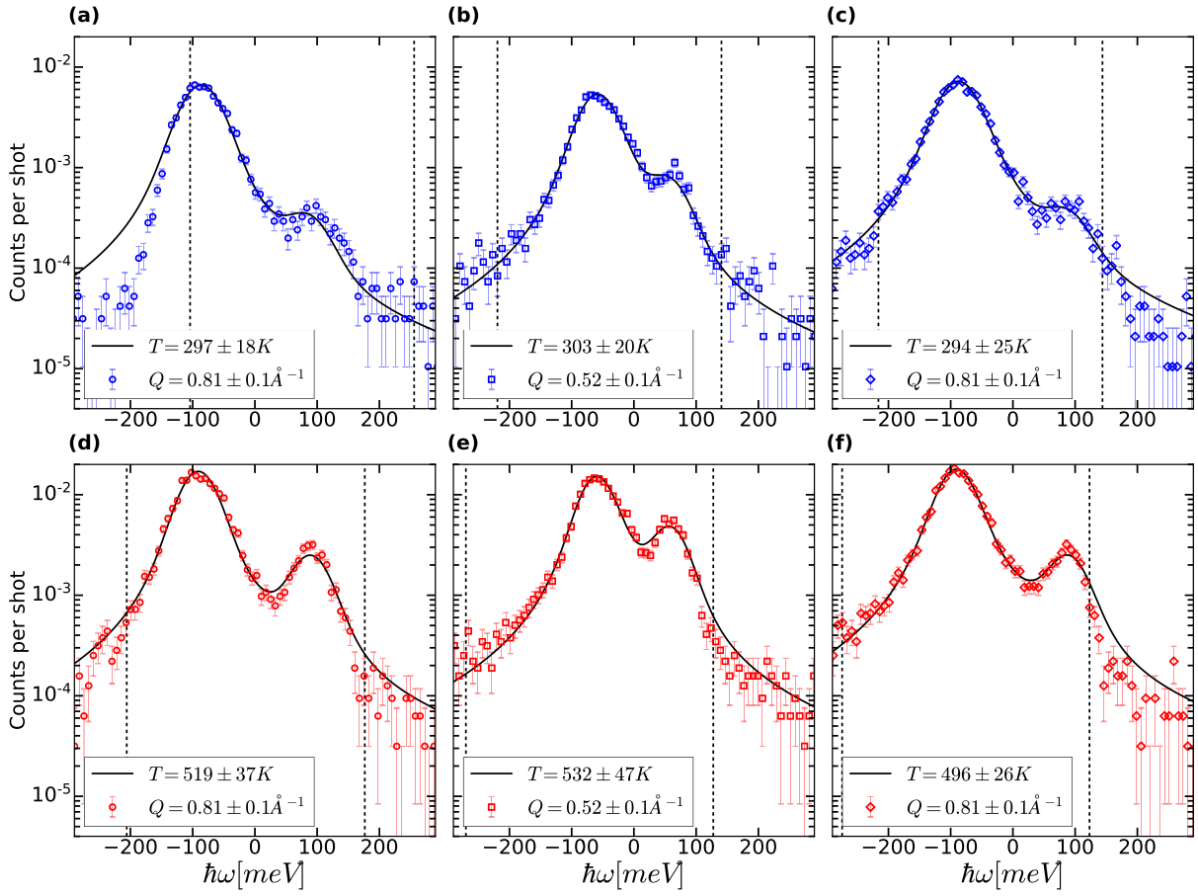

Figure 6.1: Results of p2191 for the monocrystalline diamond at ambient temperature and at 503 ± 8 K, where the approximate photon count is on the order of 10,000 per line out. The instrument function is (74,67,76) meV (ambient), (68,59,64) meV (heated), and the dominant phonons (87,59,87) for (a,b,c). As expected for monocrystalline diamond, no QES contribution can be made out by eye. Figure reproduced with permission from reference [145], Scientific Reports.

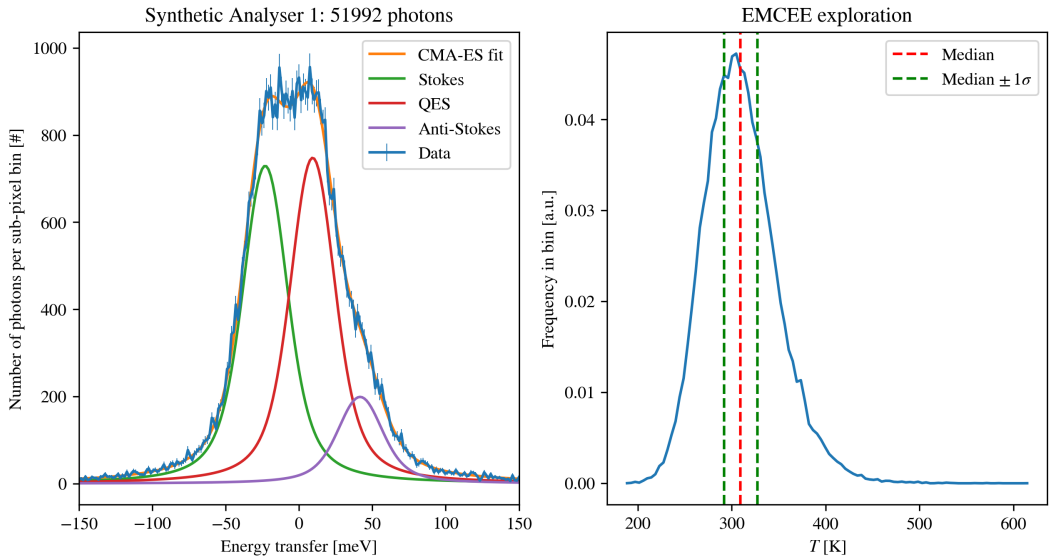

Figure 6.2: On the left, a representative synthetic hr IXS spectrum is plotted. It is generated for a temperature of 298 K, the Ni phonon energy of 33.9 meV (central analyser), a 1:1 ratio of Stokes to QES, an instrument function of 44 meV, and the scaling parameters $a_s = 0.95$, $\omega_s = 10$ meV, $b_s = 1.0$. On the right, the histogram of the accepted results of the EMCEE exploration is plotted, together with the median temperature of $T = 309^{+18}_{-17}$ K. The EMCEE exploration range lies between 1-1000 K.

the metal targets neither temperature nor link between QES and Debye-Scherrer diffraction was determinable, the p2191 and p2656 campaigns provided valuable benchmarks towards how to be successful in these future experiments.

To provide such an estimate of the temperature error for metals, in Figure 6.2 the fit of a synthetic spectrum of Ni with added shot noise is shown. Hereby, a resolution of 44 meV (as achievable at the HED instrument[146]) and the same numbers of photons as recorded for the central Cu analyser of the strongest batch were assumed. For a sample at ambient temperature ($T_0 = 298$ K) and significant QES contribution with the same strength as the Stokes peak, the CMA-ES fits and EMCEE exploration (shown in the same figure) extracted $T = 309^{+18}_{-17}$ K and approximated the equality between the Stokes and QES contribution. Whilst this case is difficult to resolve since the QES contribution equals that of the Stokes peak, and the instrument function of 44 meV remains worse than the peak spacing of about 30 meV for Ni, the errors are on the same order as those for diamond. Apart

from the existence of QES and provided shot noise is kept at a reasonable level (e.g., 50,000 photons for this synthetic spectrum), the setup resolution, or equivalently the phonon energy, make the biggest difference in fit convergence. Since the phonon energy upon compression will increase through pressure hardening, whilst also the cross section will increase with the accompanying higher temperature, the performance of this temperature diagnostic will improve in shock and ramp experiments. Recently, it was demonstrated that the ambient temperature measurement of 286 ± 30 K could be done for crystalline Fe with an instrument function 22 meV, using a higher XFEL energy of 10.9 keV and a (931) monochromator-analyser-setup[214].

Overall, in this experimental configuration and the accompanying challenges, it was hard to resolve both IXS and QES. Given the non-destructive nature of the p2191 and p2656 experiments, it was possible to integrate many XFEL trains at the same sample position to combat shot noise. Future campaigns, that include high-repetition drive lasers in destructive measurements where samples are changed after each train, such as possible with DiPOLE at the EuXFEL, will similarly be able to increase the signal-to-noise ratio, provided it can be ensured that the coordinates of the Thomson scattering source remain the same.

6.3 Concluding Remarks

A temperature measurement based on IXS would answer a much sought-after question in solid HED physics, where a reliable diagnostic currently is lacking. This thesis presented steps of its development not only to cover static experiments or monocrystalline samples but to expand its applicability into the realm of ultrafast shock and ramp compression. It described necessary commissioning work and identified that, whilst here the hr spectra suffered from shot noise and poor instrument resolution, most of the challenges outlined will be overcome with the deployment of new, brighter x-ray sources, paving the way towards making IXS a single shot temperature diagnostic in dynamic experiments.

Appendices

Appendix A

Reciprocal Space of an Ideal fcc Stacking Fault

This section briefly illustrates the signature of a single stacking fault within a perfect fcc crystal. The atomic positions in real space are plotted in Figure A.1, where both the full simulation box and the subset of only hcp atoms can be seen. The stacking fault with a surface normal in [111] was generated by shifting half of the atoms by $[11\bar{2}]/6$.

The result in reciprocal space with the anticipated fcc Bragg spots upon taking the Fourier transform of this faulted crystal is shown in Figure A.2. According to Equation 3.4, only Bragg peaks where $h+k+l$ are not an integer multiple of three are dressed with streaks in [111]. For example, the streaks in $\langle 200 \rangle + q \cdot [111]$ are visible, where $q \in \mathbb{R}$.

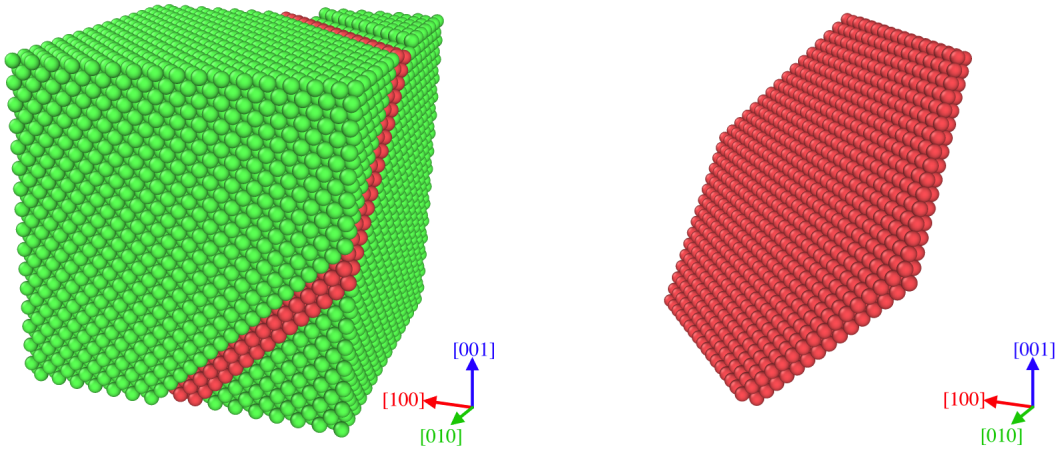

(a) Full simulation box (b) All hcp atoms

Figure A.1: Simulation boxes with atoms highlighted as fcc (green) or hcp (red). A stacking fault along the [111] direction can be seen, classified as hcp.

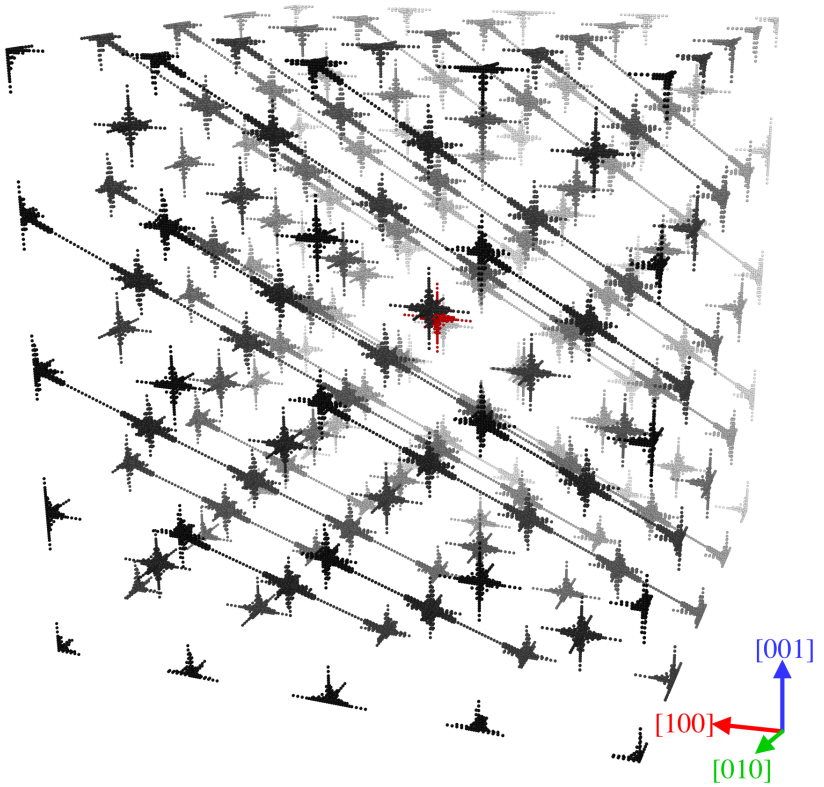

Figure A.2: The 3D Fourier transform of the perfect crystal containing a single stacking fault. The extent of the reciprocal space is defined by the two corners with Miller indices $(\bar{4}, \bar{4}, \bar{4})$ and $(4, 4, 4)$. Again, the colour scale threshold was chosen such that the Bragg peaks are clearly visible whilst the gradient from white to black indicates low to high [010]-coordinate. Intensity situated in the first Brillouin zone is colour coded in red. The fcc Bragg peaks are dressed by sinc-functions along the cardinal directions due to the simulation box. In addition to stacking-fault-related diagonal streaks in [111] can be seen for Bragg peaks whose $h+k+l$ are not an integer multiple of three.

Appendix B

Average Detector Image of the Diffraction Diagnostic

In Figures B.1 and B.2, the normalised average images seen on the Jungfrau detector in p2656 are shown for each of the six batches of equivalent experimental configuration. The white vertical and horizontal stripes are masked edge pixels and the gap between the diffraction detectors. Furthermore, the rectangular white areas in the top and bottom chips on the very right, and the broad horizontal bar across, are masked cold/hot pixels. In addition to the two diffraction lines, batch-dependent scatter signal can be seen on the chip.

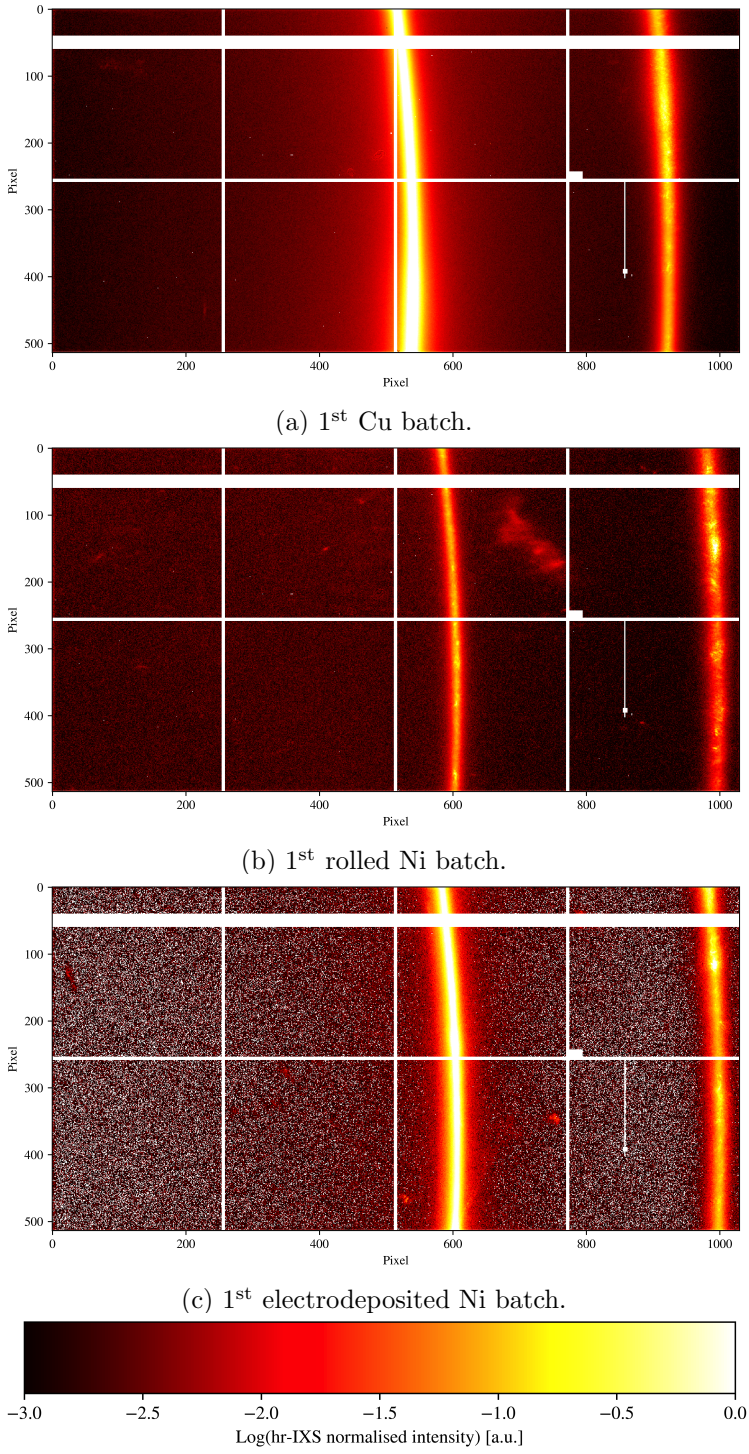

(a) 1st Cu batch.

(b) 1st rolled Ni batch.

(c) 1st electrodeposited Ni batch.

Figure B.1: Normalised average detector image for the samples shot at p2656 (1st set of experimentally equivalent positions). From left to right, the $\{1, 1, 1\}$ and $\{2, 0, 0\}$ fcc Debye-Scherrer ring sections can be seen.

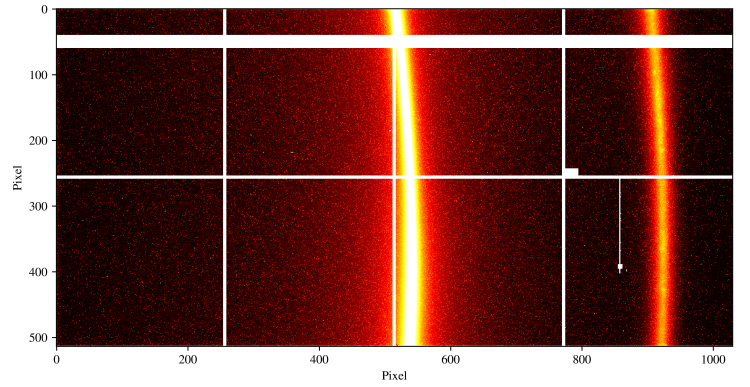

(a) 2nd Cu batch.

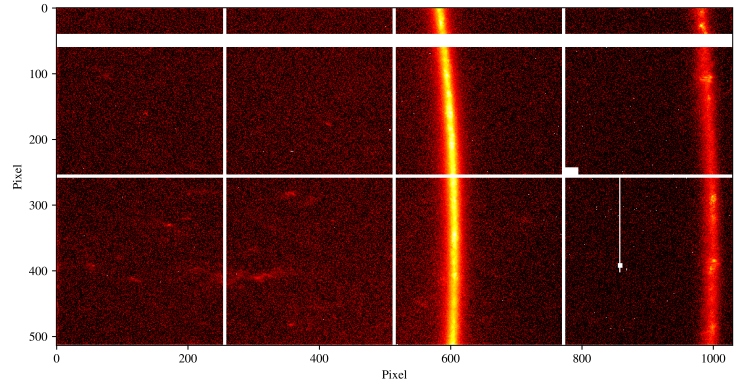

(b) 2nd rolled Ni batch.

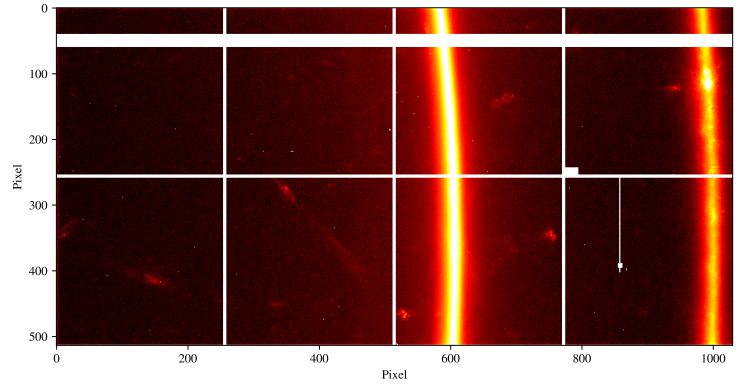

(c) 2nd electrodeposited Ni batch.

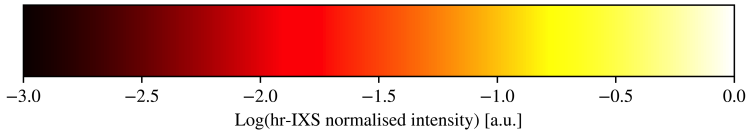

Figure B.2: Normalised average detector image for the samples shot at p2656 (2nd set of experimentally equivalent positions). From left to right, the $\{1, 1, 1\}$ and $\{2, 0, 0\}$ fcc Debye-Scherrer ring sections can be seen.

Appendix C

Average Detector Image of the HAPG Diagnostic

In Figure C.1, the mean image of PMMA with 8953 trains of the HAPG spectrometer can be seen. The Jungfrau detector consists of eight tiles that are fit together with a pixel gap between (visible around the horizontal pixel coordinate of 800). The top section of the detector contains a damaged tile (saturated white signal). On the bottom half, a horizontal line out across four tiles can be found. The elastic XRTS signal is positioned at the right detector edge and farther left, towards lower energies, a broad Compton feature can be seen. The HAPG focuses the XRTS signal along this narrow stripe and to obtain a spectrum, a few pixels centred at about the vertical pixel coordinate of 420 are summed to increase the signal strength.

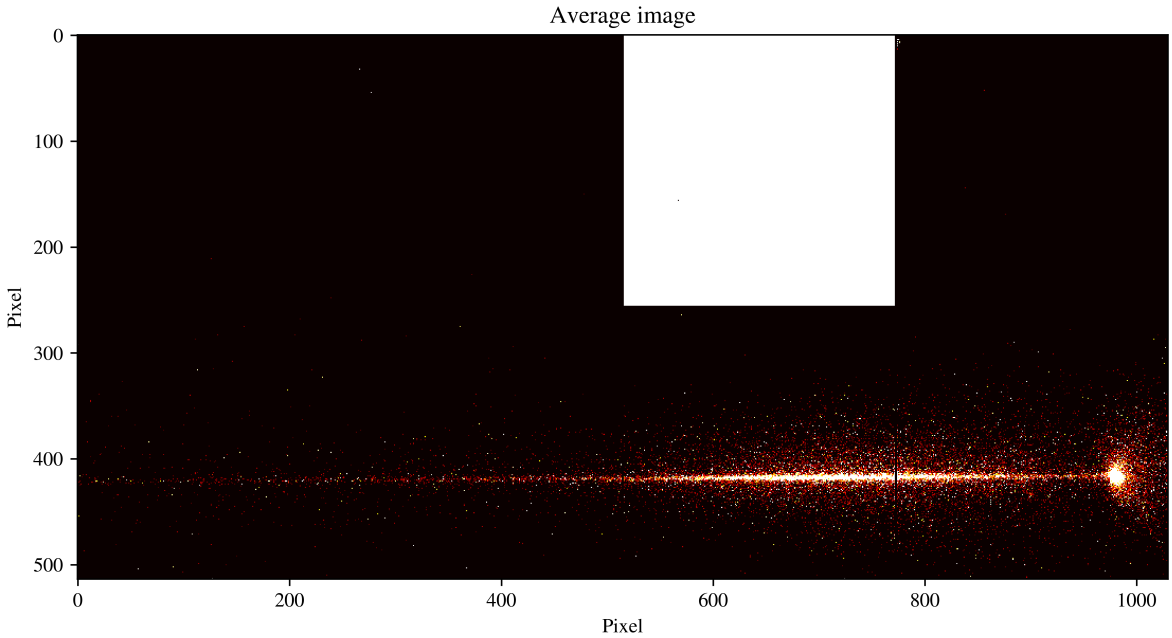

Figure C.1: Average Jungfrau image of the HAPG detector for all p2656 PMMA runs of equivalent experimental configuration. The upper section of the detector chip is damaged. In the lower section, the line out can be seen, where the main direction of dispersion is the horizontal (low energies on the left, high energies on the right).

Appendix D

Additional p2656 Polycrystal Spectra

In Figure D.1, the other nine spectra of p2656 from the polycrystalline metal foils of equivalent experimental configuration at 21° per element are presented for each DCA. In Section 5.2.4, Figure 5.10 other batches of copper (Cu), electrodeposited nickel (Ni(e)), and rolled nickel (Ni(r)) are shown. The error bars are found through Equation 5.1. The signal still is more intense than it was for any line out in p2191.

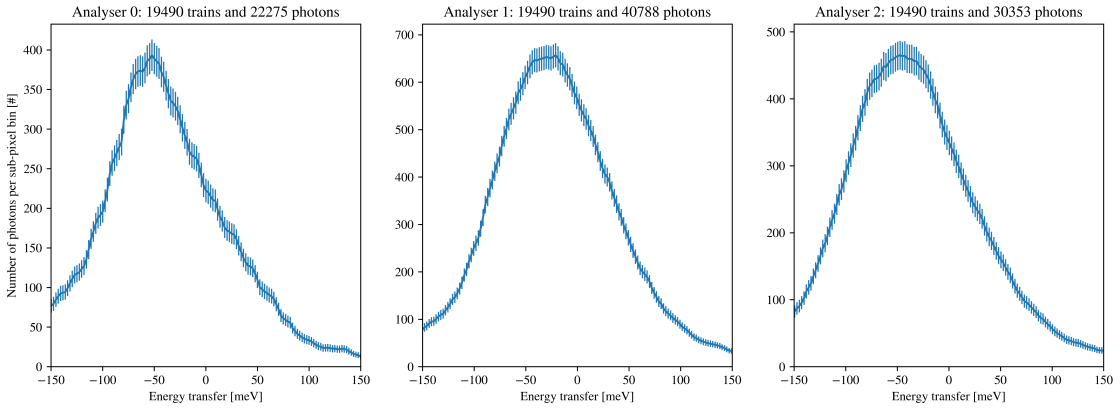

(a) 1st Cu batch.

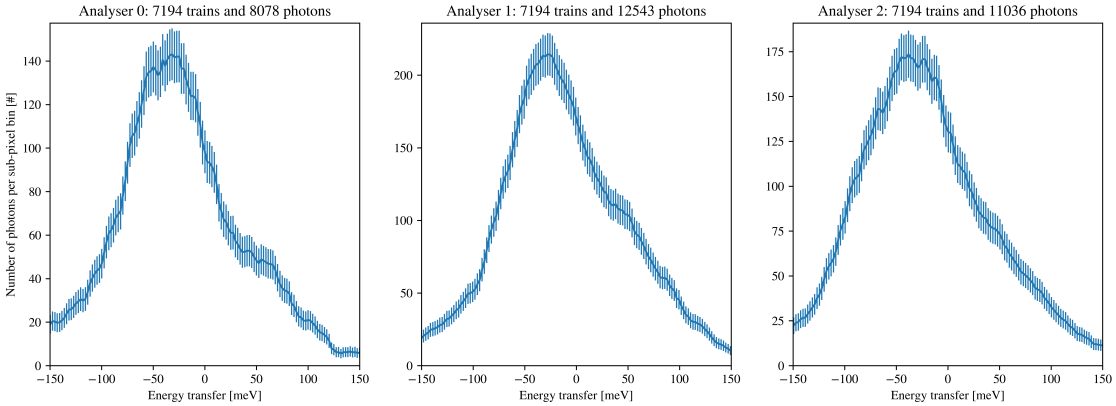

(b) 1st rolled Ni batch.

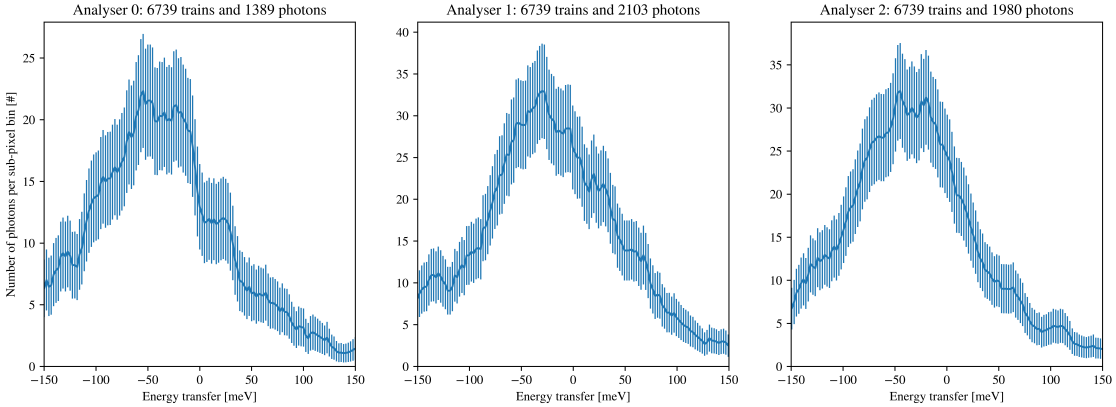

(c) 2nd electrodeposited Ni batch.

Figure D.1: Weaker batches of p2656 hr IXS spectra at 21°. The unwarped data with error bars are plotted for each DCA, where the energy zero is in reference to the PMMA calibration. Again, even for the wide instrument function, some asymmetry can be seen.

Appendix E

Additional p2656 EMCEE Parameter Explorations

In Figures E.1, E.2, E.3, and 5.16, the EMCEE parameter explorations for the other spectra of p2656 are presented, which have not been displayed in Section 5.3. Apart from the first Ni batch, the distributions are narrow and contain the best CMA-ES fit results.

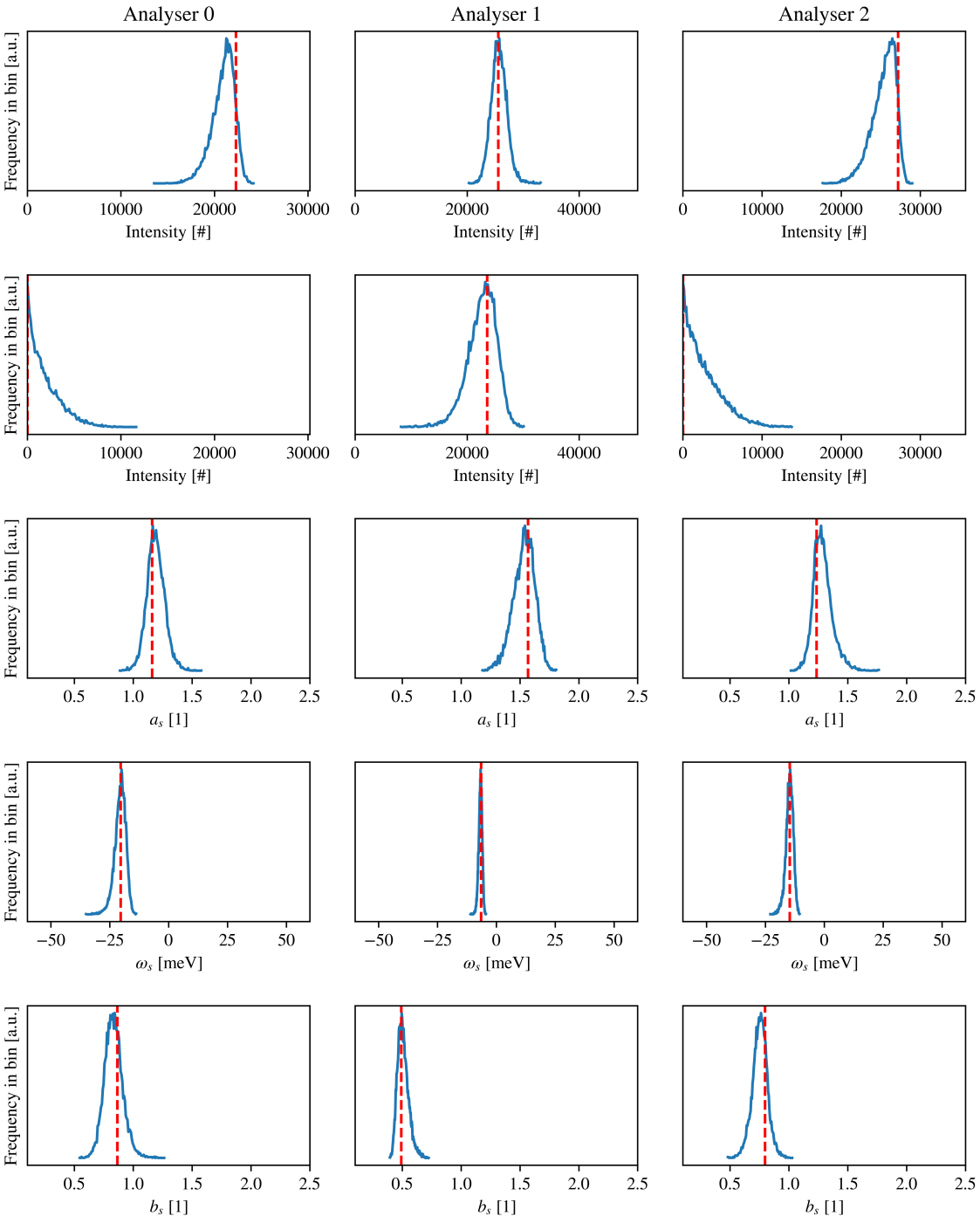

Figure E.1: CMA-ES parameter sensitivity obtained through EMCEE exploration for the second Cu batch with about 50,000 EMCEE samples per analyser. The best fits are indicated by dashed orange lines and narrow distributions around these are found.

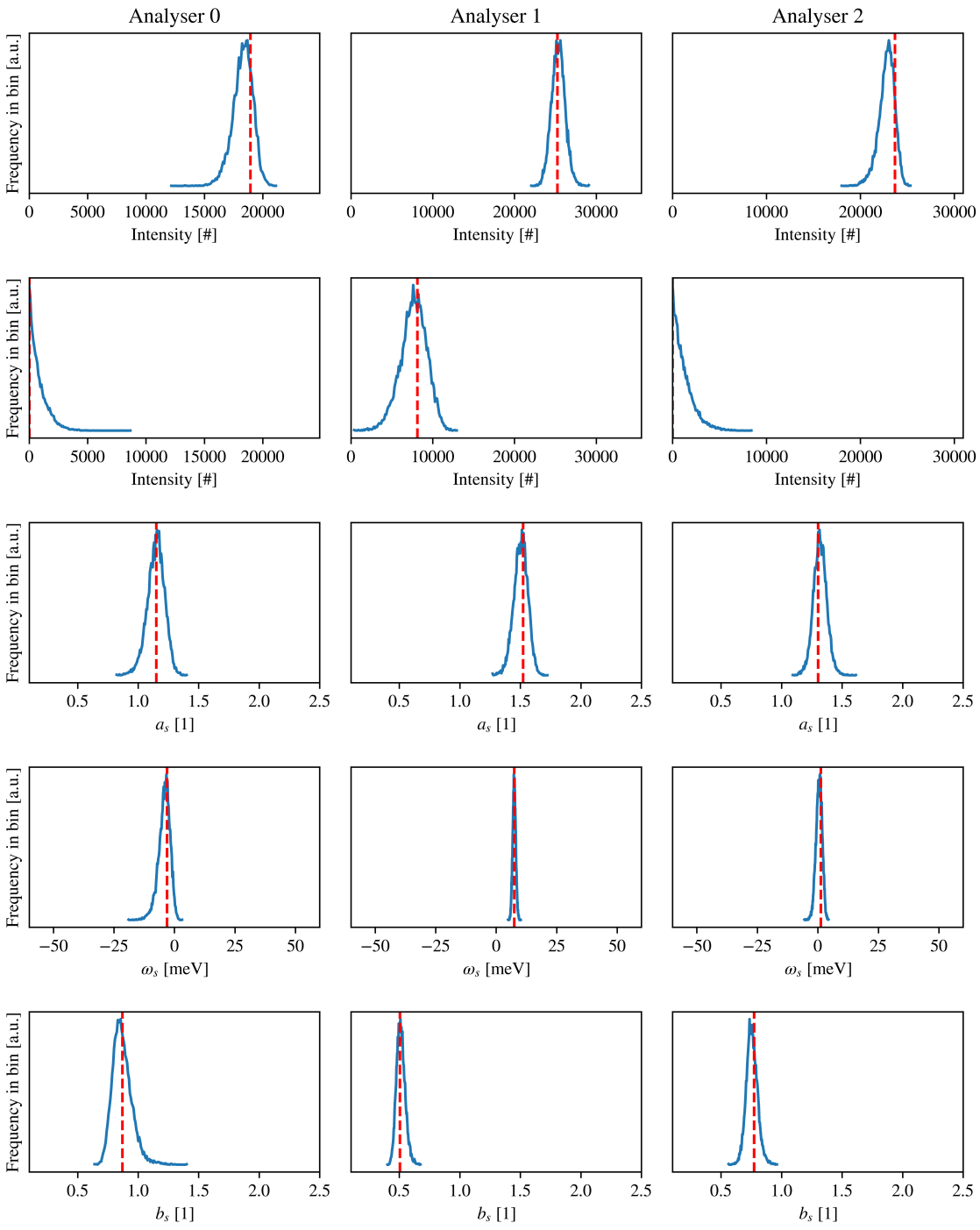

Figure E.2: CMA-ES parameter sensitivity obtained through EMCEE exploration for the first rolled Ni batch with about 50,000 EMCEE samples per analyser. The best fits are indicated by dashed orange lines and narrow distributions around these are found.

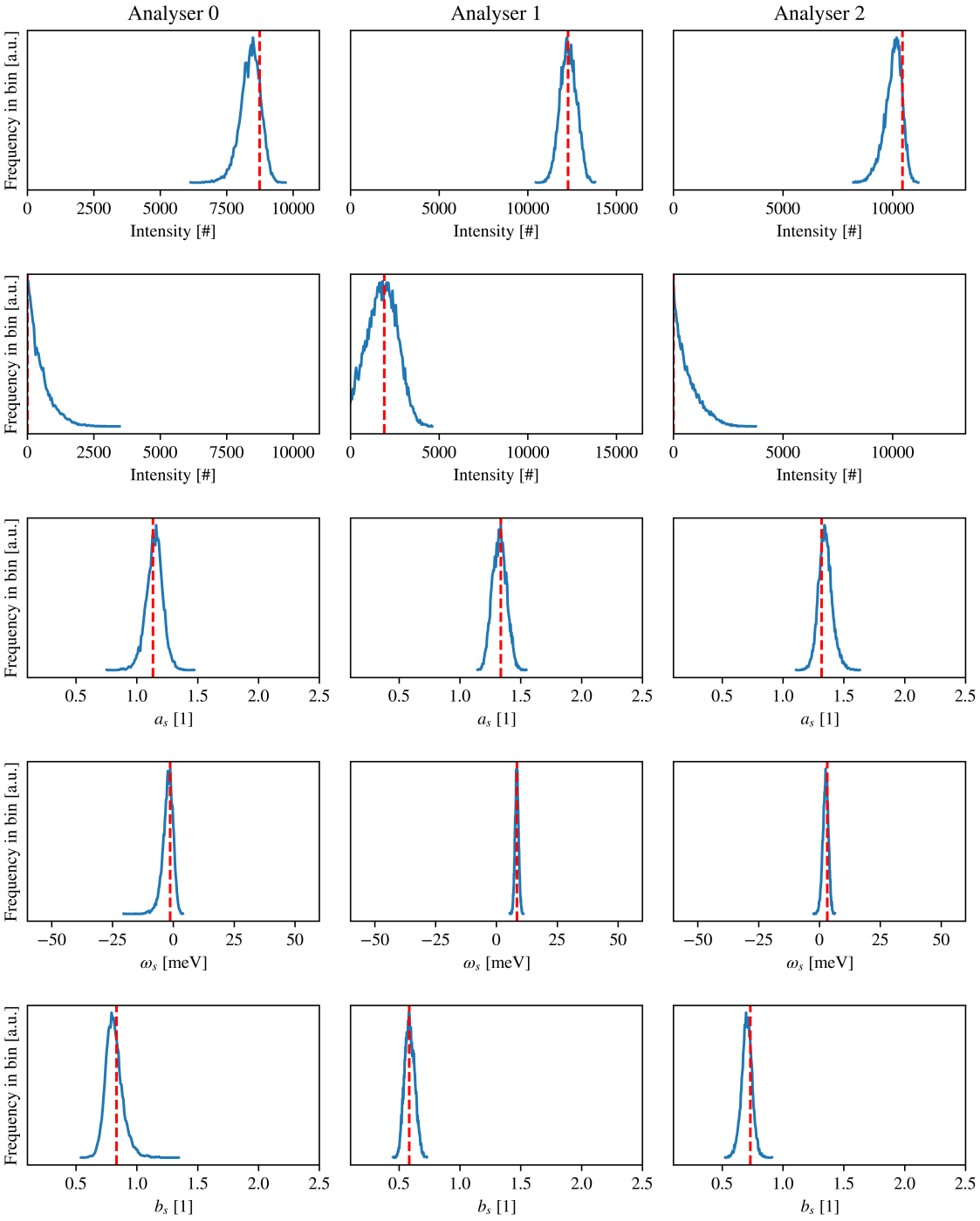

Figure E.3: CMA-ES parameter sensitivity obtained through EMCEE exploration for the second rolled Ni batch with about 50,000 EMCEE samples per analyser. The best fits are indicated by dashed orange lines and narrow distributions around these are found. The uncertainty is the largest for the central DCA.

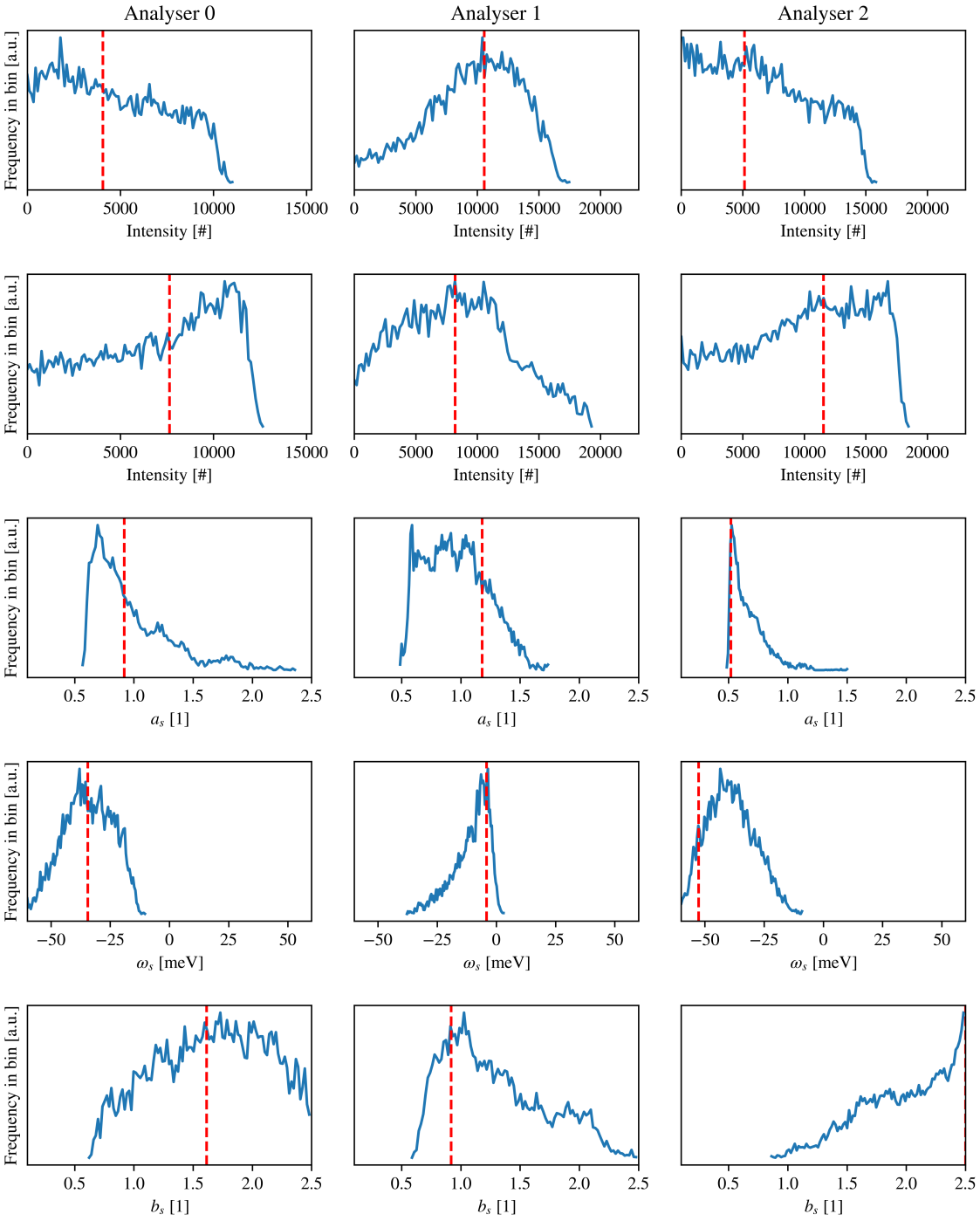

Figure E.4: CMA-ES parameter sensitivity obtained through EMCEE exploration for the first electrodeposited Ni batch with about 50,000 EMCEE samples per analyser. The best fits are indicated by dashed orange lines. As for the first Ni(e) batch, the fit cost is largely insensitive to significant parameter variation and no reliable convergence could be found.

References

[1] P. W. Bridgman. "Water, in the Liquid and Five Solid Forms, under Pressure". *Proceedings of the American Academy of Arts and Sciences*, 47(13):441, 1912. doi: 10.2307/20022754.

[2] P. W. Bridgman. "Change of Phase under Pressure. I. The Phase Diagram of Eleven Substances with Especial Reference to The Melting Curve". *Physical Review*, 3(3): 153–203, 1914. doi: 10.1103/PhysRev.3.153.

[3] P. W. Bridgman. "The Compressibility of Thirty Metals as a Function of Pressure and Temperature". *Proceedings of the American Academy of Arts and Sciences*, 58(5):165, 1923. doi: 10.2307/20025987.

[4] F. P. Bundy, H. T. Hall, H. M. Strong, and R. H. Wentorfjun. "Man-Made Diamonds". *Nature*, 176(4471):51–55, 1955. doi: 10.1038/176051a0.

[5] J. M. Walsh and R. H. Christian. "Equation of state of metals from shock wave measurements". *Physical Review*, 97:1544–1556, 1955. doi: 10.1103/PhysRev.97.1544.

[6] D. Bancroft, E. L. Peterson, and S. Minshall. "Polymorphism of iron at high pressure". *Journal of Applied Physics*, 27(3):291–298, 1956. doi: 10.1063/1.1722359.

[7] F. P. Bundy, H. P. Bovenkerk, H. M. Strong, and R. H. Wentorf. "Diamond-Graphite Equilibrium Line from Growth and Graphitization of Diamond". *The Journal of Chemical Physics*, 35(2):383–391, 1961. doi: 10.1063/1.1731938.

[8] S. Minomura and H. Drickamer. "Pressure induced phase transitions in silicon, germanium and some III–V compounds". *Journal of Physics and Chemistry of Solids*, 23 (5):451–456, 1962. doi: 10.1016/0022-3697(62)90085-9.

[9] R. W. Lynch and H. G. Drickamer. "Effect of High Pressure on the Lattice Parameters of Diamond, Graphite, and Hexagonal Boron Nitride". *The Journal of Chemical Physics*, 44(1):181–184, 1966. doi: 10.1063/1.1726442.

[10] C. P. Slichter and H. G. Drickamer. "Pressure-Induced Electronic Changes in Compounds of Iron". *The Journal of Chemical Physics*, 56(5):2142–2160, 1972. doi: 10.1063/1.1677511.

[11] F. P. Bundy. "The P , T phase and reaction diagram for elemental carbon, 1979". *Journal of Geophysical Research*, 85(B12):6930, 1980. doi: 10.1029/JB085iB12p06930.

[12] D. Keefe. "Inertial Confinement Fusion". *Annual Review of Nuclear and Particle Science*, 32(1):391–441, 1982. doi: 10.1146/annurev.ns.32.120182.002135.

[13] R. Betti and O. A. Hurricane. "Inertial-confinement fusion with lasers". *Nature Physics*, 12(5):435–448, 2016. doi: 10.1038/nphys3736.

[14] P. W. Bridgman. "High Pressure Polymorphism of Iron". *Journal of Applied Physics*, 27(6):659–659, 1956. doi: 10.1063/1.1722456.

[15] T. Guillot. "Interiors of Giant Planets Inside and Outside the Solar System". *Science*, 286(5437):72–77, 1999. doi: 10.1126/science.286.5437.72.

[16] S. Seager, M. Kuchner, C. A. Hier-Majumder, and B. Militzer. "Mass-radius relationships for solid exoplanets". *The Astrophysical Journal*, 669(2):1279–1297, 2007. doi: 10.1086/521346.

[17] D. Valencia, R. J. O'Connell, and D. D. Sasselov. "The role of high-pressure experiments on determining super-earth properties". *Astrophysics and Space Science*, 322: 135–139, 2009. doi: 10.1007/s10509-009-0034-6.

[18] S. Tateno, K. Hirose, Y. Ohishi, and Y. Tatsumi. "The Structure of Iron in Earth's Inner Core". *Science*, 330(6002):359–361, 2010. doi: 10.1126/science.1194662.

[19] D. C. Swift, J. H. Eggert, D. G. Hicks, S. Hamel, K. Caspersen, E. Schwegler, G. W. Collins, N. Nettelmann, and G. J. Ackland. "Mass-Radius Relationships for Exoplanets". *The Astrophysical Journal*, 744(1):59, 2011. doi: 10.1088/0004-637x/744/1/59.

[20] J. Wentorf, R. H. and J. S. Kasper. "Two New Forms of Silicon". *Science*, 139(3552): 338–339, 1963. doi: 10.1126/science.139.3552.338-a.

[21] J. Sun, D. D. Klug, and R. Martoňák. "Structural transformations in carbon under extreme pressure: Beyond diamond". *The Journal of Chemical Physics*, 130(19):194512, 2009. doi: 10.1063/1.3139060.

[22] E. K. Cerreta, F. L. Addessio, C. A. Bronkhorst, D. W. Brown, J. P. Escobedo, S. J. Fensin, G. T. Gray, T. Lookman, P. A. Rigg, and C. P. Trujillo. "The influence of peak shock stress on the high pressure phase transformation in zr". *Journal of Physics: Conference Series*, 500(3):032003, 2014. doi: 10.1088/1742-6596/500/3/032003.

[23] S. M. Clarke, J. P. S. Walsh, M. Amsler, C. D. Malliakas, T. Yu, S. Goedecker, Y. Wang, C. Wolverton, and D. E. Freedman. "Discovery of a superconducting cu–bi intermetallic compound by high-pressure synthesis". *Angewandte Chemie International Edition*, 55(43):13446–13449, 2016. doi: 10.1002/anie.201605902.

[24] M. G. Gorman, D. McGonegle, S. J. Tracy, S. M. Clarke, C. A. Bolme, A. E. Gleason, S. J. Ali, S. Hok, C. W. Greeff, P. G. Heighway, K. Hulpach, B. Glam, E. Galtier, H. J. Lee, J. S. Wark, J. H. Eggert, J. K. Wicks, and R. F. Smith. "Recovery of a high-pressure phase formed under laser-driven compression". *Phys. Rev. B*, 102: 024101, 2020. doi: 10.1103/PhysRevB.102.024101.

[25] R. B. Jacobs. "X-ray diffraction of substances under high pressures". *Phys. Rev.*, 54: 325–331, 1938. doi: 10.1103/PhysRev.54.325.

[26] R. B. Jacobs. "Polymorphic transitions in metallic halides". *Phys. Rev.*, 54:468–474, 1938. doi: 10.1103/PhysRev.54.468.

[27] J. C. Jamieson, A. W. Lawson, and N. D. Nachtrieb. "New device for obtaining x-ray diffraction patterns from substances exposed to high pressure". *Review of Scientific Instruments*, 30(11):1016–1019, 1959. doi: 10.1063/1.1716408.

[28] Q. Johnson, A. Mitchell, R. N. Keeler, and L. Evans. "X-ray diffraction during shock-wave compression". *Phys. Rev. Lett.*, 25:1099–1101, 1970. doi: 10.1103/PhysRevLett.25.1099.

[29] Q. Johnson, A. Mitchell, and L. Evans. "X-ray Diffraction Evidence for Crystalline Order and Isotropic Compression during the Shock-wave Process". *Nature*, 231(5301):310–311, 1971. doi: 10.1038/231310b0.

[30] E. Burkel. "Phonon spectroscopy by inelastic x-ray scattering". *Reports on Progress in Physics*, 63(2):171–232, 2000. doi: 10.1088/0034-4885/63/2/203.

[31] S. K. Sinha. "Theory of inelastic x-ray scattering from condensed matter". *Journal of Physics: Condensed Matter*, 13(34):7511–7523, 2001. doi: 10.1088/0953-8984/13/34/304.

[32] H. Sinn. "Spectroscopy with meV energy resolution". *Journal of Physics: Condensed Matter*, 13(34):7525–7537, 2001. doi: 10.1088/0953-8984/13/34/305.

[33] M. D'Astuto, P. Giura, M. Krisch, M. Lorenzen, A. Mermet, G. Monaco, H. Requardt, F. Sette, A. Shukla, and R. Verbeni. "Phonon dispersion studies of crystalline materials using high-energy resolution inelastic X-ray scattering (IXS)". *Physica B: Condensed Matter*, 316-317:150–153, 2002. doi: 10.1016/S0921-4526(02)00445-3.

[34] A. Q. Baron. "Phonons in crystals using inelastic x-ray scattering". *Journal of The Spectroscopical Society of Japan*, 58(5):205, 2009.

[35] V. W. Yuan, J. D. Bowman, D. J. Funk, G. L. Morgan, R. L. Rabie, C. E. Ragan, J. P. Quintana, and H. L. Stacy. "Shock Temperature Measurement Using Neutron Resonance Spectroscopy". *Physical Review Letters*, 94(12):125504, 2005. doi: 10.1103/PhysRevLett.94.125504.

[36] A. Q. Baron. *High-Resolution Inelastic X-Ray Scattering I: Context, Spectrometers, Samples, and Superconductors*, volume 1. Springer International Publishing, 2016.

[37] B. N. Brockhouse and A. T. Stewart. "Scattering of Neutrons by Phonons in an Aluminum Single Crystal". *Physical Review*, 100(2):756–757, 1955. doi: 10.1103/PhysRev.100.756.

[38] R. J. Birgeneau, J. Cordes, G. Dolling, and A. D. B. Woods. "Normal Modes of Vibration in Nickel". *Physical Review*, 136(5A):A1359–A1365, 1964. doi: 10.1103/PhysRev.136.A1359.

[39] J. L. Warren, J. L. Yarnell, G. Dolling, and R. A. Cowley. "Lattice Dynamics of Diamond". *Physical Review*, 158(3):805–808, 1967. doi: 10.1103/PhysRev.158.805.

[40] M. A. Coulthard. "Pressure dependence of phonon dispersion curves in simple metals". *Journal of Physics C: Solid State Physics*, 3(4):820–834, 1970. doi: 10.1088/0022-3719/3/4/010.

[41] W. M. Shaw and L. D. Muhlestein. "Investigation of the Phonon Dispersion Relations of Chromium by Inelastic Neutron Scattering". *Physical Review B*, 4(3):969–973, 1971. doi: 10.1103/PhysRevB.4.969.

[42] F. Sette. "Dynamics of Glasses and Glass-Forming Liquids Studied by Inelastic X-ray Scattering". *Science*, 280(5369):1550–1555, 1998. doi: 10.1126/science.280.5369.1550.

[43] F. Occelli, M. Krisch, P. Loubeyre, F. Sette, R. Le Toullec, R. Le Toullec, C. Masciovecchio, and J. P. Rueff. "Phonon dispersion curves in an argon single crystal at high pressure by inelastic x-ray scattering". *Physical Review B - Condensed Matter and Materials Physics*, 63(22):2243061–2243068, 2001. doi: 10.1103/PhysRevB.63.224306.

[44] G. Shen, W. Sturhahn, E. E. Alph, J. Zhao, T. S. Toellnner, V. B. Prakapenka, Y. Meng, and H. R. Mao. "Phonon density of states in iron at high pressures and high temperatures". *Physics and Chemistry of Minerals*, 31(6):353–359, 2004. doi: 10.1007/s00269-004-0403-l.

[45] J. Zhao, W. Sturhahn, J.-f. Lin, G. Shen, E. E. Alp, and H.-k. Mao. "Nuclear resonant scattering at high pressure and high temperature". *High Pressure Research*, 24(4):447–457, 2004. doi: 10.1080/08957950412331331727.

[46] R. Mittal, R. Heid, A. Bosak, T. R. Forrest, S. L. Chaplot, D. Lamago, D. Reznik, K.-P. Bohnen, Y. Su, N. Kumar, S. K. Dhar, A. Thamizhavel, C. Rüegg, M. Krisch, D. F. McMorrow, T. Brueckel, and L. Pintschovius. "Pressure dependence of phonon modes across the tetragonal to collapsed-tetragonal phase transition in CaFe2As2". *Physical Review B*, 81(14):144502, 2010. doi: 10.1103/PhysRevB.81.144502.

[47] D. Srivastava, U. V. Waghmare, and S. K. Sarkar. "Evidence of scaling in the high pressure phonon dispersion relations of some elemental solids". *The Journal of Chemical Physics*, 141(4):044714, 2014. doi: 10.1063/1.4890998.

[48] R. Mittal, M. K. Gupta, B. Singh, L. Pintschovius, Y. D. Zavartsev, and S. L. Chaplot. "Phonon dispersion relation, high-pressure phase stability, and thermal expansion in YVO4". *Physical Review Materials*, 3(4):043608, 2019. doi: 10.1103/PhysRevMaterials.3.043608.

[49] A. L. Ruoff, H. Xia, H. Luo, and Y. K. Vohra. "Miniaturization techniques for obtaining static pressures comparable to the pressure at the center of the earth: X-ray diffraction at 416 GPa". *Review of Scientific Instruments*, 61(12):3830–3833, 1990. doi: 10.1063/1.1141509.

[50] R. J. Hemley. "X-ray Imaging of Stress and Strain of Diamond, Iron, and Tungsten at Megabar Pressures". *Science*, 276(5316):1242–1245, 1997. doi: 10.1126/science.276.5316.1242.

[51] Y. Ma, V. I. Levitas, and J. Hashemi. "X-ray diffraction measurements in a rotational diamond anvil cell". *Journal of Physics and Chemistry of Solids*, 67(9-10):2083–2090, 2006. doi: 10.1016/j.jpcs.2006.05.052.

[52] I. Loa, R. J. Nelmes, L. F. Lundegaard, and M. I. McMahon. "Extraordinarily complex crystal structure with mesoscopic patterning in barium at high pressure". *Nature Materials*, 11(7):627–632, 2012. doi: 10.1038/nmat3342.

[53] L. Dubrovinsky, N. Dubrovinskaia, V. B. Prakapenka, and A. M. Abakumov. "Implementation of micro-ball nanodiamond anvils for high-pressure studies above 6 Mbar". *Nature Communications*, 3(1):1163, 2012. doi: 10.1038/ncomms2160.

[54] G. Shen and H. K. Mao. "High-pressure studies with x-rays using diamond anvil cells". *Reports on Progress in Physics*, 80(1):016101, 2017. doi: 10.1088/1361-6633/80/1/016101.

[55] S. Petitgirard, J. Jacobs, V. Cerantola, I. E. Collings, R. Tucoulou, L. Dubrovinsky, and C. J. Sahle. "A versatile diamond anvil cell for X-ray inelastic, diffraction and imaging studies at synchrotron facilities". *Review of Scientific Instruments*, 90(9), 2019. doi: 10.1063/1.5119025.

[56] L. V. Al'tshuler, M. N. Pavlovskii, and V. P. Drakin. "Peculiarities of Phase Transitions in Compression and Rarefaction Shock Waves". *J. Exptl. Theoret. Phys. (U.S.S.R.)*, 25(2):400–408, 1967.

[57] Q. Johnson, A. C. Mitchell, and L. Evans. "X-ray diffraction study of single crystals undergoing shock-wave compression". *Applied Physics Letters*, 21(1):29–30, 1972. doi: 10.1063/1.1654205.

[58] Q. Johnson and A. C. Mitchell. "First X-Ray Diffraction Evidence for a Phase Transition during Shock-Wave Compression". *Physical Review Letters*, 29(20):1369–1371, 1972. doi: 10.1103/PhysRevLett.29.1369.

[59] A. H. Jones, W. M. Isbell, and C. J. Maiden. "Measurement of the very-high-pressure properties of materials using a light-gas gun". *Journal of Applied Physics*, 37(9):3493–3499, 1966. doi: 10.1063/1.1708887.

[60] J. S. Wark, R. R. Whitlock, A. A. Hauer, J. E. Swain, and P. J. Solone. "Subnanosecond x-ray diffraction from laser-shocked crystals". *Physical Review B*, 40(8):5705–5714, 1989. doi: 10.1103/PhysRevB.40.5705.

[61] M. M. Murnane, H. C. Kapteyn, M. D. Rosen, and R. W. Falcone. "Ultrafast X-ray Pulses from Laser-Produced Plasmas". *Science*, 251(4993):531–536, 1991. doi: 10.1126/science.251.4993.531.

[62] A. Loveridge-Smith, A. Allen, J. Belak, T. Boehly, A. Hauer, B. Holian, D. Kalantar, G. Kyrala, R. W. Lee, P. Lomdahl, M. A. Meyers, D. Paisley, S. Pollaine, B. Remington, D. C. Swift, S. Weber, and J. S. Wark. "Anomalous Elastic Response of Silicon to Uniaxial Shock Compression on Nanosecond Time Scales". *Physical Review Letters*, 86(11):2349–2352, 2001. doi: 10.1103/PhysRevLett.86.2349.

[63] D. H. Kalantar, J. F. Belak, G. W. Collins, J. D. Colvin, H. M. Davies, J. H. Eggert, T. C. Germann, J. Hawreliak, B. L. Holian, K. Kadau, P. S. Lomdahl, H. E. Lorenzana, M. A. Meyers, K. Rosolankova, M. S. Schneider, J. Sheppard, J. S. Stölken, and J. S. Wark. "Direct observation of the α-ϵ transition in shock-compressed iron via nanosecond x-ray diffraction". *Physical Review Letters*, 95:075502, 2005. doi: 10.1103/PhysRevLett.95.075502.

[64] J. Hawreliak, J. D. Colvin, J. H. Eggert, D. H. Kalantar, H. E. Lorenzana, J. S. Stölken, H. M. Davies, T. C. Germann, B. L. Holian, K. Kadau, P. S. Lomdahl, A. Higginbotham, K. Rosolankova, J. Sheppard, and J. S. Wark. "Analysis of the x-ray diffraction signal for the α-ε transition in shock-compressed iron: Simulation and experiment". *Phys. Rev. B*, 74:184107, 2006. doi: 10.1103/PhysRevB.74.184107.

[65] M. D. Knudson, M. P. Desjarlais, and D. H. Dolan. "Shock-Wave Exploration of the High-Pressure Phases of Carbon". *Science*, 322(5909):1822–1825, 2008. doi: 10.1126/science.1165278.

[66] W. J. Murphy, A. Higginbotham, G. Kimminau, B. Barbrel, E. M. Bringa, J. Hawreliak, R. Kodama, M. Koenig, W. McBarron, M. A. Meyers, B. Nagler, N. Ozaki, N. Park, B. Remington, S. Rothman, S. M. Vinko, T. Whitcher, and J. S. Wark. "The strength of single crystal copper under uniaxial shock compression at 100 GPa". *Journal of Physics: Condensed Matter*, 22(6):065404, 2010. doi: 10.1088/0953-8984/22/6/065404.

[67] D. Milathianaki, D. C. Swift, J. Hawreliak, B. S. El-Dasher, J. M. McNaney, H. E. Lorenzana, and T. Ditmire. "In situ lattice measurement of the bcc phase boundary in Mg on the principal shock Hugoniot". *Physical Review B*, 86(1):014101, 2012. doi: 10.1103/PhysRevB.86.014101.

[68] M. Suggit, A. Higginbotham, G. Mogni, G. Kimminau, P. Dunne, A. Comley, N. Park, B. Remington, and J. Wark. "Nanosecond white-light laue diffraction measurements of dislocation microstructure in shock-compressed single-crystal copper". *Nature communications*, 3:1224, 2012. doi: 10.1038/ncomms2225.

[69] A. J. Comley, B. R. Maddox, R. E. Rudd, S. T. Prisbrey, J. A. Hawreliak, D. A. Orlikowski, S. C. Peterson, J. H. Satcher, A. J. Elsholz, H. S. Park, B. A. Remington, N. Bazin, J. M. Foster, P. Graham, N. Park, P. A. Rosen, S. R. Rothman, A. Higginbotham, M. Suggit, and J. S. Wark. "Strength of Shock-Loaded Single-Crystal Tantalum [100] Determined using In Situ Broadband X-Ray Laue Diffraction". *Physical Review Letters*, 110:115501, 2013. doi: 10.1103/PhysRevLett.110.115501.

[70] D. Milathianaki, S. Boutet, G. J. Williams, A. Higginbotham, D. Ratner, A. E. Gleason, M. Messerschmidt, M. M. Seibert, D. C. Swift, P. Hering, J. Robinson, W. E. White, and J. S. Wark. "Femtosecond visualization of lattice dynamics in shock-compressed matter". *Science*, 342(6155):220–223, 2013. doi: 10.1126/science.1239566.

[71] C. E. Wehrenberg, A. J. Comley, N. R. Barton, F. Coppari, D. Fratanduono, C. M. Huntington, B. R. Maddox, H. S. Park, C. Plechaty, S. T. Prisbrey, B. A. Remington, and R. E. Rudd. "Lattice-level observation of the elastic-to-plastic relaxation process with subnanosecond resolution in shock-compressed Ta using time-resolved in situ Laue diffraction". *Physical Review B*, 92(10):104305, 2015. doi: 10.1103/PhysRevB.92.104305.

[72] A. Schropp, R. Hoppe, V. Meier, J. Patommel, F. Seiboth, Y. Ping, D. G. Hicks, M. A. Beckwith, G. W. Collins, A. Higginbotham, J. S. Wark, H. J. Lee, B. Nagler, E. C. Galtier, B. Arnold, U. Zastrau, J. B. Hastings, and C. G. Schroer. "Imaging Shock Waves in Diamond with Both High Temporal and Spatial Resolution at an XFEL". *Scientific Reports*, 5(1):11089, 2015. doi: 10.1038/srep11089.

[73] A. E. Gleason, C. A. Bolme, H. J. Lee, B. Nagler, E. Galtier, D. Milathianaki, J. Hawreliak, R. G. Kraus, J. H. Eggert, D. E. Fratanduono, G. W. Collins, R. Sandberg, W. Yang, and W. L. Mao. "Ultrafast visualization of crystallization and grain growth in shock-compressed SiO2". *Nature Communications*, 6(1):8191, 2015. doi: 10.1038/ncomms9191.

[74] U. Zastrau, E. J. Gamboa, D. Kraus, J. F. Benage, R. P. Drake, P. Efthimion, K. Falk, R. W. Falcone, L. B. Fletcher, E. Galtier, M. Gauthier, E. Granados, J. B. Hastings, P. Heimann, K. Hill, P. A. Keiter, J. Lu, M. J. MacDonald, D. S. Montgomery, B. Nagler, N. Pablant, A. Schropp, B. Tobias, D. O. Gericke, S. H. Glenzer, and H. J. Lee. "Tracking the density evolution in counter-propagating shock waves using imaging X-ray scattering". *Applied Physics Letters*, 109(3):031108, 2016. doi: 10.1063/1.4959256.

[75] D. Kraus, A. Ravasio, M. Gauthier, D. O. Gericke, J. Vorberger, S. Frydrych, J. Helfrich, L. B. Fletcher, G. Schaumann, B. Nagler, B. Barbrel, B. Bachmann, E. J. Gamboa, S. Göde, E. Granados, G. Gregori, H. J. Lee, P. Neumayer, W. Schumaker, T. Döppner, R. W. Falcone, S. H. Glenzer, and M. Roth. "Nanosecond formation of diamond and lonsdaleite by shock compression of graphite". *Nature Communications*, 7(1):10970, 2016. doi: 10.1038/ncomms10970.

[76] F. Girard. "Review of laser produced multi-keV X-ray sources from metallic foils, cylinders with liner, and low density aerogels". *Physics of Plasmas*, 23(4):040501, 2016. doi: 10.1063/1.4947306.

[77] C. E. Wehrenberg, D. McGonegle, C. Bolme, A. Higginbotham, A. Lazicki, H. J. Lee, B. Nagler, H.-S. Park, B. A. Remington, R. E. Rudd, M. Sliwa, M. Suggit, D. Swift, F. Tavella, L. Zepeda-Ruiz, and J. S. Wark. "In situ X-ray diffraction measurement of

shock-wave-driven twinning and lattice dynamics". *Nature*, 550(7677):496–499, 2017. doi: 10.1038/nature24061.

[78] R. Briggs, M. G. Gorman, A. L. Coleman, R. S. McWilliams, E. E. McBride, D. McGonegle, J. S. Wark, L. Peacock, S. Rothman, S. G. Macleod, C. A. Bolme, A. E. Gleason, G. W. Collins, J. H. Eggert, D. E. Fratanduono, R. F. Smith, E. Galtier, E. Granados, H. J. Lee, B. Nagler, I. Nam, Z. Xing, and M. I. McMahon. "Ultrafast X-Ray Diffraction Studies of the Phase Transitions and Equation of State of Scandium Shock Compressed to 82 GPa". *Physical Review Letters*, 118(2):025501, 2017. doi: 10.1103/PhysRevLett.118.025501.

[79] M. G. Gorman, A. L. Coleman, R. Briggs, R. S. McWilliams, D. McGonegle, C. A. Bolme, A. E. Gleason, E. Galtier, H. J. Lee, E. Granados, M. Śliwa, C. Sanloup, S. Rothman, D. E. Fratanduono, R. F. Smith, G. W. Collins, J. H. Eggert, J. S. Wark, and M. I. McMahon. "Femtosecond diffraction studies of solid and liquid phase changes in shock-compressed bismuth". *Scientific Reports*, 8(1):16927, 2018. doi: 10.1038/s41598-018-35260-3.

[80] D. N. Polsin, D. E. Fratanduono, J. R. Rygg, A. Lazicki, R. F. Smith, J. H. Eggert, M. C. Gregor, B. J. Henderson, X. Gong, J. A. Delettrez, R. G. Kraus, P. M. Celliers, F. Coppari, D. C. Swift, C. A. McCoy, C. T. Seagle, J.-P. Davis, S. J. Burns, G. W. Collins, and T. R. Boehly. "X-ray diffraction of ramp-compressed aluminum to 475 GPa". *Physics of Plasmas*, 25(8):082709, 2018. doi: 10.1063/1.5032095.

[81] S. J. Tracy, S. J. Turneaure, and T. S. Duffy. "In situ X-Ray Diffraction of Shock-Compressed Fused Silica". *Physical Review Letters*, 120(13):135702, 2018. doi: 10.1103/PhysRevLett.120.135702.

[82] S. J. Tracy, R. F. Smith, J. K. Wicks, D. E. Fratanduono, A. E. Gleason, C. A. Bolme, V. B. Prakapenka, S. Speziale, K. Appel, A. Fernandez-Pañella, H. J. Lee, A. MacKinnon, F. Tavella, J. H. Eggert, and T. S. Duffy. "Insitu observation of a phase transition in silicon carbide under shock compression using pulsed x-ray diffraction". *Physical Review B*, 99(21):214106, 2019. doi: 10.1103/PhysRevB.99.214106.

[83] R. Briggs, F. Coppari, M. G. Gorman, R. F. Smith, S. J. Tracy, A. L. Coleman, A. Fernandez-Pañella, M. Millot, J. H. Eggert, and D. E. Fratanduono. "Measurement of body-centered cubic gold and melting under shock compression". *Phys. Rev. Lett.*, 123:045701, 2019. doi: 10.1103/PhysRevLett.123.045701.

[84] R. Briggs, M. G. Gorman, S. Zhang, D. McGonegle, A. L. Coleman, F. Coppari, M. A. Morales-Silva, R. F. Smith, J. K. Wicks, C. A. Bolme, A. E. Gleason, E. Cunningham, H. J. Lee, B. Nagler, M. I. McMahon, J. H. Eggert, and D. E. Fratanduono. "Coordination changes in liquid tin under shock compression determined using in situ femtosecond x-ray diffraction". *Applied Physics Letters*, 115(26):264101, 2019. doi: 10.1063/1.5127291.

[85] M. G. Gorman, A. L. Coleman, R. Briggs, R. S. McWilliams, A. Hermann, D. McGonegle, C. A. Bolme, A. E. Gleason, E. Galtier, H. J. Lee, E. Granados, E. E. McBride, S. Rothman, D. E. Fratanduono, R. F. Smith, G. W. Collins, J. H. Eggert, J. S. Wark, and M. I. McMahon. "Recovery of metastable dense Bi synthesized by shock compression". *Applied Physics Letters*, 114(12):120601, 2019. doi: 10.1063/1.5085678.

[86] S. M. Sharma, S. J. Turneaure, J. M. Winey, Y. Li, P. Rigg, A. Schuman, N. Sinclair, Y. Toyoda, X. Wang, N. Weir, J. Zhang, and Y. M. Gupta. "Structural transformation and melting in gold shock compressed to 355 gpa". *Phys. Rev. Lett.*, 123:045702, 2019. doi: 10.1103/PhysRevLett.123.045702.

[87] Y. Inubushi, T. Yabuuchi, T. Togashi, K. Sueda, K. Miyanishi, Y. Tange, N. Ozaki, T. Matsuoka, R. Kodama, T. Osaka, S. Matsuyama, K. Yamauchi, H. Yumoto, T. Koyama, H. Ohashi, K. Tono, and M. Yabashi. "Development of an Experimental Platform for Combinative Use of an XFEL and a High-Power Nanosecond Laser". *Applied Sciences*, 10(7):2224, 2020. doi: 10.3390/app10072224.

[88] H. Hwang, E. Galtier, H. Cynn, I. Eom, S. H. Chun, Y. Bang, G. C. Hwang, J. Choi, T. Kim, M. Kong, S. Kwon, K. Kang, H. J. Lee, C. Park, J. I. Lee, Y. Lee, W. Yang, S.-H. Shim, T. Vogt, S. Kim, J. Park, S. Kim, D. Nam, J. H. Lee, H. Hyun, M. Kim, T.-Y. Koo, C.-C. Kao, T. Sekine, and Y. Lee. "Subnanosecond phase transition dynamics in laser-shocked iron". *Science Advances*, 6(23):eaaz5132, 2020. doi: 10.1126/sciadv.aaz5132.

[89] J. M. Foster, P. W. Avraam, E. K. R. Floyd, A. J. Comley, S. D. Rothman, D. R. McGonegle, P. Graham, L. J. Peacock, R. Penman, J. J. D. Luis, and C. P. Poulter. "X-ray diffraction data from shock-compressed copper: Some consequences of metallurgical texture". *Journal of Applied Physics*, 129(24):245904, 2021. doi: 10.1063/5.0053425.

[90] M. K. Wallace, J. M. Winey, and Y. M. Gupta. "Shock compression of silver to 300 GPa: Wave profile measurements and melting transition". *Physical Review B*, 104(1):014101, 2021. doi: 10.1103/PhysRevB.104.014101.

[91] W. J. M. Rankine. "Xv. on the thermodynamic theory of waves of finite longitudinal disturbance". *Philosophical Transactions of the Royal Society of London*, 160:277–288, 1870. doi: 10.1098/rstl.1870.0015.

[92] P. H. Hugoniot. "Memoire sur la propagation du mouvement dans les corps et plus spécialement dans les gaz parfaits, 1e partie". *Journal de l'École polytechnique*, 57:3–97, 1887.

[93] D. Errandonea, B. Schwager, R. Ditz, C. Gessmann, R. Boehler, and M. Ross. "Systematics of transition-metal melting". *Physical Review B*, 63(13):132104, 2001. doi: 10.1103/PhysRevB.63.132104.

[94] A. Dewaele, P. Loubeyre, and M. Mezouar. "Equations of state of six metals above 94 GPa". *Physical Review B*, 70(9):094112, 2004. doi: 10.1103/PhysRevB.70.094112.

[95] S. Anzellini, A. Dewaele, M. Mezouar, P. Loubeyre, and G. Morard. "Melting of Iron at Earth's Inner Core Boundary Based on Fast X-ray Diffraction". *Science*, 340(6131): 464–466, 2013. doi: 10.1126/science.1233514.

[96] D. McGonegle, P. G. Heighway, M. Sliwa, C. A. Bolme, A. J. Comley, L. E. Dresselhaus-Marais, A. Higginbotham, A. J. Poole, E. E. McBride, B. Nagler, I. Nam, M. H. Seaberg, B. A. Remington, R. E. Rudd, C. E. Wehrenberg, and J. S. Wark. "Investigating off-hugoniot states using multi-layer ring-up targets". *Scientific Reports*, 10:13172, 2020. doi: 10.1038/s41598-020-68544-8.

[97] B. Zel'dovich and Y. Raizer. *Physics of Shock Waves and High-Temperature Hydrodynamic Phenomena*, volume 475 of *10*. Dover, 3 edition, 2002. doi: 10.1017/S0022112002233376.

[98] D. C. Swift, R. G. Kraus, E. N. Loomis, D. G. Hicks, J. M. McNaney, and R. P. Johnson. "Shock formation and the ideal shape of ramp compression waves". *Physical Review E*, 78(6):066115, 2008. doi: 10.1103/PhysRevE.78.066115.

[99] A. Higginbotham, J. Hawreliak, E. M. Bringa, G. Kimminau, N. Park, E. Reed, B. A. Remington, and J. S. Wark. "Molecular dynamics simulations of ramp-compressed copper". *Physical Review B*, 85(2):024112, 2012. doi: 10.1103/PhysRevB.85.024112.

[100] M. X. Tang, J. C. E, L. Wang, and S. N. Luo. "Loading-path dependent deformation of nanocrystalline ta under single- and double-shock, and quasi-isentropic compression". *Journal of Applied Physics*, 121(11):115901, 2017. doi: 10.1063/1.4978359.

[101] J. R. Rygg, R. F. Smith, A. E. Lazicki, D. G. Braun, D. E. Fratanduono, R. G. Kraus, J. M. McNaney, D. C. Swift, C. E. Wehrenberg, F. Coppari, M. F. Ahmed, M. A. Barrios, K. J. M. Blobaum, G. W. Collins, A. L. Cook, P. Di Nicola, E. G. Dzenitis, S. Gonzales, B. F. Heidl, M. Hohenberger, A. House, N. Izumi, D. H. Kalantar, S. F. Khan, T. R. Kohut, C. Kumar, N. D. Masters, D. N. Polsin, S. P. Regan, C. A. Smith, R. M. Vignes, M. A. Wall, J. Ward, J. S. Wark, T. L. Zobrist, A. Arsenlis, and J. H. Eggert. "X-ray diffraction at the National Ignition Facility". *Review of Scientific Instruments*, 91(4):043902, 2020. doi: 10.1063/1.5129698.

[102] S. C. Grant, T. Ao, C. T. Seagle, A. J. Porwitzky, J. Davis, K. R. Cochrane, D. H. Dolan, J. Lin, T. Ditmire, and A. C. Bernstein. "Equation of State Measurements on Iron Near the Melting Curve at Planetary Core Conditions by Shock and Ramp Compressions". *Journal of Geophysical Research: Solid Earth*, 126(3), 2021. doi: 10.1029/2020JB020008.

[103] D. E. Fratanduono, M. Millot, D. G. Braun, S. J. Ali, A. Fernandez-Pañella, C. T. Seagle, J.-P. Davis, J. L. Brown, Y. Akahama, R. G. Kraus, M. C. Marshall, R. F. Smith, E. F. O'Bannon, J. M. McNaney, and J. H. Eggert. "Establishing gold and platinum standards to 1 terapascal using shockless compression". *Science*, 372(6546): 1063–1068, 2021. doi: 10.1126/science.abh0364.

[104] H.-S. Park, S. J. M. Ali, P. M. Celliers, F. Coppari, J. Eggert, A. Krygier, A. E. Lazicki, J. M. Mcnaney, M. Millot, Y. Ping, R. E. Rudd, B. A. Remington, H. Sio, R. F. Smith, M. D. Knudson, and E. E. McBride. "Techniques for studying materials under extreme states of high energy density compression". *Physics of Plasmas*, 28(6): 060901, 2021. doi: 10.1063/5.0046199.

[105] D. C. Swift, A. L. Kritcher, A. Lazicki, J. A. Hawreliak, T. Doeppner, H. D. Whitley, J. Nilsen, B. Bachmann, M. MacDonald, B. Maddox, N. Kostinski, G. W. Collins, S. Glenzer, S. D. Rothman, D. Kraus, and R. W. Falcone. "Shock Hugoniot of diamond from 3 to 80 TPa". *arXiv*, 2022.

[106] D. K. Bradley, J. H. Eggert, R. F. Smith, S. T. Prisbrey, D. G. Hicks, D. G. Braun, J. Biener, A. V. Hamza, R. E. Rudd, and G. W. Collins. "Diamond at 800 GPa". *Physical Review Letters*, 102(7):075503, 2009. doi: 10.1103/PhysRevLett.102.075503.

[107] C. J. Pickard and R. J. Needs. "Aluminium at terapascal pressures". *Nature Materials*, 9(8):624–627, 2010. doi: 10.1038/nmat2796.

[108] F. Coppari, R. F. Smith, J. H. Eggert, J. Wang, J. R. Rygg, A. Lazicki, J. A. Hawreliak, G. W. Collins, and T. S. Duffy. "Experimental evidence for a phase transition in magnesium oxide at exoplanet pressures". *Nature Geoscience*, 6(11):926–929, 2013. doi: 10.1038/ngeo1948.

[109] R. F. Smith, J. H. Eggert, R. Jeanloz, T. S. Duffy, D. G. Braun, J. R. Patterson, R. E. Rudd, J. Biener, A. E. Lazicki, A. V. Hamza, J. Wang, T. Braun, L. X. Benedict, P. M. Celliers, and G. W. Collins. "Ramp compression of diamond to five terapascals". *Nature*, 511(7509):330–333, 2014. doi: 10.1038/nature13526.

[110] D. E. Fratanduono, R. F. Smith, S. J. Ali, D. G. Braun, A. Fernandez-Pañella, S. Zhang, R. G. Kraus, F. Coppari, J. M. McNaney, M. C. Marshall, L. E. Kirch, D. C. Swift, M. Millot, J. K. Wicks, and J. H. Eggert. "Probing the Solid Phase of Noble Metal Copper at Terapascal Conditions". *Physical Review Letters*, 124(1): 015701, 2020. doi: 10.1103/PhysRevLett.124.015701.

[111] A. Lazicki, D. McGonegle, J. R. Rygg, D. G. Braun, D. C. Swift, M. G. Gorman, R. F. Smith, P. G. Heighway, A. Higginbotham, M. J. Suggit, D. E. Fratanduono, F. Coppari, C. E. Wehrenberg, R. G. Kraus, D. Erskine, J. V. Bernier, J. M. McNaney, R. E. Rudd, G. W. Collins, J. H. Eggert, and J. S. Wark. "Metastability of diamond ramp-compressed to 2 terapascals". *Nature*, 589(7843):532–535, 2021. doi: 10.1038/s41586-020-03140-4.

[112] M. S. Schneider, B. Kad, D. H. Kalantar, B. A. Remington, E. Kenik, H. Jarmakani, and M. A. Meyers. "Laser shock compression of copper and copper–aluminum alloys". *International Journal of Impact Engineering*, 32(1-4):473–507, 2005. doi: 10.1016/j.ijimpeng.2005.05.010.

[113] D. N. Polsin, A. Lazicki, X. Gong, S. J. Burns, F. Coppari, L. E. Hansen, B. J. Henderson, M. F. Huff, M. I. McMahon, M. Millot, R. Paul, R. F. Smith, J. H. Eggert, G. W. Collins, and J. R. Rygg. "Structural complexity in ramp-compressed sodium to 480 GPa". *Nature Communications*, 13(1):2534, 2022. doi: 10.1038/s41467-022-29813-4.

[114] S. Khan, K. Holldack, T. Kachel, R. Mitzner, and T. Quast. "Femtosecond Undulator Radiation from Sliced Electron Bunches". *Physical Review Letters*, 97(7):074801, 2006. doi: 10.1103/PhysRevLett.97.074801.

[115] P. Beaud, S. L. Johnson, A. Streun, R. Abela, D. Abramsohn, D. Grolimund, F. Krasniqi, T. Schmidt, V. Schlott, and G. Ingold. "Spatiotemporal Stability of a Femtosecond Hard–X-Ray Undulator Source Studied by Control of Coherent Optical Phonons". *Physical Review Letters*, 99(17):174801, 2007. doi: 10.1103/PhysRevLett.99.174801.

[116] R. W. Schoenlein. "Generation of Femtosecond Pulses of Synchrotron Radiation". *Science*, 287(5461):2237–2240, 2000. doi: 10.1126/science.287.5461.2237.

[117] S. M. Sharma, S. J. Turneaure, J. M. Winey, and Y. M. Gupta. "Transformation of shock-compressed copper to the body-centered-cubic structure at 180 GPa". *Physical Review B*, 102(2):020103, 2020. doi: 10.1103/PhysRevB.102.020103.

[118] B. W. J. McNeil and N. R. Thompson. "X-ray free-electron lasers". *Nature Photonics*, 4(12):814–821, 2010. doi: 10.1038/nphoton.2010.239.

[119] G. Margaritondo and P. Rebernik Ribic. "A simplified description of X-ray free-electron lasers". *Journal of Synchrotron Radiation*, 18(2):101–108, 2011. doi: 10.1107/S090904951004896X.

[120] E. A. Schneidmiller and M. V. Yurkov. "Baseline parameters of the European XFEL". In *Proceedings of the 38th International Free-Electron Laser Conference, FEL 2017*, pages 109–112. JACoW Publishing, 2017. doi: 10.18429/JACoW-FEL2017-MOP033.

[121] N. Huang, H. Deng, B. Liu, D. Wang, and Z. Zhao. "Features and futures of X-ray free-electron lasers". *The Innovation*, 2(2):100097, 2021. doi: 10.1016/j.xinn.2021.100097.

[122] Y. Ihm, D. H. Cho, D. Sung, D. Nam, C. Jung, T. Sato, S. Kim, J. Park, S. Kim, M. Gallagher-Jones, Y. Kim, R. Xu, S. Owada, J. H. Shim, K. Tono, M. Yabashi, T. Ishikawa, J. Miao, D. Y. Noh, and C. Song. "Direct observation of picosecond melting and disintegration of metallic nanoparticles". *Nature Communications*, 10(1): 2411, 2019. doi: 10.1038/s41467-019-10328-4.

[123] J. Schiotz. "A Maximum in the Strength of Nanocrystalline Copper". *Science*, 301 (5638):1357–1359, 2003. doi: 10.1126/science.1086636.

[124] S. Mehta, G. D. Price, and D. Alfè. "Ab initio thermodynamics and phase diagram of solid magnesium: A comparison of the LDA and GGA". *The Journal of Chemical Physics*, 125(19):194507, 2006. doi: 10.1063/1.2374892.

[125] E. M. Bringa, K. Rosolankova, R. E. Rudd, B. A. Remington, J. S. Wark, M. Duchaineau, D. H. Kalantar, J. Hawreliak, and J. Belak. "Shock deformation of face-centred-cubic metals on subnanosecond timescales". *Nature Materials*, 5(10): 805–809, 2006. doi: 10.1038/nmat1735.

[126] G. Kimminau, B. Nagler, A. Higginbotham, W. J. Murphy, N. Park, J. Hawreliak, K. Kadau, T. C. Germann, E. M. Bringa, D. H. Kalantar, H. E. Lorenzana, B. A. Remington, and J. S. Wark. "Simulating picosecond x-ray diffraction from shocked crystals using post-processing molecular dynamics calculations". *Journal of Physics: Condensed Matter*, 20(50):505203, 2008. doi: 10.1088/0953-8984/20/50/505203.

[127] H. Jarmakani, E. Bringa, P. Erhart, B. Remington, Y. Wang, N. Vo, and M. Meyers. "Molecular dynamics simulations of shock compression of nickel: From monocrystals to nanocrystals". *Acta Materialia*, 56(19):5584–5604, 2008. doi: 10.1016/j.actamat.2008.07.052.

[128] M. J. Echeverria, S. Galitskiy, A. Mishra, R. Dingreville, and A. M. Dongare. "Understanding the plasticity contributions during laser-shock loading and spall failure of Cu microstructures at the atomic scales". *Computational Materials Science*, 198:110668, 2021. doi: 10.1016/j.commatsci.2021.110668.

[129] I. Bryukhanov and V. Emelyanov. "Shear stress relaxation through the motion of edge dislocations in Cu and Cu–Ni solid solution: A molecular dynamics and discrete dislocation study". *Computational Materials Science*, 201:110885, 2022. doi: 10.1016/j.commatsci.2021.110885.

[130] I. Bryukhanov. "Atomistic simulation of the shock wave in copper single crystals with pre-existing dislocation network". *International Journal of Plasticity*, page 103171, 2022. doi: 10.1016/j.ijplas.2021.103171.

[131] R. Wang, C. Lu, K. A. Tieu, and A. A. Gazder. "Slip system activity and lattice rotation in polycrystalline copper during uniaxial tension". *Journal of Materials Research and Technology*, 18:508–519, 2022. doi: 10.1016/j.jmrt.2022.02.110.

[132] L. M. Barker and R. E. Hollenbach. "Laser interferometer for measuring high velocities of any reflecting surface". *Journal of Applied Physics*, 43(11):4669–4675, 1972. doi: 10.1063/1.1660986.

[133] P. M. Celliers, D. K. Bradley, G. W. Collins, D. G. Hicks, T. R. Boehly, and W. J. Armstrong. "Line-imaging velocimeter for shock diagnostics at the OMEGA laser facility". *Review of Scientific Instruments*, 75(11):4916–4929, 2004. doi: 10.1063/1.1807008.

[134] D. Dolan. "Accuracy and precision in photonic doppler velocimetry". *The Review of scientific instruments*, 81:053905, 2010. doi: 10.1063/1.3429257.

[135] W. J. Murphy, A. Higginbotham, J. S. Wark, and N. Park. "Temperature measurements of shocked crystals by use of nanosecond x-ray diffraction". *AIP Conference Proceedings*, 955(1):325–328, 2007. doi: 10.1063/1.2833045.

[136] W. J. Murphy, A. Higginbotham, J. S. Wark, and N. Park. "Molecular dynamics simulations of the debye-waller effect in shocked copper". *Physical Review B*, 78: 014109, 2008. doi: 10.1103/PhysRevB.78.014109.

[137] Y. Ping, F. Coppari, D. G. Hicks, B. Yaakobi, D. E. Fratanduono, S. Hamel, J. H. Eggert, J. R. Rygg, R. F. Smith, D. C. Swift, D. G. Braun, T. R. Boehly, and G. W. Collins. "Solid Iron Compressed Up to 560 GPa". *Physical Review Letters*, 111(6): 065501, 2013. doi: 10.1103/PhysRevLett.111.065501.

[138] P. Scardi, L. Rebuffi, M. Abdellatief, A. Flor, and A. Leonardi. "Debye–Waller coefficient of heavily deformed nanocrystalline iron". *Journal of Applied Crystallography*, 50(2):508–518, 2017. doi: 10.1107/S160057671700022X.

[139] S. M. Sharma and Y. M. Gupta. "Inherent issues regarding the use of in situ x-ray diffraction measurements to determine temperature in shock-compressed metals". *Physical Review B*, 104(6):064113, 2021. doi: 10.1103/PhysRevB.104.064113.

[140] N. Van Hung, T. T. Hue, N. C. Toan, and D. Q. Vuong. "Advanced classical anharmonic correlated Einstein model high-order expanded Debye-Waller factors and EXAFS". *Radiation Physics and Chemistry*, 191:109844, 2022. doi: 10.1016/j.radphyschem.2021.109844.

[141] S. J. Turneaure and P. Das. "Vibrational response and temperature of shock-compressed Pt: In situ extended x-ray absorption fine structure measurements to 325 GPa". *Physical Review B*, 105(17):174103, 2022. doi: 10.1103/PhysRevB.105.174103.

[142] P. Vieillefosse and J. P. Hansen. "Statistical mechanics of dense ionized matter. V. Hydrodynamic limit and transport coefficients of the classical one-component plasma". *Physical Review A*, 12(3):1106–1116, 1975. doi: 10.1103/PhysRevA.12.1106.

[143] T. Scopigno, G. Ruocco, and F. Sette. "Microscopic dynamics in liquid metals: The experimental point of view". *Reviews of Modern Physics*, 77(3):881–933, 2005. doi: 10.1103/RevModPhys.77.881.

[144] E. E. McBride, T. G. White, A. Descamps, L. B. Fletcher, K. Appel, F. P. Condamine, C. B. Curry, F. Dallari, S. Funk, E. Galtier, M. Gauthier, S. Goede, J. B. Kim, H. J. Lee, B. K. Ofori-Okai, M. Oliver, A. Rigby, C. Schoenwaelder, P. Sun, T. Tschentscher, B. B. L. Witte, U. Zastrau, G. Gregori, B. Nagler, J. Hastings, S. H. Glenzer, and G. Monaco. "Setup for meV-resolution inelastic X-ray scattering measurements and X-ray diffraction at the Matter in Extreme Conditions endstation at the Linac Coherent Light Source". *Review of Scientific Instruments*, 89(10):10F104, 2018. doi: 10.1063/1.5039329.

[145] A. Descamps, B. K. Ofori-Okai, K. Appel, V. Cerantola, A. Comley, J. H. Eggert, L. B. Fletcher, D. O. Gericke, S. Göde, O. Humphries, O. Karnbach, A. Lazicki, R. Loetzsch, D. McGonegle, C. A. J. Palmer, C. Plueckthun, T. R. Preston, R. Redmer, D. G. Senesky, C. Strohm, I. Uschmann, T. G. White, L. Wollenweber, G. Monaco, J. S. Wark, J. B. Hastings, U. Zastrau, G. Gregori, S. H. Glenzer, and E. E. McBride. "An approach for the measurement of the bulk temperature of single crystal diamond using an X-ray free electron laser". *Scientific Reports*, 10(1):14564, 2020. doi: 10.1038/s41598-020-71350-x.

[146] L. Wollenweber, T. R. Preston, A. Descamps, V. Cerantola, A. Comley, J. H. Eggert, L. B. Fletcher, G. Geloni, D. O. Gericke, S. H. Glenzer, S. Göde, J. Hastings, O. S. Humphries, A. Jenei, O. Karnbach, Z. Konopkova, R. Loetzsch, B. Marx-Glowna, E. E. McBride, D. McGonegle, G. Monaco, B. K. Ofori-Okai, C. A. J. Palmer, C. Plückthun, R. Redmer, C. Strohm, I. Thorpe, T. Tschentscher, I. Uschmann, J. S. Wark, T. G. White, K. Appel, G. Gregori, and U. Zastrau. "High-resolution inelastic x-ray scattering at the high energy density scientific instrument at the Free-Electron Laser". *Review of Scientific Instruments*, 92(1):013101, 2021. doi: 10.1063/5.0022886.

[147] J. Feldhaus, E. Saldin, J. Schneider, E. Schneidmiller, and M. Yurkov. "Possible application of X-ray optical elements for reducing the spectral bandwidth of an X-ray SASE FEL". *Optics Communications*, 140(4-6):341–352, 1997. doi: 10.1016/S0030-4018(97)00163-6.

[148] E. Saldin, E. Schneidmiller, Y. Shvyd'ko, and M. Yurkov. "X-ray FEL with a meV bandwidth". *Nuclear Instruments and Methods in Physics Research Section A: Accelerators, Spectrometers, Detectors and Associated Equipment*, 475(1-3):357–362, 2001. doi: 10.1016/S0168-9002(01)01539-X.

[149] P. Mason, M. Divoký, K. Ertel, J. Pilař, T. Butcher, M. Hanuš, S. Banerjee, J. Phillips, J. Smith, M. De Vido, A. Lucianetti, C. Hernandez-Gomez, C. Edwards, T. Mocek, and J. Collier. "Kilowatt average power 100 J-level diode pumped solid state laser". *Optica*, 4(4):438, 2017. doi: 10.1364/OPTICA.4.000438.

[150] B. Sadigh, L. Zepeda-Ruiz, and J. L. Belof. "Metastable–solid phase diagrams derived from polymorphic solidification kinetics". *Proceedings of the National Academy of Sciences*, 118(9), 2021. doi: 10.1073/pnas.2017809118.

[151] O. Karnbach, P. G. Heighway, D. McGonegle, R. E. Rudd, G. Gregori, and J. S. Wark. "Molecular dynamics simulations of inelastic x-ray scattering from shocked copper". *Journal of Applied Physics*, 130(12):125901, 2021. doi: 10.1063/5.0057044.

[152] T. Preston, S. Göde, J.-P. Schwinkendorf, K. Appel, E. Brambrink, V. Cerantola, H. Höppner, M. Makita, A. Pelka, C. Prescher, K. Sukharnikov, A. Schmidt, I. Thorpe, T. Toncian, A. Amouretti, D. Chekrygina, R. Falcone, K. Falk, L. Fletcher, E. Galtier, M. Harmand, N. Hartley, S. Hau-Riege, P. Heimann, L. Huang, O. Humphries, O. Karnbach, D. Kraus, H. Lee, B. Nagler, S. Ren, A. Schuster, M. Smid, K. Voigt,

M. Zhang, and U. Zastrau. "Design and performance characterisation of the HAPG von Hámos Spectrometer at the High Energy Density Instrument of the European XFEL". *Journal of Instrumentation*, 15(11):P11033–P11033, 2020. doi: 10.1088/1748-0221/15/11/P11033.

[153] W. H. Zachariasen. *Theory of X-Ray Diffraction in Crystals*. Dover Publications, Inc., New York, NY, 1945.

[154] B. E. Warren. *X-Ray Diffraction*. Dover Publications, Inc., New York, NY, 1990.

[155] G. P. Srivastava. *The physics of phonons*. Taylor and Francis Group, New York, NY, 1990.

[156] M. A. Meyers. *Dynamic Behavior of Materials*. Wiley, New York, NY, 1994. doi: 10.1007/s11340-012-9598-0.

[157] D. C. Rapaport. *The Art of Molecular Dynamics Simulation*. Cambridge University Press, Cambridge, 2004.

[158] J. Als-Nielsen and D. McMorrow. *Elements of Modern X-ray Physics*. Wiley, 2 edition, 2011.

[159] G. Geloni, V. Kocharyan, and E. Saldin. "Cost-effective way to enhance the capabilities of the LCLS baseline". *arXiv*, 2010.

[160] J. Amann, W. Berg, V. Blank, F.-J. Decker, Y. Ding, P. Emma, Y. Feng, J. Frisch, D. Fritz, J. Hastings, Z. Huang, J. Krzywinski, R. Lindberg, H. Loos, A. Lutman, H.-D. Nuhn, D. Ratner, J. Rzepiela, D. Shu, Y. Shvyd'ko, S. Spampinati, S. Stoupin, S. Terentyev, E. Trakhtenberg, D. Walz, J. Welch, J. Wu, A. Zholents, and D. Zhu. "Demonstration of self-seeding in a hard-X-ray free-electron laser". *Nature Photonics*, 6(10):693–698, 2012. doi: 10.1038/nphoton.2012.180.

[161] C. E. Anderson. "An overview of the theory of hydrocodes". *International Journal of Impact Engineering*, 5(1-4):33–59, 1987. doi: 10.1016/0734-743X(87)90029-7.

[162] E. S. Hertel, Jr. "A survey of numerical methods for shock physics applications". *osti.gov*, 1997.

[163] S. Plimpton. "Fast parallel algorithms for short-range molecular dynamics". *Journal of Computational Physics*, 117(1):1 – 19, 1995. doi: https://doi.org/10.1006/jcph.1995.1039.

[164] B. R. Maddox, H. S. Park, B. A. Remington, and M. McKernan. "Calibration and characterization of single photon counting cameras for short-pulse laser experiments". *Review of Scientific Instruments*, 79(10):10E924, 2008. doi: 10.1063/1.2966374.

[165] S. Fourmaux, S. Corde, K. Ta Phuoc, P. M. Leguay, S. Payeur, P. Lassonde, S. Gnedyuk, G. Lebrun, C. Fourment, V. Malka, S. Sebban, A. Rousse, and J. C. Kieffer. "Demonstration of the synchrotron-type spectrum of laser-produced Betatron radiation". *New Journal of Physics*, 13(3):033017, 2011. doi: 10.1088/1367-2630/13/3/033017.

[166] A. Higginbotham, M. J. Suggit, E. M. Bringa, P. Erhart, J. A. Hawreliak, G. Mogni, N. Park, B. A. Remington, and J. S. Wark. "Molecular dynamics simulations of shock-induced deformation twinning of a body-centered-cubic metal". *Physical Review B*, 88:104105, 2013. doi: 10.1103/PhysRevB.88.104105.

[167] A. Higginbotham and D. McGonegle. "Prediction of debye-scherrer diffraction patterns in arbitrarily strained samples". *Journal of Applied Physics*, 115(17):174906, 2014. doi: 10.1063/1.4874656.

[168] D. McGonegle, D. Milathianaki, B. A. Remington, J. S. Wark, and A. Higginbotham. "Simulations of in situ x-ray diffraction from uniaxially compressed highly textured polycrystalline targets". *Journal of Applied Physics*, 118(6):065902, 2015. doi: 10.1063/1.4927275.

[169] D. Francom, D. J. Walters, J. L. Barber, D. J. Luscher, E. Lawrence, A. Biswas, C. M. Biwer, D. Banesh, J. Lazarz, S. C. Vogel, K. Ramos, C. Bolme, R. L. Sandberg, and J. Ahrens. "Simulation and Emulation of X-Ray Diffraction from Dynamic Compression Experiments". *Journal of Dynamic Behavior of Materials*, 2020. doi: 10.1007/s40870-020-00254-8.

[170] J. S. Wark. "Picosecond X-Ray Diffraction from Laser-Shocked Copper and Iron". *Journal of Applied Physics*, 845:286–291, 2006. doi: 10.1063/1.2263319.

[171] K. Rosolankova, J. S. Wark, E. M. Bringa, and J. Hawreliak. "Measuring stacking fault densities in shock-compressed FCC crystals using in situ x-ray diffraction". *Journal of Physics: Condensed Matter*, 18(29):6749–6757, 2006. doi: 10.1088/0953-8984/18/29/014.

[172] R. Ravelo, T. C. Germann, O. Guerrero, Q. An, and B. L. Holian. "Shock-induced plasticity in tantalum single crystals: Interatomic potentials and large-scale molecular-dynamics simulations". *Phys. Rev. B*, 88:134101, 2013. doi: 10.1103/PhysRevB.88.134101.

[173] Q.-l. Xiong, T. Kitamura, and Z. Li. "Transient phase transitions in single-crystal coppers under ultrafast lasers induced shock compression: A molecular dynamics study". *Journal of Applied Physics*, 125(19):194302, 2019. doi: 10.1063/1.5088371.

[174] N. Amadou, T. De Resseguier, A. Dragon, and E. Brambrink. "Effects of orientation, lattice defects and temperature on plasticity and phase transition in ramp-compressed single crystal iron". *Computational Materials Science*, 172:109318, 2020. doi: 10.1016/j.commatsci.2019.109318.

[175] L. Zhang, C. Lu, G. Michal, G. Deng, and K. Tieu. "The formation and destruction of stacking fault tetrahedron in fcc metals: A molecular dynamics study". *Scripta Materialia*, 136:78–82, 2017. doi: 10.1016/j.scriptamat.2017.04.019.

[176] S. M. Sharma, S. Turneaure, J. Winey, P. Rigg, N. Sinclair, X. Wang, Y. Toyoda, and Y. Gupta. "Real-Time Observation of Stacking Faults in Gold Shock Compressed to 150 GPa". *Physical Review X*, 10(1):011010, 2020. doi: 10.1103/PhysRevX.10.011010.

[177] A. Stukowski and K. Albe. "Extracting dislocations and non-dislocation crystal defects from atomistic simulation data". *Modelling and Simulation in Materials Science and Engineering*, 18(8):085001, 2010. doi: 10.1088/0965-0393/18/8/085001.

[178] Y. Mishin, M. J. Mehl, D. A. Papaconstantopoulos, A. F. Voter, and J. D. Kress. "Structural stability and lattice defects in copper: Ab initio , tight-binding, and embedded-atom calculations". *Physical Review B*, 63(22):224106, 2001. doi: 10.1103/PhysRevB.63.224106.

[179] A. Stukowski. "Visualization and analysis of atomistic simulation data with OVITO-the Open Visualization Tool". *Modelling and Simulation in Materials Science and Engineering*, 18(1), 2010. doi: {10.1088/0965-0393/18/1/015012}.

[180] J. D. Honeycutt and H. C. Andersen. "Molecular dynamics study of melting and freezing of small Lennard-Jones clusters". *The Journal of Physical Chemistry*, 91(19): 4950–4963, 1987. doi: 10.1021/j100303a014.

[181] D. Faken and H. Jónsson. "Systematic analysis of local atomic structure combined with 3D computer graphics". *Computational Materials Science*, 2(2):279–286, 1994. doi: 10.1016/0927-0256(94)90109-0.

[182] H. Tsuzuki, P. S. Branicio, and J. P. Rino. "Structural characterization of deformed crystals by analysis of common atomic neighborhood". *Computer Physics Communications*, 177(6):518–523, 2007. doi: 10.1016/j.cpc.2007.05.018.

[183] E. Schmid and W. Boas. *Kristallplastizität*, volume 17. Springer, 1 edition, 1935. doi: 10.1007/978-3-662-34532-0.

[184] E. M. Bringa, J. U. Cazamias, P. Erhart, J. Stölken, N. Tanushev, B. D. Wirth, R. E. Rudd, and M. J. Caturla. "Atomistic shock hugoniot simulation of single-crystal copper". *Journal of Applied Physics*, 96(7):3793–3799, 2004. doi: 10.1063/1.1789266.

[185] A. Neogi and N. Mitra. "A metastable phase of shocked bulk single crystal copper: an atomistic simulation study". *Scientific Reports*, 7(1):7337, 2017. doi: 10.1038/s41598-017-07809-1.

[186] L. Velterop, R. Delhez, T. H. de Keijser, E. J. Mittemeijer, and D. Reefman. "X-ray diffraction analysis of stacking and twin faults in f.c.c. metals: a revision and allowance for texture and non-uniform fault probabilities". *Journal of Applied Crystallography*, 33(2):296–306, 2000. doi: 10.1107/S0021889800000133.

[187] G. Kimminau, B. Nagler, A. Higginbotham, W. Murphy, J. Wark, N. Park, J. Hawreliak, D. Kalantar, H. Lorenzana, and B. Remington. "Simulating picosecond X-ray diffraction from crystals using FFT methods on MD output". In *AIP Conference Proceedings*, volume 955, pages 1251–1254, 2007. doi: 10.1063/1.2832948.

[188] G. Kimminau, P. Erhart, E. M. Bringa, B. Remington, and J. S. Wark. "Phonon instabilities in uniaxially compressed fcc metals as seen in molecular dynamics simulations". *Physical Review B*, 81(9):092102, 2010. doi: 10.1103/PhysRevB.81.092102.

[189] Y. Chalopin and S. Volz. "A microscopic formulation of the phonon transmission at the nanoscale". *Applied Physics Letters*, 103(5):051602, 2013. doi: 10.1063/1.4816738.

[190] Y. Sun, Y. Zhou, M. Hu, G. Jeffrey Snyder, B. Xu, and W. Liu. "Probing the phonon mean free paths in dislocation core by molecular dynamics simulation". *Journal of Applied Physics*, 129(5):055103, 2021. doi: 10.1063/5.0038265.

[191] F. Harris. "On the use of windows for harmonic analysis with the discrete Fourier transform". *Proceedings of the IEEE*, 66(1):51–83, 1978. doi: 10.1109/PROC.1978.10837.

[192] M. Dupraz, G. Beutier, D. Rodney, D. Mordehai, and M. Verdier. "Signature of dislocations and stacking faults of face-centred cubic nanocrystals in coherent X-ray diffraction patterns: a numerical study". *Journal of Applied Crystallography*, 48(3):621–644, 2015. doi: 10.1107/S1600576715005324.

[193] C. Giannini, V. Holy, L. De Caro, L. Mino, and C. Lamberti. "Watching nanomaterials with X-Ray eyes: probing different length scales by combining scattering with spectroscopy". *Progress in Materials Science*, 112:100667, 2020. doi: 10.1016/j.pmatsci.2020.100667.

[194] J. D. Jackson. *Classical Electrodynamics*. Wiley, New York, 3 edition, 1999.

[195] C. Masciovecchio, U. Bergmann, M. Krisch, G. Ruocco, F. Sette, and R. Verbeni. "A perfect crystal X-ray analyser with meV energy resolution". *Nuclear Instruments and Methods in Physics Research Section B: Beam Interactions with Materials and Atoms*, 111(1-2):181–186, 1996. doi: 10.1016/0168-583X(95)01288-5.

[196] C. Masciovecchio, U. Bergmann, M. Krisch, G. Ruocco, F. Sette, and R. Verbeni. "A perfect crystal X-ray analyser with 1.5 meV energy resolution". *Nuclear Instruments and Methods in Physics Research Section B: Beam Interactions with Materials and Atoms*, 117(3):339–340, 1996. doi: 10.1016/0168-583X(96)00334-5.

[197] R. Verbeni, M. Kocsis, S. Huotari, M. Krisch, G. Monaco, F. Sette, and G. Vanko. "Advances in crystal analyzers for inelastic X-ray scattering". *Journal of Physics and Chemistry of Solids*, 66(12):2299–2305, 2005. doi: 10.1016/j.jpcs.2005.09.079.

[198] S. Huotari, F. Albergamo, G. Vankó, R. Verbeni, and G. Monaco. "Resonant inelastic hard x-ray scattering with diced analyzer crystals and position-sensitive detectors". *Review of Scientific Instruments*, 77(5):053102, 2006. doi: 10.1063/1.2198805.

[199] L. Boldon, F. Laliberte, and L. Liu. "Review of the fundamental theories behind small angle X-ray scattering, molecular dynamics simulations, and relevant integrated application". *Nano Reviews*, 6(1):25661, 2015. doi: 10.3402/nano.v6.25661.

[200] T. Li, A. J. Senesi, and B. Lee. "Small Angle X-ray Scattering for Nanoparticle Research". *Chemical Reviews*, 116(18):11128–11180, 2016. doi: 10.1021/acs.chemrev.5b00690.

[201] J. Li, A. Jiao, S. Chen, Z. Wu, E. Xu, and Z. Jin. "Application of the small-angle X-ray scattering technique for structural analysis studies: A review". *Journal of Molecular Structure*, 1165:391–400, 2018. doi: 10.1016/j.molstruc.2017.12.031.

[202] P. J. Brown, A. G. Fox, E. N. Maslen, M. A. O'Keefe, and B. T. M. Willis. "Intensity of diffracted intensities". In *International Tables for Crystallography*, pages 554–595. International Union of Crystallography, Chester, England, 2006. doi: 10.1107/97809553602060000600.

[203] R. Resel and P. Hadley. "Atomic form factors". `lampx.tugraz.at/~hadley/ss1/crystaldiffraction/atomicformfactors/formfactors.php`, 2022. [Online; accessed 21-April-2022].

[204] S. Huotari, G. Vankó, F. Albergamo, C. Ponchut, H. Graafsma, C. Henriquet, R. Verbeni, and G. Monaco. "Improving the performance of high-resolution X-ray spectrometers with position-sensitive pixel detectors". *Journal of Synchrotron Radiation*, 12(4):467–472, 2005. doi: 10.1107/S0909049505010630.

[205] G. Blaj, P. Caragiulo, G. Carini, S. Carron, A. Dragone, D. Freytag, G. Haller, P. Hart, J. Hasi, R. Herbst, S. Herrmann, C. Kenney, B. Markovic, K. Nishimura, S. Osier, J. Pines, B. Reese, J. Segal, A. Tomada, and M. Weaver. "X-ray detectors at the Linac Coherent Light Source". *Journal of Synchrotron Radiation*, 22(3):577–583, 2015. doi: 10.1107/S1600577515005317.

[206] A. Mozzanica, A. Bergamaschi, M. Brueckner, S. Cartier, R. Dinapoli, D. Greiffenberg, J. Jungmann-Smith, D. Maliakal, D. Mezza, M. Ramilli, C. Ruder, L. Schaedler, B. Schmitt, X. Shi, and G. Tinti. "Characterization results of the JUNGFRAU full scale readout ASIC". *Journal of Instrumentation*, 11(02):C02047–C02047, 2016. doi: 10.1088/1748-0221/11/02/C02047.

[207] Shung-Wu Lee and R. Mittra. "Fourier transform of a polygonal shape function and its application in electromagnetics". *IEEE Transactions on Antennas and Propagation*, 31(1):99–103, 1983. doi: 10.1109/TAP.1983.1142981.

[208] F.-L. Chu and C.-F. Huang. "On the calculation of the Fourier transform of a polygonal shape function". *Journal of Physics A: Mathematical and General*, 22(14):L671–L672, 1989. doi: 10.1088/0305-4470/22/14/003.

[209] C. Prescher and V. B. Prakapenka. "DIOPTAS : a program for reduction of two-dimensional X-ray diffraction data and data exploration". *High Pressure Research*, 35 (3):223–230, 2015. doi: 10.1080/08957959.2015.1059835.

[210] M. F. Kasim, T. P. Galligan, J. Topp-Mugglestone, G. Gregori, and S. M. Vinko. "Inverse problem instabilities in large-scale modeling of matter in extreme conditions". *Physics of Plasmas*, 26(11):112706, 2019. doi: 10.1063/1.5125979.

[211] N. Hansen. "The CMA Evolution Strategy: A Tutorial". *arXiv*, 2016.

[212] C. Andrieu, N. de Freitas, A. Doucet, and M. I. Jordan. "An Introduction to MCMC for Machine Learning". *Machine Learning*, 50(1):5–43, 2003. doi: 10.1023/A:1020281327116.

[213] T. C. Germann, B. L. Holian, P. S. Lomdahl, D. Tanguy, M. Mareschal, and R. Ravelo. "Dislocation structure behind a shock front in fcc perfect crystals: Atomistic simulation results". *Metallurgical and Materials Transactions A*, 35(9):2609–2615, 2004. doi: 10.1007/s11661-004-0206-5.

[214] A. Descamps, B. K. Ofori-Okai, J. K. Baldwin, Z. Chen, L. B. Fletcher, S. H. Glenzer, N. J. Hartley, J. B. Hasting, D. Khaghani, M. Mo, B. Nagler, V. Recoules, R. Redmer, M. Schörner, P. Sun, Y. Q. Wang, T. G. White, and E. E. McBride. "Towards performing high-resolution inelastic X-ray scattering measurements at hard X-ray free-electron lasers coupled with energetic laser drivers". *Journal of Synchrotron Radiation*, 29(4), 2022. doi: 10.1107/S1600577522004453.